U.PORTO

FEUP FACULDADE DE ENGENHARIA
UNIVERSIDADE DO PORTO

Vibration of nanobeams under electrostatic actuation

Marco Alexandre da Costa Alves

Supervisor:
Prof. Dr. Pedro Leal Ribeiro

A Thesis submitted for the degree of

Master of Science in Mechanical Engineering

to the Faculty of Engineering, University of Porto

Porto, July 2016

Título: Vibrações de nanovigas sobre actuação electroestática

Resumo

Dispositivos MEMS e NEMS baseados em micro ou nano vigas tem diversas aplicações tais como sensores, ecrãs, sistemas portáteis de geração de energia, administração localizada de drogas, e em todas as aplicações referidas, é essencial conhecer o comportamento dinâmico destes sistemas. O regime dinâmico destes dispositivos é inerentemente não linear devido às grandes amplitudes de vibração verificadas, quando comparadas com a sua espessura, e devido à não linearidade das forças de atuação electrostática. A análise e o conhecimento dos modos de vibração e das frequências naturais destes sistemas é essencial para o sucesso da sua implementação nas aplicações anteriormente referidas.

Nesta dissertação, os modos não lineares e as frequências de vibração de nano vigas atuadas sob forças electroestáticas são estudados. A formulação matemática é baseada no método *p* dos elementos finitos, e o método de Galerkin é usado para reduzir e discretizar as equações de movimento que são equações diferenciais não lineares de derivadas parciais em equações diferenciais não lineares ordinárias. O modelo é baseado na teoria de vigas de Timoshenko e na analogia para vigas da teoria de placas de von Kármán, que toma em consideração os efeitos da não linearidade geométrica. A teoria não local da elasticidade de Erigen foi utilizada para ter em conta os fenómenos de pequena escala, que alteram a inércia, a rigidez não linear do sistema e a atração electrostática. O método do balanceamento dos harmónicos (MBH) é utilizado para obter as equações não lineares algébricas que são resolvidas por um método de continuação. Vários harmónicos foram considerados para a solução periódica do MBH.

Os vários termos do modelo, relacionados com os efeitos considerados, são validados numericamente comparando os resultados obtidos com valores publicados na literatura. A deformada estática de vigas sob atração electroestática é determinada recorrendo ao método de Newton, e a influência de parâmetros geométricos e de efeitos não locais na deformada estática são analisados. É estudado também a influência da força electroestática, de efeitos de fronteira (franjas), efeitos não locais e da não linearidade geométrica na dinâmica deste tipo de vigas. As várias combinações destes efeitos levam a comportamentos dinâmicos extremamente diferentes. Fenómenos não lineares tais como ressonâncias internas e pontos de bifurcação são também analisados.

É feita uma introdução ao algoritmo de Dinâmica Molecular, que foi utilizado para calcular as frequências naturais naturais de um nanotubo de carbono. Os valores de frequência foram comparados com os calculados pelo modelo contínuo desenvolvido, na tentativa de definir um valor correto do parâmetro não local para este tipo de nanotubos.

Palavras-Chave: Nano vigas; Actuação electroestática; Modos não lineares de vibração; Frequências não lineares; Efeitos não locais; Ressonâncias internas; Dinâmica Molecular

Title: Vibration of nanobeams under electrostatic actuation

Abstract

Micro and nanobeam based devices (MEMS and NEMS) are employed in sensors, displays, portable power generation, localized drug delivery, and in all applications it is essential to understand their dynamic behaviour. The dynamics of these devices are inherently non-linear, due to the large displacements in comparison to the thickness and also to the non-linearity of the electrostatic force that is used to actuate them. The knowledge of the modes of vibration and the natural frequencies of nanobeams are essential to describe the dynamics of these systems, and to successfully implement them in the aforementioned applications.

In this dissertation, the non-linear modes of vibration of electrostatically actuated nanobeams are investigated. A *p*-version finite element derived by Galerkin's method is used to reduce the partial differential equations of motion into a finite dimensional system of non-linear ordinary differential equations in the time domain. The Timoshenko beam theory is applied, as well as the beam analogue of the von Kármán's plate theory in order to take into account the geometrical non-linearity. The formulation considers nonlocal effects which affects the inertia of the system as well as the non-linear stiffness terms and the electrostatic force. The harmonic balance method (HBM) is used to transform the ordinary differential equations into algebraic equations of motion in the frequency domain, which are then solved by an arc-length continuation method. Several harmonics are used in the periodic solution considered in the HBM.

The different terms related to the effects considered in the proposed model are validated with different numerical and experimental results published in the literature. The static deflection of electrostatically actuated nanobeams is determined using the Newton method. The influence of geometric properties and nonlocal effects in the static deformation is investigated. The influence in the dynamic response of the electrostatic force, fringing fields and nonlocal effects, combined with the geometrical non-linearity is investigated. One found that different combination of these effects lead to different outcomes in the system dynamics changing the natural frequencies, mode shapes, and leading to hardening, softening or even the combination of both effects. Non-linear phenomena such as internal resonances and bifurcation points, which may lead to secondary branches, are studied.

An introduction to the Molecular Dynamic algorithm is presented, and this algorithm is used to calculate the natural frequencies of a carbon nanotube. The results are then compared to the ones derived with the developed continuum model in an attempt to establish a correct value for the nonlocal parameter of the nanotube analysed.

Keywords: Nanobeams; Electrostatic actuation; Non-linear modes of vibration; Non-linear frequencies; Nonlocal effects; Internal resonance; Molecular Dynamics

Acknowledgements

I would like to thank my supervisor Prof. Pedro Leal Ribeiro for his guidance and support, and especially for sharing with me all his knowledge without which this dissertation would not have been possible.

I would like to thank Dr. Hamed Akhavan for all his help during the time this work took place, and for all the fruitful conversations we shared that in many ways helped me complete this work.

I would like to thank all my friends that walked this journey with me, in particular, André Leite, Luís Varandas and Tomás Chuaqui, for all the support and advice and for all the good moments we shared that make these last five years absolutely memorable.

I would like to thank Ricardo Lopes for his friendship and guidance, and for always being there for me in both good and bad moments.

I would like to thank my family, in particular my parents Jorge and Maria Alves for their unconditional love and support.

A special thanks to my brother Paulo Alves for his friendship and scientific guidance, and for being a true inspiration to me.

Finally, I would like to thank my girlfriend Beatriz for all her love, support, for believing in me and for giving me the confidence to overcome any obstacle.

CONTENTS

LIST OF FIGURES

List of Tables

List of Symbols

Roman and Greek symbols

u	longitudinal displacement along the x axis;
w	transverse displacement along the z axis;
ϕ	rotation displacement along the y axis;
ξ	natural coordinate;
t	time variable;
$t_i(\xi)$	longitudinal shape function;
$f_i(\xi)$	transverse shape function;
$g_i(\xi)$	rotation shape function;
$s_i(t)$	time variation function of the longitudinal displacement;
$q_i(t)$	time variation function of the transverse displacement;
$r_i(t)$	time variation function of the rotation displacement;
p_l	number of longitudinal shape functions;
p_o	number of transverse shape functions;
p_t	number of rotation shape functions;
σ_{xx}	normal stress;
τ_{xz}	transverse shear stress;
ϵ_{xx}	normal strain;
γ_{xz}	shear strain;
V	potential energy;
T	kinetic energy;
W_{nc}	work of the non-conservative forces;
N_x	normal resultant force;
Q_x	transverse shear force;
M_x	bending moment;
ρ	density;
A	cross-sectional area;
I	second moment of area;
r	radius of gyration;
E	Young's modulus;

G	shear modulus;
k_s	shear correction factor;
v	Poisson's ratio;
L	beam length;
h	beam thickness;
b	beam width;
d	gap size - distance between the beam and the stationary electrode;
f_e	electrostatic force;
ϵ_0	vacuum permittivity;
V	DC tension/voltage;
ζ	binary auxiliary parameter;
$t_{i,j}(x)$	classical macroscopic stress tensor;
$k(\|x' - x\|, \tau)$	attenuation function;
μ	nonlocal parameter;
W_i	amplitude of the *i-th* harmonic;
ω	frequency;
ω_i	*i-th* natural frequency;
ω_{bif}	bifurcation point frequency;
T	period of vibration;
s	arc length;
V	DC tension/voltage;
$\dot{w}$	transverse velocity;
Ω	non-dimensional frequency;
η	non-dimensional nonlocal parameter;
$\bar{L}$	non-dimensional beam length;
β	non-dimensional beam width;
$\bar{d}$	non-dimensional gap size;
$\bar{w}$	non-dimensional transverse displacement;
$\bar{W}_i$	non-dimensional amplitude of the *i-th* harmonic;
m_i	mass of the *i-th* atom;
ΔV	gradient of the potential energy;
λ_i	*i-th* eigenvalue.

Matrices and Vectors

$\mathbf{d}$	vector of the displacement components;
$\mathbf{N}$	shape function matrix;
$\mathbf{q}$	vector of the generalized displacements;
$\mathbf{t}$	vector of the longitudinal shape functions;

$\mathbf{f}$	vector of the transverse shape functions;
$\mathbf{g}$	vector of the rotation shape functions;
$\mathbf{M}_{local}$	mass matrix;
$\mathbf{M}^{w}$,$\mathbf{M}^{\phi}$	mass matrix associated with the transverse and rotation inertia;
$\mathbf{M}_{n-local}$	nonlocal mass matrix;
$\mathbf{M}^{\mu w}$,$\mathbf{M}^{\mu\phi}$	nonlocal mass matrix associated with the transverse and rotation inertia;
$\mathbf{K}_{l}$	linear stiffness matrix;
$\mathbf{K}_{p}$	longitudinal stiffness matrix;
$\mathbf{K}_{b}$	bending stiffness matrix;
$\mathbf{K}_{\gamma i,j}$	shear stiffness matrix;
$\mathbf{K}_{nl-local}$	non-linear stiffness matrix;
$\mathbf{K}_{2}^{1}$,$\mathbf{K}_{3}^{1}$	1^{st} order non-linear local stiffness matrix;
$\mathbf{K}_{4}^{2}$	2^{nd} order non-linear stiffness matrix;
$\mathbf{K}_{nl-n-local}$	non-linear nonlocal stiffness matrix;
$\mathbf{K}_{5}^{1}$	1^{st} order non-linear nonlocal stiffness matrix;
$\mathbf{K}_{6}^{2}$	2^{nd} order non-linear nonlocal stiffness matrix;
$\mathbf{v}_{fe}$	vector - elec. force;
$\mathbf{K}_{fe}^{0}$	2^{nd} linear stiffness matrix - elec. force;
$\mathbf{K}_{fe}^{i}$	*i-th* order non-linear stiffness matrix - elec. force;
$\mathbf{K}_{\mu fe}^{0}$	2^{nd} linear nonlocal stiffness matrix - elec. force;
$\mathbf{K}_{\mu fe}^{i}$	*i-th* order non-linear nonlocal stiffness matrix - elec. force;
$\mathbf{q}_{u}(t)$	vector of longitudinal displacements;
$\mathbf{q}_{w}(t)$	vector of transverse displacements;
$\mathbf{q}_{\phi}(t)$	vector of rotation displacements;
$\ddot{\mathbf{q}}_{u}(t)$	vector of longitudinal accelerations;
$\ddot{\mathbf{q}}_{w}(t)$	vector of transverse accelerations;
$\ddot{\mathbf{q}}_{\phi}(t)$	vector of rotation accelerations;
$\mathbf{KL}_{w}(t)$	vector of rotation displacements;
$\mathbf{KL}_{\phi}^{1}$,$\mathbf{KL}_{\phi}^{2}$	matrix containing all linear stiffness terms related to ϕ;
$\mathbf{KL}_{w}^{1}$,$\mathbf{KL}_{w}^{2}$	matrix containing all linear stiffness terms related to w;
$\mathbf{M}_{lw}$	mass matrix containing local and nonlocal terms related to w;
$\mathbf{M}_{l\phi}$	mass matrix containing local and nonlocal terms related to ϕ;
$\mathbf{K}_{w}$	matrix containing all stiffness terms related to w;
$\mathbf{u}_{i}(t)$	*i- th* vector of the harmonics coefficients;
$\mathbf{M}_{HBM}$	mass matrix used in the HBM;
$\mathbf{K}_{HBM}$	stiffness matrix used in the HBM;
$\mathbf{f}_{HBM}$	vector containing all non-linear terms used in the HBM;
$\mathbf{f}_{el}$	vector - elec. force used in the HBM;
$\mathbf{F}_{i,HBM}$	vector of non-linear terms used in the HBM;
$\boldsymbol{w}_{i}$	solution vector of the i-th iteration;

$\mathbf{J}$	Jacobian matrix;
$\mathbf{f}_r$	vector of residual forces;
$\mathbf{F}_i$	force applied on the *i-th* atom;
$\mathbf{r}_i$	position of the *i-th* atom;
$\mathbf{v}_i$	velocity of the *i-th* atom;
$\mathbf{a}_i$	acceleration of the *i-th* atom;
$\boldsymbol{\phi}_i$	*i-th* eigenvector.

In this dissertation, the matrices are represented by bold upper case letters, and vectors are generally represented by bold lower case letters.

Abbreviations

NEMS	Nanoelectromechanical system;
MEMS	Microelectromechanical system;
CNT	Carbon nanotube;
SWCNT	Single walled carbon nanotube;
MWCNT	Multi walled carbon nanotube;
MD	Molecular dynamics;
HBM	Harmonic balance method;
FEM	Finite element method;
ATK	Atomistix ToolKit;
vdW	van der Waals;
CC	double clamped boundary condition;
SS	Simply supported boundary condition;

CHAPTER 1

INTRODUCTION

1.1 GENERAL OVERVIEW AND MOTIVATION

Micro electromechanical systems (MEMS) had a great development when micro-machining technology was introduced in the industry, allowing new manufacturing techniques to fabricate micro scaled devices with high precision. MEMS became so attractive over their macroscopic counterparts, due to their small size and weight, low power consumption and compatibility with integrated circuit processes, which allows the fabrication of a very high number of MEMS devices on a single wafer with an associated low cost. These devices can easily be combined directly with electronic components without the need of any complicated electrical system, reducing the electrical noise, increasing precision and stability. Some successful examples of MEMS applications are accelerometers used in airbags, micro-pressure transducers and micro-mirror arrays in plasma TVs, microphones in cell phones and inertia sensors used in video game controllers. There are also many micro-sensing and micro-actuating devices that have been produced, although they are still under extensive development [1].

With the evolution of high precision manufacturing techniques, and with the pressure to produce even smaller devices, MEMS are being miniaturized day by day, and are now deep in the sub-micrometer range giving birth to what are called nanoelectromechanical systems (NEMS). These electromechanical devices are envisioned for many applications as well as to access interesting and new regimes in fundamental physics, which will open a vast number of exploratory research areas in science and engineering. Some envisioned applications for NEMS are mass and force sensing, nano-switches, nano-actuators and molecules or cell detection, which could be important in specific disease diagnosis. Knowing the resonant frequencies and other dynamic characteristics is key to the success of NEMS in the applications mentioned. There are some technological challenges

when it comes to operating these nanoelectromechanical systems (NEMS), being the actuation and detection of their sub-micrometer displacement at high frequencies, some of them [1].

Most MEMS and NEMS devices employ a structure that undergoes some sort of motion. Understanding the motion of these devices is a challenging task, since when actuated they are submitted to large deflections when compared to their dimensions, which introduces geometric non-linearities. Many devices are actuated electrostatically, and adding to the geometric non-linearity, this force is a highly non-linear function of the distance between the two electrodes involved, which further enriches the dynamic behaviour of MEMS and NEMS [2].

Electric forces introduce an instability called ”pull-in”, which occurs when the internal elastic force of the beam can no longer resist the opposing electric force, causing it to collapse to the electrode. This instability is another obstacle to overcome when simulating and predicting the dynamic behaviour of electrically actuated devices [2].

Linear modelling and analysis is inadequate to capture the dynamics of non-linear systems, producing misleading predictions of their mechanical behaviour. Thus, a model that takes into account the non-linearities of these systems, becomes necessary to accurately simulate them. Different approaches have been proposed to simulated the dynamic behaviour of micro and nanobeams, from lumped spring-mass based system, to generic software based on finite element methods (FEM). These FEM programs use numerous variables to represent these type of systems, and have the shortcoming of being complex and demanding huge computational costs [3].

The study of undamped non-linear free vibrations is essential to understand the system’s vibratory response in the non-linear regime. Furthermore, resonances that take place in forced responses occur in the neighbourhood of the free vibration oscillations. This way, the analysis of free vibration oscillations provides an important insight on the dynamic behaviour of the system, which is of use when the system is actuated by almost any force.

1.2 Literature Review

1.2.1 Modelling of small scale systems

Nanotechnology is currently a subject of scientific and technological interest, and accordingly to many researchers, there are three main techniques to study nanostructures numerically: quantum mechanics, molecular dynamics (MD) and continuum models. Quantum mechanics has not been successful in representing the mechanical behaviour of small sizes structures maybe due to its limited results and applications. It was mainly used to study the structures of nano materials in basic sciences [4]. On the

other hand, molecular dynamics has been extensively used in nano mechanics. It is a numerical simulation method which allows the atoms and molecules to interact for a fixed period of time, and by simply solving the Newton's equations of motion, it's able to give an overall view of the dynamical evolution of the system in study. By using MD simulations, one can determine mechanical characteristics of nanostructures, such as thermal properties, natural frequencies, buckling loads, etc. Despite the potentiality of the atomistic simulations, they can't be used to model a complicated system due to the high computation resources that would be necessary to carry out the simulations [5–7]. In order to overcome this limitation, researches used continuum modelling techniques, applying classical elasticity theories (beam, plate, shell) to replicate the mechanical behaviour of the components used in nanotechnology. Some experiments revealed that these classical elasticity theories were not able to correctly predict the behaviour of micro and nanostructures on their own. In order to solve this problem, nonlocal continuum theories were developed, taking into account the inter atomic forces, and the internal length scales were introduced into the constitutive equations as well as a material parameter.

Eringen [8], developed a non local elasticity theory, which has been used as the basis of many studies related to the behaviour of micro and nano sized structures. Reddy [9], reformulated the Euler-Bernoulli, Timoshenko, Reddy and Levinson beam theories using the nonlocal differential constitutive relations of Eringen, and studied the deflection and the fundamental natural frequency of nanobeams. Roque et al. [10], applied the nonlocal elasticity theory of Erigen to study bending, buckling and free vibration of Timoshenko nanobeams. The authors used a meshless method to derive the numerical solutions which were then compared to with the available analytical solutions.

Wang et al. [11], applied the nonlocal elasticity constitutive equations and the Timoshenko beam theory to study the influence of the nonlocal parameter in the vibration of single-walled carbon nanotubes (SWCNT). Wang [12], studied wave propagation in carbon nanotubes with both the Timoshenko and Euler-Bernoulli beam theories, considering the nonlocal elasticity of Eringen. Reddy and Pang [13], used the Euler-Bernoulli and the Timoshenko beam theories to calculate the deflection, bending and natural frequencies for different boundary conditions, concluding that the Timoshenko beam theory is more sensitive to changes in the nonlocal parameter.

Ansari and Sahmani [14], used MD simulations to calculate the natural frequencies of CNT's with different types of chirality (armchair and zigzag) and boundary conditions. After comparing the results obtained with MD simulations with the results obtained with nonlocal continuum theories, they concluded that the natural frequencies are lower for higher values of the nonlocal parameters.

1.2.2 Micro and nanoelectromechanical systems - MEMS and NEMS

One feature about MEMS and NEMS is that they are extensively used as sensors and actuators. Most sensors where these devices are used are resonant sensors, which offer attractive advantages over the other conventional counterparts, such as low-power consumption, high sensitivity and resolution and long term stability. Resonant nanobeams can be referred as resonators, and are the transducers in resonant sensors. The beams' natural frequencies are sensitive to axial strains, and since external loads induced by pressure, temperature or acceleration, lead to the appearance of axial strains in the beam, these physical quantities can be measured by detecting the shift in the natural frequencies [2].

Silicon represents the core material of MEMS devices. In NEMS devices, silicon is also extensively used, however, carbon nanotubes and graphene sheets are being intensively studied and present great potential for different applications in this area. Silicon is the chosen material for these devices due to its excellent thermal and mechanical properties, such as high melting point, small thermal expansion, and brittleness with no plastic behaviour. Silicon substrates are the platform where MEMS and NEMS devices are built. The fabrication normally starts with a single crystal of silicon, which is normally used directly in NEMS scales [1,2].

Due to their small size and extremely light weight, MEMS and NEMS actuation methods demand very low power. Some of the existing methods include thermal, magnetomotive, piezoelectric and electrostatic actuation [15].

Thermal actuation is used for bilayer structures with different thermal expansion coefficients. When heated, this structure is subjected to stresses due to the differential thermal expansion between the layers. The bandwidth of thermal actuation techniques depends upon the thermal time constant of the structures, given that the structure has to cool and return to its initial shape before its submitted to the next heat pulse. For the magnetomotive actuation, a Lorentz force is generated by a current-carrying conductor in a stationary magnetic field, which supplies the actuation force [15].

Piezoelectric actuation is still an unexplored phenomenon but with potential in actuation of NEMS. When an external electric field is applied in a piezoelectric material, it responds by deforming. This phenomena is know as the "inverse effect". The effectiveness of this type of actuation depends on the relaxation time of the deformation after the electric field is removed, and also in the charging time of the actuation circuit that produces the electric field [15] .

Electrostatic actuation, among the other techniques, is the most common and well-developed method. Electrostatic actuators can use only DC voltages, or combine DC and AC voltages, although in this work only DC electrostatic actuation will be considered. This type of actuation offers a well controlled force over the several nanometres of

displacement, and requires very low current. This force is exerted on a mechanical element, like a beam, causing it to serve different functions, such as vibrating at resonance or just to move back and forth, depending on the type of device considered [2, 3, 15].

There are different factors that set the dynamics of electrostatic MEMS and NEMS devices to the non-linear regime. Parallel-plate electric forces are inherently non-linear since they are inversely proportional to the square of the distance between the capacitor plates. These electric forces produce large deflections when acting on such small scaled components, which in turn introduce geometric non-linearities, such as mid-plane stretching in beams of immovable ends. The mid-plane stretching of nanobeams, shifts the natural frequencies to higher values, while the electrostatic force tends to shift them to lower values. The deflected beam can experience softening or hardening behaviour, depending on whether the electrostatic force dominates mid-plane stretching or not. A hardening behaviour is defined by an increase of the natural frequency as the amplitude of vibration increases, while in softening behaviour, the frequency decreases.

The electric actuation of small scaled devices introduces a structural instability known as "pull-in". The combined AC and DC electric load has an upper limit beyond which the internal elastic restoring force of the beam can no longer balance it, leading to a continuous increase in the deflection of the beam, which in turn leads to a stronger attraction force in a positive feedback loop. This instability leads to a physical contact between the beam and the immovable electrode. The critical tension associated with this instability is know as the "pull-in voltage".

MEMS and NEMS devices have experienced a significant growth in the past decade, however, during its development some challenges arise, such as the fabrication of the devices, the actuation and detection of their sub micrometer displacements at high frequencies. The way these challenges are overcome, will determine the commercial success of NEMS and MEMS in both technical and economic terms.

Some research has been carried out in the dynamics of electrostatically actuated NEMS. For instance, Dequesnes et al. [16] studied the pull-in instability in several CNT's. The authors derived an expression for the force considering that this force is exerted by a plane on a cylinder. Ke et al. [17] derived a similar expression for the force, confirming that the geometric non-linearity has a relevant effect on the pull-in tension. Mojahedi et al. [18] studied the static pull-in instability of electrostatically actuated micro-cantilevers considering different non-linear effects. Galerkin's method was used in order to convert the non-linear differential equations of motion into non-linear algebraic equations, and obtained the solutions for the static deflections using the homotopy perturbation method. Fakhrabadi et al. [4] used the nonlocal elasticity theory to investigate the deflection and instability of electrostatically actuated CNT's for different boundary conditions. They studied the influence of the geometry and the nonlocal parameter in the pull-in voltage. Krylov [19] made a stability analysis of microbeams actuated by an electrostatic force with non-linear squeeze film damping, by evaluating the largest Lyaponov exponent, the

sign of which defines the character of the response. Choi and Lovell [20] calculated the static deflection of a microbeam , using the shooting method. Their model accounts for both the electrostatic force and the geometric non-linearity.

Ahn et al. [21] studied a microbeam under electrostatic actuation as a single degree-of-freedom system. The model considered a linear spring, neglecting the mid-plane stretching. They derived an expression that relates the fundamental natural frequency with the applied DC voltage, and concluded that an increase in the voltage leads to lower values of the fundamental natural frequency.

Kacem et al. [22] investigated the non-linear dynamics of NEMS resonant sensors around their primary resonance. The authors developed an analytical model based on the Galerkin decomposition method coupled with the averaging method, to study the dynamics os the system and also took in to account fringing field effects. Ouakad and Younis [23] investigated the dynamic behaviour of double clamped micro-machined arches when actuated by a small DC electrostatic load superimposed to an AC harmonic load. Galerkin's method was used to derive a reduced-order model where the natural frequencies and mode shapes of the arches were calculated for various values of DC voltages and initial rises.

Motion Detection in NEMS

The detection the small displacements that occur at the nano scale presents a very challenging task, since their detection requires transducers with extremely high sensitivity. Since the frequency at which NEMS devices vibrate are in the order of Teraherts (THz), a large transduction bandwidth is essential. This topic is not connected directly to the objective of this dissertation, however, for the sake of completeness and due to their relevance, some motion detections techniques used for NEMS devices are presented next.

— **Magnetomotive Technique** - the magnetomotive displacement technique was first introduced in the NEMS domain in 1996. It's based in the presence of a uniform magnetic field in which a NEMS device is in motion, causing the electromagnetic flux to vary in time, generating an electromotive force in the loop. This force, in turn, can be detected by a circuit and converted to a displacement measurement [15];

— **Optical Techniques** - optical interferometry techniques are very popular in the detection of small scaled displacements. A focused laser beam is split into one reference beam and one beam that reflects on the surface of the NEMS device. When these two beams interfere with each other a pattern of fringes appear due to the differences in both phases of the beams. The pattern is then analysed and the displacements of the device can be determined;

— **Piezoresistive and Piezoelectric Detection** - both piezoresistive and piezoelectric

detection are sensitive to the strain generated during the motion of a NEMS device rather then the actual displacement itself. Piezoresistive materials change their resistivity when strain is applied, and piezoelectric materials exhibit a potential drop when the same strain is applied. Piezoresistive sensing is realized by measuring the changes of resistance of a piezoresistive NEMS in motion. There is a considerable challenge in this approach, since the resistance change in the NEMS device is very low, and are usually even harder to detect at high resonance frequencies that are typical in these devices [15]. On the other hand, in piezoelectric NEMS, the polarization fields created by the strain are explored. The detection is realized by a highly sensitive measuring of the potential drop across the strained device. This technique faces the same challenges of the piezoresistive one, since the voltage generated across the nano scaled system is very small. The detection of this potential field becomes even more challenging at high frequencies [15].

1.2.3 NON-LINEAR DYNAMICS

Linear systems are generally approximations of real systems and present limited applications. The majority of natural systems are non-linear, and the correct dynamic description of these systems is far more complex than linear ones. Several type of non-linearities exist in mechanical systems, such as material, geometric, inertial and also non-linear external forces. In this dissertation, only the geometric non-linearity and non-linear external forces are considered.

Non-linear systems are often represented by non-linear partial differential equations, which are generally treated by two different approaches. In the first approach, the partial differential equations are discretized by a variational method or by a weight-residual method, and in the second approach, the equations are treated directly in a numerical or analytical way [24].

Knowing the modes of vibration is essential to understand and to accurately describe the dynamic behaviour of any system. In linear conservative systems, a mode of vibration is defined by a natural frequency and a mode shape that remain unchanged during the vibration cycle. In a non-linear system, this is no longer true. The definition of a mode of vibration in a non-linear system is not unique, and different authors have different interpretations. However, in this dissertation a non-linear mode is interpreted as a periodic oscillation motion, not necessarily harmonic, where the correspondent shape and frequency are amplitude dependant. This way, the mode shape and frequency are constantly changing during the oscillation motion, which means that a non-linear mode can't be characterized by a single shape or frequency. Despite this fact, in most cases non-linear mode shapes are similar to the linear shapes, and when the amplitudes of vibration tend to low values, the non-linear shape actually assumes the linear mode shape.

Since the natural frequencies are constantly changing during an oscillation cycle,

two or more natural frequencies may become commensurable, and conditions for the interaction of the modes involved can be created. This phenomenon is known as internal resonance, and energy exchanges between the interacting modes occur, leading to multi mode vibration and to significant changes of the mode shapes [25].

Previous theoretical and experimental studies showed that the mechanical behaviour of nanostructures is non-linear when they are subjected to large external loads [26]. It is also known that when a beam with fixed end supports undergoes transverse vibration, an axial tension is produced, which is non-linearly proportional to the amount of lateral deflection of the beam, causing it to vibrate in the non-linear regime.

Lewandowski [27] studied the non-linear vibrations of beams, applying the harmonic balance method and a continuation method with an arc-length restrain. Benamar [28] presented an analytical solution for calculating the non-linear mode shapes and natural frequencies of a double clamped beam at large vibration amplitudes.

Ribeiro and Petyt [29] used a *p*-version of the finite element method and the harmonic balance method to study the geometrically non-linear free and steady-state forced vibrations of uniform slender beams. The von Kármán's non-linear strain-displacement relationships were employed, and a continuation method was used to solve the equations of motion. The authors found a 1:3 and 1:5 internal resonances and discussed their consequences. Stoykov and Ribeiro [30] studied the geometrical non-linear free vibrations in space of beams with rectangular cross section, using the *p*-version finite element method. Their model was based on the Timoshenko's theory and the authors employed the harmonic balance method to derive the non linear algebraic equations of motion, and then solved them by a continuation method. Several harmonics were considered to study the periodic motions and internal resonances were also investigated.

Fang et al. [31] have examined size-dependent non-linear vibration of DWCNTs by using the harmonic balance method and DavidonFletcherPowell method.

Fu et al. [32] applied a multiple elastic beam model to study the non-linear free vibration of embedded multi-wall CNT, taking in consideration the effect of the surrounding elastic medium, and van de Waals forces. The authors used the incremental harmonic balance method to derive the frequency domain equations of motion.

Yang and Kitipornchai [33], studied the non-linear free vibration of Single Walled carbon nanotubes (SWCNT) based on von Kármán's geometric non-linearity, Timoshenko beam theory and Eringen's nonlocal elasticity theory. The elastic properties of the CNTs where obtained using MD simulations, and the influence of the nonlocal parameter in the non-linear frequencies was studied for different boundary conditions. Ansari et al. [34], used the Timoshenko beam theory to study the non-linear vibration of embedded multi-walled carbon nanotubes in thermal environments. The authors considered the van der Waals force existing between adjacent and non-adjacent nested

nanotubes and solved the non-linear equations using the harmonic balance method.

1.3 OBJECTIVES

In non-linear problems, the natural modes of vibration provide key information for the correct understanding of the dynamic behaviour of a structure. In the present work, it is intended to investigate the non-linear dynamic behaviour of rectangular cross section nanobeams under DC electrostatic actuation, however, since the developed model is applicable for symmetrical cross shaped beams, some attention is given to study linear and non-linear vibrations of carbon nanotubes. In order to do so, a continuum mechanics p-version finite element method, which takes into account the geometric and electrostatic non-linear effects, is presented. The model is based on the Timoshenko beam theory in order to be able to accurately model both short and long beams. The nonlocal elasticity of Erigen is introduced in the model, to consider the small size effects that exist in nano scales. The nonlocal effects of the electrostatic force were also taken into account. The Galerkin method and the harmonic balance method (HBM) are applied in order to derive the frequency domain equations of motion, which are then solved by an arc-length continuation method. Several harmonics for the response are considered, to analyse the influence of the higher harmonics in the oscillations of a nanobeam.

1.4 THESIS OUTLINE

In chapter 2, the mathematical formulation of the p-version finite element model is presented as well as the techniques used to solve the non-linear partial differential equations of motion.

In chapter 3, the different aspects of the model are verified, comparing its results to the ones existing in the literature.

In chapter 4, a complete analysis of the dynamic behaviour of an electrostatically actuated nanobeam with different boundary conditions is made. The influence of fringing fields and geometric properties in the dynamic behaviour of the nanobeam are studied. Furthermore, internal resonances, bifurcation points and secondary branches are also explored.

In chapter 5 an introduction to Molecular Dynamic (MD) simulations is made. Some simulations of this type were carried out to calculate the Young Modulus and linear vibrations of carbon nanotubes, and the results were compared with the ones derived with the continuum model.

In chapter 6 the main conclusions of the dissertation and proposed future work are presented.

CHAPTER 2

MATHEMATICAL FORMULATION

2.1 INTRODUCTION

In this chapter a mathematical model for non-linear vibration of nanobeams is presented. The model is based on a *p*-version of the finite element method and in the Timoshenko's beam theory, which takes into account shear deformation and rotational inertia effects, making it suitable for describing the behaviour of both thick and slender beams. The beam analogue of the von Kármán's plate theory is considered to take into account the geometrical non-linear effects, and Erigen's non-local constitutive relations are used to include small scale effects in the model. The beam's material is considered to be elastic and isotropic, and the equations of motion derived are applicable to any symmetrical cross shaped beam, so both rectangular section beams and CNTs can be accurately modelled.

The partial differential equations of motion were discretized using Galerkin's method, and the solution of the resulting non-linear ordinary differential equations were assumed to be periodic. This way the harmonic balance method finds its natural application, and a set of algebraic non-linear equations are derived, which are then solved by an arc-length based continuation method.

2.2 *p* -VERSION OF THE FEM

The Finite Element Method (FEM) is a numerical technique that is used to solve partial differential equations, by approximating the solution by means of admissible functions called shape functions. In the *h*-version of the FEM a large problem is divided into smaller and simpler parts that are called finite elements. This way, the set of equations that model each element are assembled into a larger system of equations which in turn model the

initial problem. In order to obtain better approximations with this version of the FEM, the initial problem must be subdivided into more finite elements, creating what is usually called a more refined mesh.

In this dissertation the *p*-version of the FEM was used. In this version, the mesh is maintained constant and the accuracy is achieved by increasing the number of admissible functions over each element. In the present work, the beams are modelled with only one element, however one could still use the *p*-version approach and consider more than one element in the mesh. The combination of both presented versions is called the *hp* version of the finite element method.

The *p*-version has some advantages over the *h*-version such as [29, 30, 35–37]:

— simple structures can accurately be modelled using only one element avoiding the assemblage of elements;

— the *p*-version gives more accurate results with fewer degrees of freedom than the *h*-version, presenting higher rates of convergence.

2.3 MATHEMATICAL MODEL

2.3.1 TIMOSHENKO BEAM THEORY

The Timoshenko beam theory takes into account shear deformation and rotational inertia effects, which makes it suitable to describe the behaviour of short beams. This way, the theory considers that the cross section of a deformed beam does not remain perpendicular to its axis or reference line.

In linear beam theories, the strain of the reference line is neglected since the magnitude of the transverse deflection is small. When the magnitude of this displacement is on the order of the beam thickness, this strain can no longer be ignored, since it produces a longitudinal force that appreciably helps in resisting lateral loads. In these situations it is necessary to consider the geometric non-linearity which is introduced to the strain-displacement relation.

Based on the Timoshenko beam theory, the displacements of an arbitrary point in the beam along the x-axis are,

$$\begin{cases} u_1(x,z,t) = u(x,t) + z\phi(x,t) \\ u_2(x,z,t) = 0 \\ u_3(x,z,t) = w(x,t) \end{cases} \tag{2.1}$$

where $\phi(x,t)$, $u(x,t)$ and $w(x,t)$ are the rotation of the cross section, the axial and transverse displacement of the point x on the mid-plane of the beam.

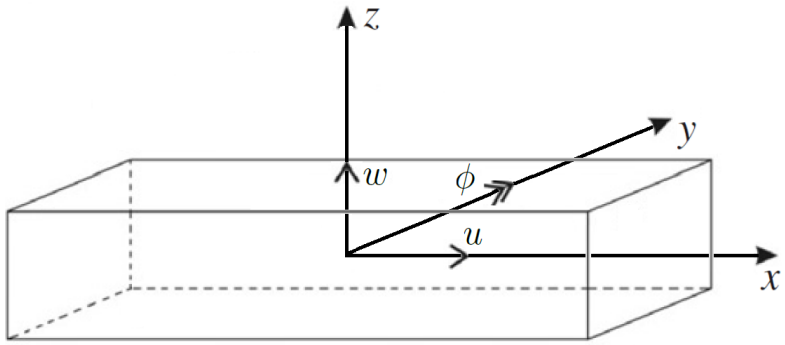

FIGURE 2.1: Axis and displacement components of the beam element.

The vector **d** is formed by the displacement components u, w and ϕ, and can be expressed as the product of the shape functions matrix, **N** and the vector of generalized nodal displacements **q**,

$$\mathbf{d}(x,t) = \begin{Bmatrix} u(x,t) \\ w(x,t) \\ \phi(x,t) \end{Bmatrix} = \mathbf{N}(x)\mathbf{q}(t) \tag{2.2}$$

$$\mathbf{N} = \begin{bmatrix} t_1, t_2, ..., t_{p_i} & \mathbf{0} & \mathbf{0} \\ \mathbf{0} & f_1, f_2, ..., f_{p_o} & \mathbf{0} \\ \mathbf{0} & \mathbf{0} & g_1, g_2, ..., g_{p_t} \end{bmatrix} = \begin{bmatrix} \mathbf{t}^T & \mathbf{0} & \mathbf{0} \\ \mathbf{0} & \mathbf{f}^T & \mathbf{0} \\ \mathbf{0} & \mathbf{0} & \mathbf{g}^T \end{bmatrix} \tag{2.3}$$

$$\mathbf{t}^T = \begin{bmatrix} t_1(x) & t_2(x) & ... & t_{p_i}(x) \end{bmatrix} \tag{2.4}$$

$$\mathbf{f}^T = \begin{bmatrix} f_1(x) & f_2(x) & ... & f_{p_o}(x) \end{bmatrix} \tag{2.5}$$

$$\mathbf{g}^T = \begin{bmatrix} g_1(x) & g_2(x) & ... & g_{p_t}(x) \end{bmatrix} \tag{2.6}$$

$$\mathbf{q}(t)^T = \begin{bmatrix} \mathbf{q}_u(t)^T & \mathbf{q}_w(t)^T & \mathbf{q}_\phi(t)^T \end{bmatrix} \tag{2.7}$$

The number of longitudinal, transverse and rotational shape functions are defined by p_l, p_o and p_t respectively. Only the shape functions that satisfy the geometric boundary conditions are included in the model, and in this dissertation only simply supported (SS) and double clamped (CC) beams were considered. The shape functions used are derived from the Rodrigues' form of the Legendre polynomials [29, 35, 36].

The shape functions g_i and t_i, which are related to the rotation and longitudinal displacements respectively, are given by,

$$g_{r-2} = \sum_{n=0}^{int(r/2)} \frac{(-1)^n (2r-2n-5)!!}{2^n n!(r-2n-1)!} \xi^{r-2n-1}, \quad r > 2 \tag{2.8}$$

The shape functions f_i, related to the transverse displacements, are given by,

$$f_{r-2} = \sum_{n=0}^{int(r/2)} \frac{(-1)^n (2r-2n-7)!!}{2^n n!(r-2n-1)!} \xi^{r-2n-1}, \quad r > 4 \tag{2.9}$$

with $r!!$ representing the double factorial operator and $int(r/2)$ the integer part of $r/2$. The set of shape functions presented only satisfy double clamped boundary conditions. In order to consider a simply supported case, other shape functions must be added to the set of shape functions f, like third-order polynomials.

Since the transverse deflection is large compared with the beam thickness (leading to geometrical non-linearity) and yet very small when compared to the length $L(w << L)$, the beam analogue of the von Kármán's plate theory can be applied. The strain-displacement relationship can be expressed as follows,

$$\epsilon_{xx}(x,t) = \frac{\partial u(x,t)}{\partial x} + \frac{1}{2}\Big(\frac{\partial w(x,t)}{\partial x}\Big)^2 + z\frac{\partial \phi(x,t)}{\partial x} \tag{2.10a}$$

$$\gamma_{xy}(x,t) = \frac{\partial w(x,t)}{\partial x} + \phi(x,t) \tag{2.10b}$$

In order to obtain the equations of motion in terms of the generalized displacements, the Hamilton's principle can be used. Since the stress resultants are expressed in terms of the generalized displacements, we can express the potential energy V as,

$$V = \int_L \int_A (\sigma_{xx}\epsilon_{xx} + \sigma_{xz}\gamma_{xz}) dA dx \tag{2.11}$$

where A is the cross-section area of the beam, σ_{xx} and σ_{xz} are the normal and shear stresses, respectively. By replacing the strain-displacement relations of the Eq. (2.10) in Eq. (2.11), the potential energy can be written as follows,

$$\begin{aligned} V &= \frac{1}{2}\int_L \int_A \left[\sigma_{xx}\Big[\frac{\partial u}{\partial x} + \frac{1}{2}\Big(\frac{\partial w}{\partial x}\Big)^2\Big] + \sigma_{xx} z\frac{\partial \phi}{\partial x} + \sigma_{xz}\Big(\frac{\partial w}{\partial x} + \phi\Big)\right] dA dx \\ &= \frac{1}{2}\int_L \left[N_x\Big[\frac{\partial u}{\partial x} + \frac{1}{2}\Big(\frac{\partial w}{\partial x}\Big)^2\Big] + M_x\frac{\partial \phi}{\partial x} + Q_x\Big(\frac{\partial w}{\partial x} + \phi\Big)\right] dx \end{aligned} \tag{2.12}$$

where the normal force N_x, the transverse shear force Q_x and the bending moment M_x are calculated from,

$$N_x = \int_A \sigma_{xx} dA, \quad Q_x = \int_A \sigma_{xz} dA \quad M_x = \int_A \sigma_{xx} z dA \tag{2.13}$$

The kinetic energy T, can be calculated from,

$$T = \frac{1}{2} \int_L \left[\rho A \Big(\frac{\partial u}{\partial t} \Big)^2 + \rho A \Big(\frac{\partial w}{\partial t} \Big)^2 + \rho I \Big(\frac{\partial \phi}{\partial t} \Big)^2 \right] \tag{2.14}$$

where ρ is the mass density of the beam material and I is the second moment of area.

Since the nanobeam is going to be submitted to an electrostatic actuation, an external force f_e must be considered. The virtual work of the non-conservative forces, δW_{nc}, is defined by,

$$\delta W_{nc} = \int_L f_e \delta w dx \tag{2.15}$$

Equations of Motion

Hamilton's principle states the following,

$$\int_{t_1}^{t_2} (\delta T - \delta U) dt + \int_{t_1}^{t_2} \delta W_{nc} dt = 0 \tag{2.16}$$

Substituting the potential and kinetic energy in Hamilton's principle, integrating by parts and setting the variational coefficients δu, δw, $\delta \phi$ to zero, one arrives at the equations of motion in terms of the generalized stresses.

$$\frac{\partial N_x}{\partial x} = 0 \tag{2.17a}$$

$$\frac{\partial Q_x}{\partial x} + \frac{\partial}{\partial x} \Big(N \frac{\partial w}{\partial x} \Big) + f_e = \rho A \frac{\partial^2 w}{\partial t^2} \tag{2.17b}$$

$$\frac{\partial M_x}{\partial x} - Q_x = \rho I \frac{\partial^2 \phi}{\partial t^2} \tag{2.17c}$$

In order to simplify the following equations, and since the longitudinal accelerations are much smaller than the other displacements, the longitudinal inertia term was neglected in Eq.(2.17a).

2.3.2 ERIGEN'S NONLOCAL ELASTICITY THEORY

Classical continuum models can describe the evolution of a macroscopic scaled system. The length scales associated with nanostructures are such, that in order to apply any continuum model, one needs to consider small length scales such as lattice spacing between atoms, which makes a consistent model formulation very challenging.

To overcome this challenge the nonlocal elasticity theory of Erigen has been proposed [8]. This theory takes account of remote forces between atoms, which causes the stress field at a specific point to depend not only on the strain at that point but also on the strains at all the surrounding points of the domain. This theory allows the use of continuum models, which provide a good alternative to atomistic simulations, which are known to be highly demanding in terms of computation.

Many authors studied the influence of small size effects in beams considering the nonlocal elasticity theory of Erigen, therefore, mathematical models for nanosized beams were developed [9,38,39].

The non-local stresses σ_{ij} are given by,

$$\sigma_{ij} = \int_V K(|x' - x|, \tau) t_{ij}(x') dx' \tag{2.18}$$

where $t_{ij}(x')$ is the macroscopic stress tensor at point x', the attenuation function $K(|x' - x|, \tau)$ expresses the nonlocal effects at point x caused by a strain at point x', with $|x' - x|$ representing the distance in Euclidean norm and τ is a material constant that depends on the internal and external characteristic lengths. The stress and strain, at a given point, is related by the generalized Hooke's Law,

$$\boldsymbol{t}(x) = \boldsymbol{C}(x) : \epsilon(x) \tag{2.19}$$

It is possible to represent the integral constitutive relations in a differential form,

$$(1 - \mu\nabla^2)\boldsymbol{\sigma} = \boldsymbol{t}, \quad \mu = (e_0 a)^2 \tag{2.20}$$

where e_0 is a material constant and a is the internal characteristic length.

By defining and operator $\mathcal{L}$, that is given by,

$$\mathcal{L} = 1 - \mu\nabla^2 \tag{2.21}$$

it is possible to approximate the nonlocal constitutive relations (Eq. 2.18) to a one dimensional form as [9],

$$\sigma_{xx} - \mu\frac{\partial^2\sigma_{xx}}{\partial x^2} = E\epsilon_{xx} \tag{2.22a}$$

$$\sigma_{xz} - \mu\frac{\partial^2\sigma_{xz}}{\partial x^2} = G\gamma_{xz} \tag{2.22b}$$

The set of equations of motion (Eq. 2.17) are the same as those for the classical Timoshenko beam theory; however, for a nonlocal theory the generalized stresses are different due to the nonlocal constitutive relation, and can be written as,

$$N_x - \mu\frac{\partial^2 N_x}{\partial x^2} = EA\left[\frac{\partial u}{\partial x} + \frac{1}{2}\Big(\frac{\partial w}{\partial x}\Big)^2\right] \tag{2.23a}$$

$$Q_x - \mu\frac{\partial^2 Q_x}{\partial x^2} = k_s GA\Big(\frac{\partial w}{\partial x} + \phi\Big) \tag{2.23b}$$

$$M_x - \mu\frac{\partial^2 M_x}{\partial x^2} = EI\frac{\partial \phi}{\partial x} \tag{2.23c}$$

where k_s is the shear correction used in the Timoshenko beam theory, in order to compensate for the error in assuming a constant shear strain through the thickness of the beam. It's value depends on the shape of the cross section of the beam [40, 41]. By substituting Eq. (2.17) into Eq. (2.23) the explicit expressions of nonlocal generalized stress resultants can be derived,

$$N_x = EA\left[\frac{\partial u}{\partial x} + \frac{1}{2}\Big(\frac{\partial w}{\partial x}\Big)^2\right] \tag{2.24a}$$

$$Q_x = k_s GA\Big(\frac{\partial w}{\partial x} + \phi\Big) + \mu\left[\rho A\frac{\partial^3 w}{\partial x \partial t^2} - \frac{\partial^2}{\partial x^2}\Big(N_x\frac{\partial w}{\partial x}\Big) - \frac{\partial f_e}{dx}\right] \tag{2.24b}$$

$$M_x = EI\frac{\partial \phi}{\partial x} + \mu\left[\rho I\frac{\partial^3 \phi}{\partial x \partial t^2} + \rho A\frac{\partial^2 w}{\partial t^2} - \frac{\partial}{\partial x}\Big(N_x\frac{\partial w}{\partial x}\Big) - f_e\right] \tag{2.24c}$$

Replacing the stress resultants by the their relation with the generalized displacements, the non-linear equations of motion are written as follows,

$$EA\Big(\frac{\partial^2 u}{\partial x^2}+\frac{\partial w}{\partial x}\frac{\partial^2 w}{\partial x^2}\Big)=0 \tag{2.25a}$$

$$\rho A\frac{\partial^2 w}{\partial t^2}-k_sGA\Big(\frac{\partial^2 w}{\partial x^2}+\frac{\partial \phi}{\partial x}\Big)-\mu\left[\rho A\frac{\partial^4 w}{\partial x^2\partial t^2}-\frac{\partial^3}{\partial x^3}\left(\frac{\partial w}{\partial x}\Big(EA\Big[\frac{\partial u}{\partial x}+\frac{1}{2}\Big(\frac{\partial w}{\partial x}\Big)^2\Big]\Big)\right)\right]$$
$$-\frac{\partial}{\partial x}\left[\frac{\partial w}{\partial x}\Big(EA\Big[\frac{\partial u}{\partial x}+\frac{1}{2}\Big(\frac{\partial w}{\partial x}\Big)^2\Big]\Big)\right]=f_e-\mu\frac{\partial^2 f_e}{\partial x^2} \tag{2.25b}$$

$$EI\frac{\partial^2 \phi}{\partial x^2}-k_sGA\Big(\frac{\partial w}{\partial x}+\phi\Big)=\rho I\frac{\partial^2}{\partial t^2}\Big(\phi-\mu\frac{\partial^2 \phi}{\partial x^2}\Big) \tag{2.25c}$$

In order to solve the partial differential equations written above, the Galerkin method can be applied, since it allows to derive ordinary differential equations which can then be solved. Accordingly to this method, the displacements u, w and ϕ can be written as follows,

$$\begin{cases} u(x,t)=\sum_{i=0}^{p_l} t_i(x)s_i(t) \\ w(x,t)=\sum_{i=0}^{p_o} f_i(x)q_i(t) \\ \phi(x,t)=\sum_{i=0}^{p_t} g_i(x)r_i(t) \end{cases} \tag{2.26}$$

where t, f, g are vectors of shape functions that define the spacial displacements along the length of the beam. The vectors s, q, r are formed by time dependent functions which describe the variation in time of the displacements of the beam.

Since the shape functions are defined by the natural coordinate ξ, the relation between the spacial variable x and ξ must be defined,

$$x=\frac{L}{2}\xi \tag{2.27a}$$

$$dx=\frac{L}{2}d\xi \tag{2.27b}$$

$$\frac{d}{dx}=\frac{2}{L}\frac{d}{d\xi} \tag{2.27c}$$

By multiplying the Eq. (2.25a) by the vector **t** and integrating each resulting term over the beam's domain, it's possible to derive the expressions for the mass and stiffness terms, that are related to the longitudinal displacement. If one proceeds in the same way for the other two equations, this time multiplying the vector **f** by Eq. (2.25b) and the vector **g** by Eq. (2.25c) all mass and stiffness terms can be calculated. The final expression

for all the mass and stiffness terms are presented next, however the integration by parts of these terms are presented in Appendix A.

Mass Matrices

Since the longitudinal inertia was neglected, the local mass matrix can be expressed in the form,

$$\mathbf{M}_{local} = \begin{bmatrix} \mathbf{0} & \mathbf{0} & \mathbf{0} \\ \mathbf{0} & \mathbf{M}^{w} & \mathbf{0} \\ \mathbf{0} & \mathbf{0} & \mathbf{M}^{\phi} \end{bmatrix} \tag{2.28}$$

$$\mathbf{M}^{w} = \frac{L}{2}\rho A \int_{-1}^{1} \mathbf{f}(\xi)\ \mathbf{f}(\xi)^{T} d\xi \tag{2.29a}$$

$$\mathbf{M}^{\phi} = \frac{L}{2}\rho I \int_{-1}^{1} \mathbf{g}(\xi)\ \mathbf{g}(\xi)^{T} d\xi \tag{2.29b}$$

The nonlocal mass matrix is the following,

$$\mathbf{M}_{n-local} = \begin{bmatrix} \mathbf{0} & \mathbf{0} & \mathbf{0} \\ \mathbf{0} & \mathbf{M}^{\mu w} & \mathbf{0} \\ \mathbf{0} & \mathbf{0} & \mathbf{M}^{\mu\phi} \end{bmatrix} \tag{2.30}$$

$$\mathbf{M}^{\mu w} = \frac{2}{L}\rho A \mu \int_{-1}^{1} \frac{\partial \mathbf{f}(\xi)}{\partial \xi} \frac{\partial \mathbf{f}(\xi)}{\partial \xi}^{T} d\xi \tag{2.31a}$$

$$\mathbf{M}^{\mu\phi} = \frac{2}{L}\rho I \mu \int_{-1}^{1} \frac{\partial \mathbf{g}(\xi)}{\partial \xi} \frac{\partial \mathbf{g}(\xi)}{\partial \xi}^{T} d\xi \tag{2.31b}$$

Stiffness Matrices

The linear terms of the stiffness matrix are not affected by the nonlocal parameter, so the linear stiffness matrix is given by,

$$\mathbf{K}_{l} = \begin{bmatrix} \mathbf{K}_{p} & \mathbf{0} & \mathbf{0} \\ \mathbf{0} & \mathbf{K}_{\gamma 22} & \mathbf{K}_{\gamma 23} \\ \mathbf{0} & \mathbf{K}_{\gamma 32} & \mathbf{K}_{\gamma 33} + \mathbf{K}_{b} \end{bmatrix} \tag{2.32}$$

$$\mathbf{K}_p = \frac{2}{L} EA \int_{-1}^{1} \frac{\partial \mathbf{t}(\xi)}{\partial \xi} \frac{\partial \mathbf{t}(\xi)}{\partial \xi}^T d\xi \tag{2.33a}$$

$$\mathbf{K}_b = \frac{2}{L} EI \int_{-1}^{1} \frac{\partial \mathbf{g}(\xi)}{\partial \xi} \frac{\partial \mathbf{g}(\xi)}{\partial \xi}^T d\xi \tag{2.33b}$$

$$\mathbf{K}_{\gamma 22} = \frac{2}{L} k_s GA \int_{-1}^{1} \frac{\partial \mathbf{f}(\xi)}{\partial \xi} \frac{\partial \mathbf{f}(\xi)}{\partial \xi}^T d\xi \tag{2.33c}$$

$$\mathbf{K}_{\gamma 23} = k_s GA \int_{-1}^{1} \mathbf{g}(\xi) \frac{\partial \mathbf{f}(\xi)}{\partial \xi}^T d\xi \tag{2.33d}$$

$$\mathbf{K}_{\gamma 32} = k_s GA \int_{-1}^{1} \frac{\partial \mathbf{f}(\xi)}{\partial \xi} \mathbf{g}(\xi)^T d\xi \tag{2.33e}$$

$$\mathbf{K}_{\gamma 33} = \frac{L}{2} k_s GA \int_{-1}^{1} \mathbf{g}(\xi) \mathbf{g}(\xi)^T d\xi \tag{2.33f}$$

The non-linear terms of the stiffness matrix are affected by the nonlocal parameter, due to that, the non-linear terms are divided in nonlocal and local.

The local and non-linear stiffness matrix is given by,

$$\mathbf{K}_{nl-local} = \begin{bmatrix} \mathbf{0} & \mathbf{K}_2^1 & \mathbf{0} \\ \mathbf{K}_3^1 & \mathbf{K}_4^2 & \mathbf{0} \\ \mathbf{0} & \mathbf{0} & \mathbf{0} \end{bmatrix} \tag{2.34}$$

$$\mathbf{K}_2^1 = \frac{2}{L^2} EA \int_{-1}^{1} \left(\frac{\partial \mathbf{f}(\xi)}{\partial \xi}^T \mathbf{q}_w(t) \right) \frac{\partial \mathbf{t}(\xi)}{\partial \xi} \frac{\partial \mathbf{f}(\xi)}{\partial \xi}^T d\xi \tag{2.35a}$$

$$\mathbf{K}_3^1 = \frac{4}{L^2} EA \int_{-1}^{1} \left(\frac{\partial \mathbf{f}(\xi)}{\partial \xi}^T \mathbf{q}_w(t) \right) \frac{\partial \mathbf{f}(\xi)}{\partial \xi} \frac{\partial \mathbf{t}(\xi)}{\partial \xi}^T d\xi \tag{2.35b}$$

$$\mathbf{K}_4^2 = \frac{4}{L^3} EA \int_{-1}^{1} \left(\frac{\partial \mathbf{f}(\xi)}{\partial \xi}^T \mathbf{q}_w(t) \right)^2 \frac{\partial \mathbf{f}(\xi)}{\partial \xi} \frac{\partial \mathbf{f}(\xi)}{\partial \xi}^T d\xi \tag{2.35c}$$

where the superscript indicates the order of the non-linearity of the matrix.

The nonlocal and non-linear stiffness matrix can be written as,

$$\mathbf{K}_{nl-n-local} = \begin{bmatrix} \mathbf{0} & \mathbf{0} & \mathbf{0} \\ \mathbf{K}_5^1 & \mathbf{K}_6^2 & \mathbf{0} \\ \mathbf{0} & \mathbf{0} & \mathbf{0} \end{bmatrix} \tag{2.36}$$

$$\mathbf{K}_5^1 = \frac{16}{L^4} EA\mu \int_{-1}^{1} \left(\frac{\partial^2 \mathbf{f}(\xi)}{\partial \xi^2}^T \mathbf{q}_w(t) \right) \frac{\partial^2 \mathbf{f}(\xi)}{\partial \xi^2} \frac{\partial \mathbf{t}(\xi)}{\partial \xi}^T d\xi \tag{2.37a}$$

$$\mathbf{K}_6^2 = \frac{16}{L^5} EA\mu \int_{-1}^{1} \left(\frac{\partial^2 \mathbf{f}(\xi)}{\partial \xi^2}^T \mathbf{q}_w(t) \right)^2 \frac{\partial^2 \mathbf{f}(\xi)}{\partial \xi^2} \frac{\partial^2 \mathbf{f}(\xi)}{\partial \xi^2}^T d\xi \tag{2.37b}$$

Electrostatic Force

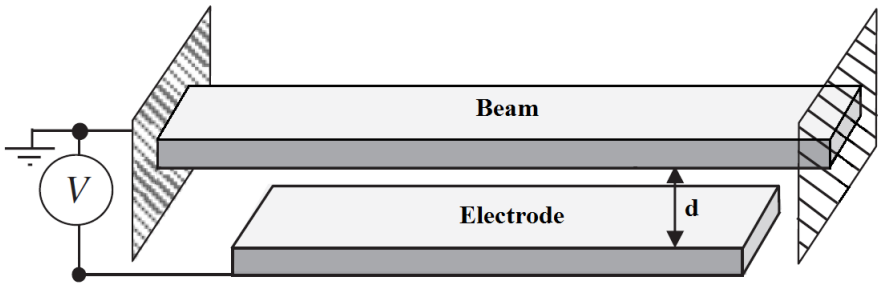

FIGURE 2.2: Schematic layout of a double clamped nanobeam under electrostatic actuation.

The expression that gives the distributed electrostatic force applied in the nanobeam, includes a first order fringing field effect correction [19, 42, 43], and is given by,

$$f_e = -\frac{\varepsilon_0 b V^2}{2(d+w)^2} \left(1 + 0.65\zeta \frac{d+w}{b} \right) \tag{2.38}$$

where ε_0 denotes the permittivity of vacuum, V is the voltage applied, d is the gap between the beam and the electrodes, b represents the width of the beam and ζ is binary auxiliary parameter that takes the value 0 or 1, in case one wants to consider the fringing field effect or not.

The electrostatic force is highly non-linear, and in order to consider it's effect in the p-version model, a Taylor expansion, considering the first five terms of the series, was applied.

$$\begin{aligned} f_e \approx & \frac{\varepsilon_0 b V^2}{2} \left[\frac{1}{d^2} + \frac{0.65\zeta}{bd} - w\left(\frac{2}{d^3} + \frac{0.65\zeta}{bd^2} \right) + w^2 \left(\frac{3}{d^4} + \frac{0.65\zeta}{bd^3} \right) \right. \\ & \left. - w^3 \left(\frac{4}{d^5} + \frac{0.65\zeta}{bd^4} \right) + w^4 \left(\frac{5}{d^6} + \frac{0.65\zeta}{bd^5} \right) \right] \end{aligned} \tag{2.39}$$

In order to know if the number of terms used in the expansion assure a correct approximation of the force and to know the valid domain of the deflection, a convergence study was carried out for three, four and five terms.

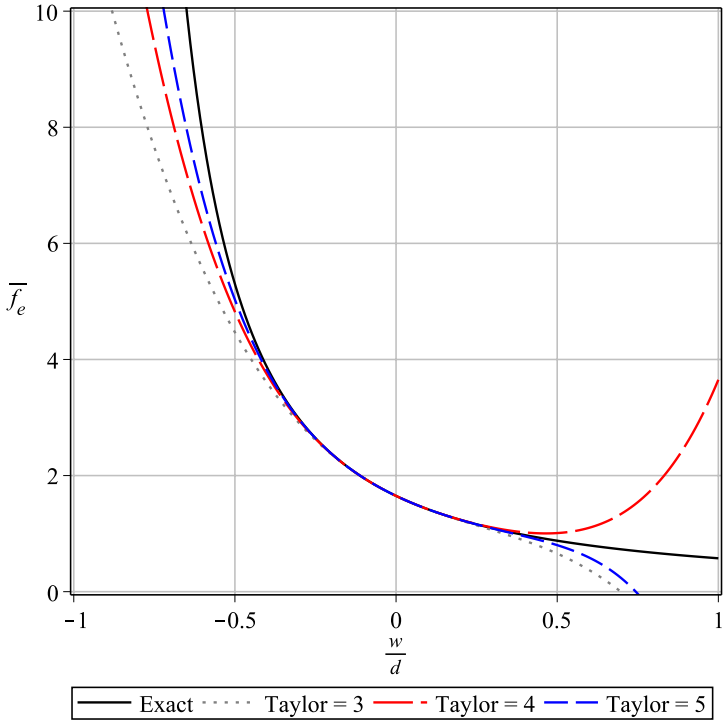

FIGURE 2.3: Convergence of the Taylor expansion series.

Analysing Figure 2.3, where the electrostatic force ($\bar{f}_e$) is presented in a non-dimensional form, the approximation that was carried out is only valid for $|\frac{w}{d}| < 0.5$. In this value range, and using five terms of the expansion, a good approximation for the exact expression of the force is achieved.

In the equation of motion (Eq. 2.25b), the electrostatic force is also affected by the nonlocal parameter, which means that it's necessary to divide the electrostatic terms in local and nonlocal.

Regarding the local terms first, applying the Galerkin method to all terms of the Taylor expansion and using the relations of Eq. (2.26), one derives the following,

$$\mathbf{v}_{fe} = -\frac{\varepsilon_0 b L V^2}{4}\Big(\frac{1}{d^2} + \frac{0.65\zeta}{bd}\Big)\int_{-1}^{1} \mathbf{f}(\xi)\, d\xi \tag{2.40a}$$

$$\mathbf{K}^0_{fe} = -\frac{\varepsilon_0 b L V^2}{4}\Big(\frac{2}{d^3} + \frac{0.65\zeta}{bd^2}\Big)\int_{-1}^{1} \mathbf{f}(\xi)\, \mathbf{f}(\xi)^T d\xi \tag{2.40b}$$

$$\mathbf{K}^1_{fe} = -\frac{\varepsilon_0 b L V^2}{4}\Big(\frac{3}{d^4} + \frac{0.65\zeta}{bd^3}\Big)\int_{-1}^{1} \mathbf{f}(\xi)\, \mathbf{f}(\xi)^T \Big(\mathbf{f}(\xi)\, \mathbf{q}_w(t)\Big) d\xi \tag{2.40c}$$

$$\mathbf{K}^2_{fe} = -\frac{\varepsilon_0 b L V^2}{4}\Big(\frac{4}{d^5} + \frac{0.65\zeta}{bd^4}\Big)\int_{-1}^{1} \mathbf{f}(\xi)\, \mathbf{f}(\xi)^T \Big(\mathbf{f}(\xi)\, \mathbf{q}_w(t)\Big)^2 d\xi \tag{2.40d}$$

$$\mathbf{K}^3_{fe} = -\frac{\varepsilon_0 b L V^2}{4}\Big(\frac{5}{d^6} + \frac{0.65\zeta}{bd^5}\Big)\int_{-1}^{1} \mathbf{f}(\xi)\, \mathbf{f}(\xi)^T \Big(\mathbf{f}(\xi)\, \mathbf{q}_w(t)\Big)^3 d\xi \tag{2.40e}$$

In order to derive the components that represent the nonlocal effect of the electrostatic force, Galerkin's method was applied directly in the nonlocal component of the force from Eq. (3.25b), before applying the method to the Taylor expansion terms.

$$-\int_0^L \mathbf{f}(x)\, \mu \frac{\partial^2 f_e(x,t)}{\partial x^2} dx \tag{2.41}$$

Integrating by parts, one has,

$$-\mu\int_0^L \mathbf{f}(x)\, \frac{\partial^2 f_e(x,t)}{\partial x^2} dx = -\mu\frac{2}{L}\Big[\underbrace{f(\xi)\frac{\partial f_e}{\partial \xi}\Big|_{-1}^{1}}_{=0} - \int_{-1}^{1} \frac{\partial \mathbf{f}(\xi)}{\partial \xi}\frac{\partial f_e(\xi,t)}{\partial \xi} d\xi\Big] = \mu\frac{2}{L}\int_{-1}^{1} \frac{\partial \mathbf{f}(\xi)}{\partial \xi}\frac{\partial f_e(\xi,t)}{\partial \xi} d\xi \tag{2.42}$$

The first term resulting from integration by parts of Eq. (2.41) is zero due to the boundary conditions considered, which are simply supported and double clamped, where the shape functions considered are zero at the beam ends. Applying Galerkin's method, this time to the Taylor expansion terms of $\frac{\partial f_e}{\partial x}$, the nonlocal terms of the electrostatic force are derived,

$$\mathbf{K}^0_{\mu fe} = \frac{\varepsilon_0 b \mu V^2}{L}\Big(\frac{2}{d^3} + \frac{0.65\zeta}{bd^2}\Big)\int_{-1}^{1} \frac{\partial \mathbf{f}(\xi)}{\partial \xi}\frac{\partial \mathbf{f}(\xi)}{\partial \xi}^T d\xi \tag{2.43a}$$

$$\mathbf{K}^1_{\mu fe} = \frac{\varepsilon_0 b \mu V^2}{L}\Big(\frac{3}{d^4} + \frac{0.65\zeta}{bd^3}\Big)\int_{-1}^{1} \frac{\partial \mathbf{f}(\xi)}{\partial \xi}\frac{\partial \mathbf{f}(\xi)}{\partial \xi}^T \Big(\mathbf{f}(\xi)\, \mathbf{q}_w(t)\Big) d\xi \tag{2.43b}$$

$$\mathbf{K}^2_{\mu fe} = \frac{\varepsilon_0 b \mu V^2}{L}\Big(\frac{4}{d^5} + \frac{0.65\zeta}{bd^4}\Big)\int_{-1}^{1} \frac{\partial \mathbf{f}(\xi)}{\partial \xi}\frac{\partial \mathbf{f}(\xi)}{\partial \xi}^T \Big(\mathbf{f}(\xi)\, \mathbf{q}_w(t)\Big)^2 d\xi \tag{2.43c}$$

$$\mathbf{K}^3_{\mu fe} = \frac{\varepsilon_0 b \mu V^2}{L}\Big(\frac{5}{d^6} + \frac{0.65\zeta}{bd^5}\Big)\int_{-1}^{1} \frac{\partial \mathbf{f}(\xi)}{\partial \xi}\frac{\partial \mathbf{f}(\xi)}{\partial \xi}^T \Big(\mathbf{f}(\xi)\, \mathbf{q}_w(t)\Big)^3 d\xi \tag{2.43d}$$

With all terms defined, it's now possible to write the equations of motion in a matrix form.

$$\begin{bmatrix} \mathbf{0} & \mathbf{0} & \mathbf{0} \\ \mathbf{0} & \mathbf{M}^{w} + \mathbf{M}^{\mu w} & \mathbf{0} \\ \mathbf{0} & \mathbf{0} & \mathbf{M}^{\phi} + \mathbf{M}^{\mu\phi} \end{bmatrix} \begin{Bmatrix} \ddot{\mathbf{q}}_u(t) \\ \ddot{\mathbf{q}}_w(t) \\ \ddot{\mathbf{q}}_\phi(t) \end{Bmatrix} + \left(\begin{bmatrix} \mathbf{K}_p & \mathbf{0} & \mathbf{0} \\ \mathbf{0} & \mathbf{K}_{\gamma 22} & \mathbf{K}_{\gamma 23} \\ \mathbf{0} & \mathbf{K}_{\gamma 32} & \mathbf{K}_{\gamma 33} + \mathbf{K}_b \end{bmatrix} + \begin{bmatrix} \mathbf{0} & \mathbf{K}_2^1 & \mathbf{0} \\ \mathbf{K}_3^1 + \mathbf{K}_5^1 & \mathbf{K}_4^2 + \mathbf{K}_6^2 & \mathbf{0} \\ \mathbf{0} & \mathbf{0} & \mathbf{0} \end{bmatrix} \right) \begin{Bmatrix} \mathbf{q}_u(t) \\ \mathbf{q}_w(t) \\ \mathbf{q}_\phi(t) \end{Bmatrix} = \begin{Bmatrix} \mathbf{0} \\ \mathbf{f_e} \\ \mathbf{0} \end{Bmatrix} \tag{2.44}$$

where $\mathbf{f_e}$ contains all the terms defined in Eqs. (2.40) and (2.43).

From the first equation of motion (longitudinal direction) one can derive an expression to relate $\mathbf{q}_u$ and $\mathbf{q}_w$, which is the following,

$$\mathbf{q}_u(t) = -(\mathbf{K}_p^{-1}\mathbf{K}_2^1)\mathbf{q}_w(t) \tag{2.45}$$

This way, one can consider only two equations of motion that are coupled and depend only on $\mathbf{q}_w$ and $\mathbf{q}_\phi$.

$$\begin{aligned} &[\mathbf{M}^{w} + \mathbf{M}^{\mu w}]\ddot{\mathbf{q}}_w(t) + \mathbf{K}_{\gamma 23}\mathbf{q}_\phi(t) + [\mathbf{K}_{\gamma 22} + \mathbf{K}_{fe}^0 + \mathbf{K}_{\mu fe}^0]\mathbf{q}_w(t) - \left([\mathbf{K}_3^1 + \mathbf{K}_5^1][\mathbf{K}_p^{-1}\mathbf{K}_2^1]\right)\mathbf{q}_w(t) \\ &+ \left(\mathbf{K}_4^2 + \mathbf{K}_6^2 + \mathbf{K}_{fe}^1 + \mathbf{K}_{fe}^2 + \mathbf{K}_{fe}^3 + \mathbf{K}_{\mu fe}^1 + \mathbf{K}_{\mu fe}^2 + \mathbf{K}_{\mu fe}^3\right)\mathbf{q}_w(t) + \mathbf{v}_{fe} = \mathbf{0} \end{aligned} \tag{2.46}$$

$$[\mathbf{M}^{\phi} + \mathbf{M}^{\mu\phi}]\ddot{\mathbf{q}}_\phi(t) + \mathbf{K}_{\gamma 32}\mathbf{q}_w(t) + [\mathbf{K}_{\gamma 33} + \mathbf{K}_b]\mathbf{q}_\phi(t) = \mathbf{0} \tag{2.47}$$

Grouping all linear stiffness terms and a doing the same for the non-linear stiffness terms, one can rewrite the previous equations as follows,

$$\mathbf{M}_{lw}\ddot{\mathbf{q}}_w(t) + \mathbf{KL}_\phi^1\mathbf{q}_\phi(t) + \Big(\underbrace{\mathbf{KL}_w^1 + \mathbf{KNL}(q_w(t))}_{\mathbf{K}_w}\Big)\mathbf{q}_w(t) + \mathbf{v}_{fe} = \mathbf{0} \tag{2.48}$$

$$[\mathbf{M}_{l\phi}]\ddot{\mathbf{q}}_\phi(t) + \mathbf{KL}_\phi^2\mathbf{q}_\phi(t) + \mathbf{KL}_w^2\mathbf{q}_w(t) = \mathbf{0} \tag{2.49}$$

2.4 HARMONIC BALANCE METHOD

There are some methods that can be used to obtain the solutions of non-linear differential equations, such as perturbation methods, time domain integration methods, the harmonic balance method and others [44, 45]. Perturbation methods are only applicable for weakly non-linear systems which restricts their application. Direct time domain integration methods, as Newmark, Wilson-θ or the finite differences, allows the analysis of periodic and non-periodic motions, however, convergence to a steady-state solution has, sometimes, proven to be difficult [45].

In this dissertation the harmonic balance method (HBM) was used, and it solves the non-linear equations of motion in the frequency domain. In this method, the solution is written in the form of a truncated Fourier series with a finite number of harmonics. The coefficients of the harmonics are then compared, and non-linear algebraic equations in the space and frequency variables are derived.

In non-linear vibrations, the oscillations with amplitudes of the order of the structures' thickness tend to be periodic, as proven by experimental time domain analysis, numerical and analytical investigations, which supports the applicability of the HBM in the study of non-linear dynamics [22,28–30]. The advantages and disadvantages of the HBM are presented next.

Advantages of the HBM

— Applicable to both weakly and highly non-linear systems;

— As the number of harmonics considered increase, the solution converges to the exact periodic one;

— Differential equations are reduced to algebraic ones;

— Easy to implement numerically and results are obtained with a small computational cost.

Disadvantages of the HBM

— The number of non-linear equations to solve increase with the number of harmonics used, becoming complex when several ones are considered;

— Appropriate harmonics in the Fourier series must be considered in order to avoid considerable errors;

— The method is only directly applicable to periodic motions.

Solution of the equations of motion

Since only periodic solutions of the equations of motion are of interest, the generalized solutions can be written in a Fourier series,

$$\mathbf{q}_w(t) = \frac{\mathbf{u}_0}{2} + \sum_{i=1}^{3}(\mathbf{u}_i \cos(i\omega t)) \tag{2.50a}$$

$$\mathbf{q}_\phi(t) = \frac{\mathbf{u}_4}{2} + \sum_{i=5}^{7}(\mathbf{u}_i \cos((i-4)\omega t)) \tag{2.50b}$$

where the vectors $\mathbf{u}_i$ are the coefficients of the harmonics. One constant term and three harmonics are considered for the periodic solution so the model can accurately represent the periodic oscillations, and also detect typical non-linear phenomena such as internal resonances and bifurcation points, which will be studied later on in this dissertation. The equations of motion contain odd and even polynomial type of non-linear terms, and since no type of damping was considered, only the cosine terms of the Fourier expansion are necessary.

Differentiating $\mathbf{q}_w$ and $\mathbf{q}_\phi$ twice in order to t, and inserting $\mathbf{q}_w$, $\mathbf{q}_\phi$, $\ddot{\mathbf{q}}_w$, $\ddot{\mathbf{q}}_w$ in Eqs. (2.46) and (2.47) one arrives to non-differential equations of the form,

$$\mathbf{F}(\mathbf{u}_0, \mathbf{u}_1, \mathbf{u}_2, \mathbf{u}_3, \mathbf{u}_4, \mathbf{u}_5, \mathbf{u}_6, \mathbf{u}_7, \omega, t) = \mathbf{0} \tag{2.51}$$

In order to eliminate the cosine terms and the time dependency of the equations, by taking advantage of the orthogonality of the trigonometric functions, the equations are multiplied by each cosine term and then integrated over one period of vibration T.

$$\frac{2}{T}\int_0^T \mathbf{F}(\mathbf{u}_0, \mathbf{u}_1, \mathbf{u}_2, \mathbf{u}_3, \mathbf{u}_4, \mathbf{u}_5, \mathbf{u}_6, \mathbf{u}_7, \omega, t)\cos(i\omega t)dt, \quad i = 0, 1, 2, 3 \tag{2.52}$$

After applying the HBM, a system of non-linear algebraic equations is obtained, and is given by

$$(-\omega^2\mathbf{M}_{HBM} + \mathbf{K}_{HBM})\mathbf{u}_{HBM} + \mathbf{f}_{HBM} = \mathbf{f}_{el} \tag{2.53}$$

were the matrix $\mathbf{M}_{HMB}$ and $\mathbf{K}_{HBM}$ are given by,

$$\mathbf{M}_{HBM} = \begin{bmatrix} \mathbf{0} & \mathbf{0} & \mathbf{0} & \mathbf{0} & \mathbf{0} & \mathbf{0} & \mathbf{0} & \mathbf{0} \\ \mathbf{0} & \mathbf{M}_{lw} & \mathbf{0} & \mathbf{0} & \mathbf{0} & \mathbf{0} & \mathbf{0} & \mathbf{0} \\ \mathbf{0} & \mathbf{0} & 4\mathbf{M}_{lw} & \mathbf{0} & \mathbf{0} & \mathbf{0} & \mathbf{0} & \mathbf{0} \\ \mathbf{0} & \mathbf{0} & \mathbf{0} & 9\mathbf{M}_{lw} & \mathbf{0} & \mathbf{0} & \mathbf{0} & \mathbf{0} \\ \mathbf{0} & \mathbf{0} & \mathbf{0} & \mathbf{0} & \mathbf{0} & \mathbf{0} & \mathbf{0} & \mathbf{0} \\ \mathbf{0} & \mathbf{0} & \mathbf{0} & \mathbf{0} & \mathbf{0} & \mathbf{M}_{l\phi} & \mathbf{0} & \mathbf{0} \\ \mathbf{0} & \mathbf{0} & \mathbf{0} & \mathbf{0} & \mathbf{0} & \mathbf{0} & 4\mathbf{M}_{l\phi} & \mathbf{0} \\ \mathbf{0} & \mathbf{0} & \mathbf{0} & \mathbf{0} & \mathbf{0} & \mathbf{0} & \mathbf{0} & 9\mathbf{M}_{l\phi} \end{bmatrix} \tag{2.54a}$$

$$\mathbf{K}_{HBM} = \begin{bmatrix} \mathbf{K}_w & \mathbf{0} & \mathbf{0} & \mathbf{0} & \mathbf{KL}_\phi^1 & \mathbf{0} & \mathbf{0} & \mathbf{0} \\ \mathbf{0} & \mathbf{K}_w & \mathbf{0} & \mathbf{0} & \mathbf{0} & \mathbf{KL}_\phi^1 & \mathbf{0} & \mathbf{0} \\ \mathbf{0} & \mathbf{0} & \mathbf{K}_w & \mathbf{0} & \mathbf{0} & \mathbf{0} & \mathbf{KL}_\phi^1 & \mathbf{0} \\ \mathbf{0} & \mathbf{0} & \mathbf{0} & \mathbf{K}_w & \mathbf{0} & \mathbf{0} & \mathbf{0} & \mathbf{KL}_\phi^1 \\ \mathbf{KL}_w^2 & \mathbf{0} & \mathbf{0} & \mathbf{0} & \mathbf{KL}_\phi^2 & \mathbf{0} & \mathbf{0} & \mathbf{0} \\ \mathbf{0} & \mathbf{KL}_w^2 & \mathbf{0} & \mathbf{0} & \mathbf{0} & \mathbf{KL}_\phi^2 & \mathbf{0} & \mathbf{0} \\ \mathbf{0} & \mathbf{0} & \mathbf{KL}_w^2 & \mathbf{0} & \mathbf{0} & \mathbf{0} & \mathbf{KL}_\phi^2 & \mathbf{0} \\ \mathbf{0} & \mathbf{0} & \mathbf{0} & \mathbf{KL}_w^2 & \mathbf{0} & \mathbf{0} & \mathbf{0} & \mathbf{KL}_\phi^2 \end{bmatrix} \tag{2.54b}$$

and the vectors $\mathbf{f}_{HBM}$, and $\mathbf{f}_{el}$ are given by,

$$\mathbf{f}_{HBM} = \begin{Bmatrix} \mathbf{F}_{0,HBM}(\omega, u_{0,1,2,3}) \\ \mathbf{F}_{1,HBM}(\omega, u_{0,1,2,3}) \\ \mathbf{F}_{2,HBM}(\omega, u_{0,1,2,3}) \\ \mathbf{F}_{3,HBM}(\omega, u_{0,1,2,3}) \\ \mathbf{0} \\ \mathbf{0} \\ \mathbf{0} \\ \mathbf{0} \end{Bmatrix} \tag{2.55a}$$

$$\mathbf{f}_{el} = \begin{Bmatrix} -\mathbf{v}_{fe} \\ \mathbf{0} \\ \mathbf{0} \\ \mathbf{0} \\ \mathbf{0} \\ \mathbf{0} \\ \mathbf{0} \\ \mathbf{0} \end{Bmatrix} \tag{2.55b}$$

The vectors $\mathbf{F}_{i,HBM}$, presented in Eq. (2.55a), are given by,

$$\mathbf{F}_{i,HBM}(\omega, \mathbf{u}_{0,1,2,3}) = \frac{2}{T}\int_0^T \mathbf{K}_{nl}\mathbf{q}_w(\cos(i\omega t))dt, \quad i = 1,2,3 \tag{2.56}$$

The vector $\mathbf{F}_{0,HBM}$ is calculated by Eq. (2.56), but divided by 2. Matrix $\mathbf{K}_{nl}$ contains all non-linear terms of Eq. (2.46). The matrix $\mathbf{K}_{nl}$ can be separated according to the order of the non-linearity of its terms. There are terms which depend linearly, quadratically and cubically on the solution $\mathbf{u}_{HB}$.

The equations of motion in the frequency domain are given by,

$$\Big(-\omega^2\mathbf{M} + \mathbf{K}_l + \mathbf{K}_{nl}(\boldsymbol{w})\Big)\boldsymbol{w} = \mathbf{0} \tag{2.57}$$

and can be rewritten as

$$\mathbf{f}_r(\boldsymbol{w}, \omega^2) = \mathbf{0} \tag{2.58}$$

2.5 Newton's Method

One can consider a vibration as an oscillatory motion about an equilibrium position. Under a DC electrostatic force, a beam is submitted to an initial deflection that represents the new equilibrium position. This initial deflection, which will be defined as static deflection, was determined by solving the static equilibrium of the equations of motion. Newton's method was used to calculate the static deflection, however, this method is not able to overcome turning points. Due to this limitation, one can only calculate the stable values of the static deflection, and when the "pull-in" instability starts to develop, the method fails to converge to an accurate solution.

There are two loops to consider, one internal and one external. In the external loop, the process begins by considering a small applied tension increment, ΔV, and then a predictor of the solution is calculated as follows,

$$\boldsymbol{w}_{i+1} = \boldsymbol{w}_{i+1}^{previous} + \delta\boldsymbol{w} \tag{2.59}$$

where in the first increment, the solution $\boldsymbol{w}_{i+1}$ is assumed to be zero.

In the internal loop, the solution is corrected by solving the following equation,

$$\boldsymbol{J}\delta\boldsymbol{w} = -\mathbf{f}_r \tag{2.60}$$

where $\boldsymbol{J}$ is the Jacobian matrix of $\boldsymbol{f}_r$, defined by,

$$\boldsymbol{J} = \frac{\partial \mathbf{f}_r}{\partial \boldsymbol{w}} \tag{2.61}$$

Since a static deflection is being determined, no inertia terms are considered in $\boldsymbol{f}_r$. After calculating the increment $\delta \boldsymbol{w}$ the solution is corrected by Eq. (2.59), and the iterative process is restarted until the relative error between to successive solutions is smaller than a defined error/tolerance.

2.6 Continuation Method

In non-linear dynamics, the backbone curves, which relate the evolution of the natural frequencies with the vibration amplitude, can present turning points or secondary branches, which define regions of multiple solutions. In order to pass these regions, a continuation method will be used to solve the algebraic equations derived previously with the HBM.

The continuation method used was originally proposed by Riks [46] and Crisfield [47], to study the snap-back buckling phenomena. The method is based in the Newton's method and a constraint arc-length equation. Lewandowski [27] used the same method to study free and forced vibration of beams in the non-linear regime, and Ribeiro [48] used it to study the geometrical nonlinear vibrations of beams and plates.

The continuation method presented next has two main loops. The external one, estimates a value of the solution based on the two previous determined/know points of the backbone curve. In the internal loop, the solution is corrected by applying the Newton's method.

External Loop

In this loop a predictor of the solution, $\boldsymbol{w}_{i+1}$, is defined based on the two last know points of the backbone curve, and it's given by,

$$\boldsymbol{w}_{i+1} = \boldsymbol{w}_i + \Delta \boldsymbol{w}_{i+1} \tag{2.62}$$

$$\Delta \boldsymbol{w}_{i+1} = (\boldsymbol{w}_i - \boldsymbol{w}_{i-1}) \frac{dw_{aux}}{\Delta w} \tag{2.63}$$

where dw_{aux} is the amplitude of the vector $\Delta \boldsymbol{w}_{i+1}$, and Δw is the amplitude of the vector $\boldsymbol{w}_i - \boldsymbol{w}_{i-1}$.

It's also necessary to define a predictor and the correspondent frequency value, ω^2_{i+1}, which is given by,

$$\omega_{i+1}^2 = \omega_i^2 + \Delta\omega_0^2 \tag{2.64}$$

$$\Delta\omega_0^2 = \pm \frac{s}{\sqrt{\delta \boldsymbol{w}_1^T \delta \boldsymbol{w}_1}} \omega_i^2 \tag{2.65}$$

where s is the arc-length parameter, which represents the distance between the two successive points of the backbone curve and will be defined ahead as well as $\{\delta w\}_1$. The sign in the frequency variation $\Delta\omega_0^2$ (Eq. 2.65), is chosen following the one of the previous increment, in case the sign of the Jacobian matrix remains the same. If the sign changes, the same operation should be carried out in the calculation of $\Delta\omega_0^2$. To define $\{\delta w\}_1$ the last know frequency of the backbone curve should be used.

In the beginning of the method, since the beam starts vibrating from a deflected position, the initial solution for the transverse displacement $\boldsymbol{w}_{i+1}$ will be the static solution derived with Newton's method. The initial frequency predictor will be the linear natural frequency of the mode one intends to study.

Internal Loop

After the predictions of both the amplitude and the frequency are defined, the values must be corrected. In order to do so, the Newton's method is applied to Eq. (2.57), and one arrives at,

$$\mathbf{J}\delta \boldsymbol{w} - \mathbf{M}\boldsymbol{w}_{i+1}\delta\omega^2 = -\mathbf{f}_r \tag{2.66}$$

What allows this method to overcome turning points in the backbone curves, is the fact that despite considering variations in the generalized displacements, variations in the frequency are also taken in to account. Adding to the previous, a correct arc-length parameter adjustment is required in order to constrain the solution and to assure its correct convergence.

$$s^2 = \|\Delta \boldsymbol{w}_{i+1}\|^2 \tag{2.67}$$

From equation Eq. (2.66),

$$\delta \boldsymbol{w} = \delta\omega^2 \delta \boldsymbol{w}_1 + \delta \boldsymbol{w}_2 \tag{2.68}$$

where $\delta \boldsymbol{w}_1$ and $\delta \boldsymbol{w}_2$ result from the following equations,

$$\mathbf{J}\delta \boldsymbol{w}_1 = \mathbf{M}\boldsymbol{w}_{i+1} \tag{2.69}$$

$$\mathbf{J}\delta\boldsymbol{w}_2 = -\mathbf{f}_r \tag{2.70}$$

To correct the value of $\boldsymbol{w}$ one just needs to apply the next equation,

$$\boldsymbol{w}_{i+1} = \boldsymbol{w}_i + \Delta\boldsymbol{w}_{i+1} \tag{2.71}$$

with,

$$\Delta\boldsymbol{w}_{i+1} = \Delta\boldsymbol{w}_{i+1}^{previous} + \delta\boldsymbol{w} \tag{2.72}$$

By substituting $\Delta\boldsymbol{w}_{i+1}$ from Eq. (2.72) into the constraint Eq. (2.67), the following relation for $\delta\omega^2$ is derived,

$$a_1(\delta\omega^2)^2 + a_2\delta\omega^2 + a_3 = 0 \tag{2.73}$$

where,

$$a_1 = \delta\boldsymbol{w}_1^T\delta\boldsymbol{w}_1 \tag{2.74a}$$

$$a_2 = \left(\Delta\delta\boldsymbol{w}_{i+1}^{previous} + \delta\boldsymbol{w}_2\right)^T\delta\boldsymbol{w}_1 \tag{2.74b}$$

$$a_3 = \left(\Delta\delta\boldsymbol{w}_{i+1}^{previous} + \delta\boldsymbol{w}_2\right)^T\left(\Delta\delta\boldsymbol{w}_{i+1}^{previous} + \delta\boldsymbol{w}_2\right) - s^2 \tag{2.74c}$$

To solve Eq. (2.73) one just needs to apply the quadratic equation formula, which results in to different solutions for $\delta\omega^2$. In order to choose the correct solution instead of the one that would lead to an already known point, the angle between the incremental amplitude vector of the previous iteration and the one of the current iteration must be positive. If both angles turn out to be positive, then the appropriate root is the one closer to the linear solution of Eq. (2.73).

To correct the natural frequency, the following equation should be applied,

$$\Delta\omega_{i+1}^2 = (\Delta\omega_{i+1}^2)^{previous} + \delta\omega^2 \tag{2.75}$$

$$\omega_{i+1}^2 = \omega_i^2 + \Delta\omega_{i+1}^2 \tag{2.76}$$

The internal loop is repeated until the following conditions are respected,

$$\left|\frac{\delta\omega^2}{\omega_{i+1}^2}\right| < Error_1 \tag{2.77a}$$

$$\left|\frac{\|\boldsymbol{w}\|}{\|\boldsymbol{w}_{i+1}\|}\right| < Error_2 \tag{2.77b}$$

$$\|\mathbf{f}_r\| < Error_3 \tag{2.77c}$$

If Eq. (2.73) presents complex solutions, or if the method needs a high number of iterations to converge, the arc-length parameter and dw_{aux} must be reduced and the process restarts from Eq. (2.62).

2.6.1 BIFURCATION POINTS AND BRANCH SWITCHING

When analysing the backbone curve of a non-linear dynamical system, one can find regions with multiple solutions, due to bifurcations that may occur. When a bifurcation point is detected in the main branch of the backbone curve, a secondary branch can be originated, however, not all bifurcation points lead to secondary branches. Turning points are also considered bifurcation points and do not lead to secondary branches, and one can characterize a turning point by having two solutions in the neighbour region at one side, and no solution at the other. The designation main branch, indicates a branch which contains a linear solution, or in other words, it contains a solution corresponding to an infinitesimal vibration amplitude which occurs at the linear natural frequency or at a submultiple of a linear natural frequency. A secondary branch corresponds to the one that bifurcates from a main branch.

The detection of bifurcation points is based on analysing the sign of the determinant of $\mathbf{J}$. If the signs of $|\mathbf{J}|$ of two successive points on the backbone curve are different, then somewhere between those two points, a bifurcation point can be found for which $\mathbf{J}$ is singular, i.e $|\mathbf{J}| = 0$.

The continuation method, as described in Section 2.6, is capable of overcoming turning points, however, in order to obtain secondary branches born from a bifurcation point, and additional routine has to be considered. It starts by determining a point sufficiently close to the bifurcation point, which is used as the initial prediction, and the continuation method can then be applied [27, 48]. This initial point is used to calculate the Jacobian matrix and the eigenvalue problem can then be solved. The number of null eigenvalues determines the number of possible branches that can be born from the bifurcation point. Often there is just one null eigenvalue, and in this case the eigenvector associated to the null eigenvalue is used to perturb the solution, by adding the eigenvector to the solution prediction $\boldsymbol{w}$, at the bifurcation point.

$$\boldsymbol{w}_j = \boldsymbol{w} + \varsigma_j \frac{\boldsymbol{\phi}_j}{||\boldsymbol{\phi}_i||} \tag{2.78}$$

In Eq. (2.78), the vector $\boldsymbol{w}_j$ represents the perturbed configuration used as the starting vector to derive the secondary branches and $\boldsymbol{\phi}_j$ represents the eigenvector that corresponds to the null eigenvalue. The parameter ς_j is a scaling factor, which value is determinant of the success of the branch switching. Lewandowski [27] considered $\varsigma = 100$ and Ribeiro [48] found good results with $\varsigma = 50$, which was used in the present work.

All matrices derived in the aforementioned formulation were calculated with the symbolic manipulator *Maple*. Both the Newton's method and the continuation method were implemented in *Fortran*, due its high-performance computing capabilities.

2.7 Conclusion

In this chapter a *p*-version finite element model based on the Timoshenko's beam theory was presented. Geometrical non-linear and nonlocal effects were considered, as well as an external DC electrostatic force and the differential equations of motion were presented. The harmonic balance method was used to derive the algebraic non-linear equations in the frequency domain. Two different iterative methods of solving the non-linear equations were presented. The Newton's method was used to solve the static equilibrium equations, deriving the solution of the static deflection. With this method, one can only obtain stable results, and can't overcome turning points. The continuation method based in an arc-length parameter, was presented to overcome turning points, to detect bifurcation points and to calculate the system's backbone curves, which will be presented in the following chapters.

CHAPTER 3

MODEL VALIDATION

3.1 INTRODUCTION

In this chapter, the different terms of the model are validated by comparing the derived results with published ones. The validation starts for the most simple case, which is the linear analysis and one gradually considers more complex situations where geometric non-linear and nonlocal effects are taken in consideration. After this validation, the terms related to the external DC electrostatic load are also confirmed with published results.

3.2 LINEAR VIBRATION

In order to study the linear free vibration of a nanobeam, a reduced model was used, which considers only the transverse and rotation displacements. The matrix form of the equations of motion for the linear analysis is the following,

$$\begin{bmatrix} \mathbf{M}^{w} + \mathbf{M}^{\mu w} & \mathbf{0} \\ \mathbf{0} & \mathbf{M}^{\phi} + \mathbf{M}^{\mu \phi} \end{bmatrix} \begin{Bmatrix} \ddot{\mathbf{w}} \\ \ddot{\boldsymbol{\phi}} \end{Bmatrix} + \begin{bmatrix} \mathbf{K}_{\gamma 22} & \mathbf{K}_{\gamma 23} \\ \mathbf{K}_{\gamma 32} & \mathbf{K}_{\gamma 33} + \mathbf{K}_{b} \end{bmatrix} \begin{Bmatrix} \mathbf{w} \\ \boldsymbol{\phi} \end{Bmatrix} = \begin{Bmatrix} \mathbf{0} \\ \mathbf{0} \end{Bmatrix} \tag{3.1}$$

3.2.1 CONVERGENCE ANALYSIS

Since the p-version finite element method has its basis in a number n of shape functions, it's important to define the minimum number of shape functions that is necessary for the results to converge.

The convergence analysis was made considering the first natural frequency of a simply supported beam with the properties given in Table 3.1,

TABLE 3.1: Beam properties for the convergence analysis [29].

L [mm]	h [mm]	b [mm]	E [GPa]	ρ [kg/ m^3]	r = $\sqrt{I/A}$ [m]	v
580	2	20	70	2778	8.775×10^{-4}	0.3

where r represents the radius of gyration, and Ω the area of the beam's cross section. In order to have a reference value, 12 shape functions both for the transverse (p_o) and for the rotation (p_t) displacements where used. The difference between the reference value and the others, obtained with less shape functions, were registered in Table 3.2, along with the relative error between them.

TABLE 3.2: Convergence analysis of the 1^{st} natural frequency (rad/s) of a nanobeam.

$p_o = p_t$	ω_1^i	$\lvert\omega_1^{i=11} - \omega_1^i\rvert$	*Relative error (%)*
3	193.3973825	0.661758012	0.343000
4	192.7405692	0.004944785	0.002500
5	192.7400751	0.004450657	0.002310
6	192.7360774	0.000452912	0.000234
7	192.7358400	0.000215529	0.000111
8	192.7358400	0.000214235	0.000104
9	192.7357060	0.000081574	0.000042
10	192.7358387	0.000013266	0.000012
11	192.7356245	0.000008157	0.000004
12	192.7356045	0.000000000	0.000000

Analysing the results, it becomes clear that after using 6 shape functions, the relative error becomes insignificant. However, to achieve the highest precision possible, 12 shape functions for each displacement were used in the following validations of the linear model.

3.2.2 VALIDATION OF THE LINEAR AND NONLOCAL TERMS

In order to validate the linear and the linear nonlocal part of the model developed in this dissertation, a comparison with published results was made. The published results are presented in a non-dimensional form, and the expression used was the following,

$$\Omega = \omega L^2 \sqrt{\frac{\rho A}{EI}} \tag{3.2}$$

The beam considered in this validation is simply supported and has the properties presented in Table 4.3.

TABLE 3.3: Beam properties for the validation of the linear/nonlocal model [9,39].

L	E	v	ρ
10	30×10^6	0.3	1

Presented in Table 3.4 are the values for the first natural frequency of the considered beam, calculated with the model developed, as well as the values obtained by Reddy [9] and Huu-Tai Thai [39]. The values were calculated for different nonlocal parameters and different slenderness ratio L/h of the beam.

TABLE 3.4: Validation of the linear/nonlocal model for a SS beam.

L/h	μ	p-version model	Reddy [9]	Huu-Tai Thai [39]
100	0	9.8679	9.8683	9.8679
	1	9.4143	9.4159	9.4143
	2	9.0179	9.0183	9.0180
	3	8.6678	8.6682	8.6678
	4	8.3555	8.3558	8.3555
20	0	9.8281	9.8381	9.8281
	1	9.3763	9.3858	9.3763
	2	8.9816	8.9907	8.9816
	3	8.6328	8.6416	8.6328
	4	8.3218	8.3302	8.3218
10	0	9.7075	9.7454	9.7075
	1	9.2612	9.2973	9.2612
	2	8.8713	8.9059	8.8714
	3	8.5269	8.5601	8.5269
	4	8.2196	8.2517	8.2197

Analysing the results, is clear that the ones calculated with the developed model are accurate and very similar to the values existing in the literature, with relative differences below 1%.

In Table 3.5, the first three natural frequencies are presented for a double clamped beam with a slenderness ratio of $L/h = 100$, and with the same elastic properties of the beam considered before. The results obtained are in good agreement with the values presented by Eltaher et al. [49], although the author used the Euler-Bernoulli beam theory.

TABLE 3.5: Validation of the linear/nonlocal model for a CC beam.

N.Frequency	μ	*p*-version model	M.A.Eltaher et al. [49]
Ω_1	0	22.3580	22.3744
	1	21.0948	21.1096
	2	20.0194	20.033
	3	19.0902	19.1028
	4	18.2773	18.289
Ω_2	0	61.5755	61.6847
	1	50.9053	50.9844
	2	44.3279	44.392
	3	39.7670	39.822
	4	36.3696	36.4184
Ω_3	0	120.5686	120.9536
	1	85.4878	85.7081
	2	69.9366	70.1033
	3	60.6853	60.8244
	4	54.3798	54.5015

3.2.3 INFLUENCE OF THE NONLOCAL PARAMETER

In order to clearly see the effect of the nonlocal parameter in the natural frequencies for both double clamped and simply supported beams, in Figure 3.1 a frequency ratio was plotted in function of the nonlocal parameter for a beam with a slenderness ratio of $L/h = 100$.

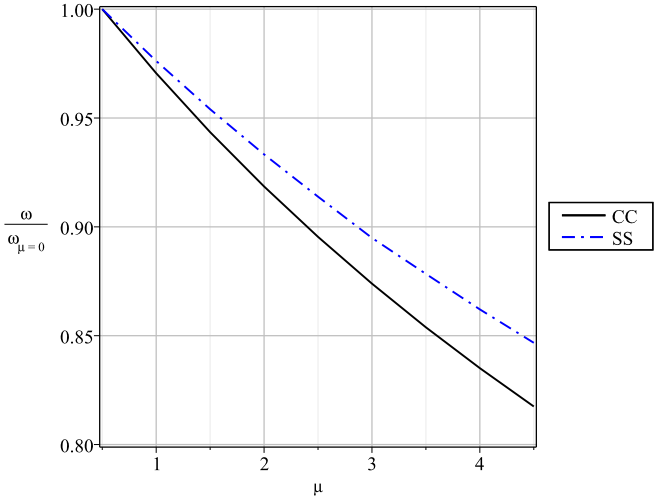

FIGURE 3.1: Effect of the nonlocal parameter on the 1^{st} linear natural frequency.

$$Frequency\ Ratio = \frac{\omega_{non-local}}{\omega_{local}} \tag{3.3}$$

Analysing Figure 3.1, one can see that as the nonlocal parameter increases, the natural frequency decreases for both cases of boundary conditions. However, the double clamped beam is more sensitive to the variation of the nonlocal parameter than the simply supported one.

To see the influence of the nonlocal parameter in the first 3 natural mode shapes of a nanobeam for both type of boundary conditions analysed before, they were plotted in the following figures. In the simply supported case, the nonlocal parameter has no influence in the natural mode shapes, which was also reported by Oliveira [50]. On the other hand, for the double clamped beam, the nonlocal parameter provokes a slight change in the mode shapes. For the first mode this is not so evident, but in the third mode the influence becomes more clear. Just like it was verified for the natural frequencies, the nonlocal parameter has more effect on the natural mode shapes of a double clamped beam than it does in a simply supported one, even though the influence is small.

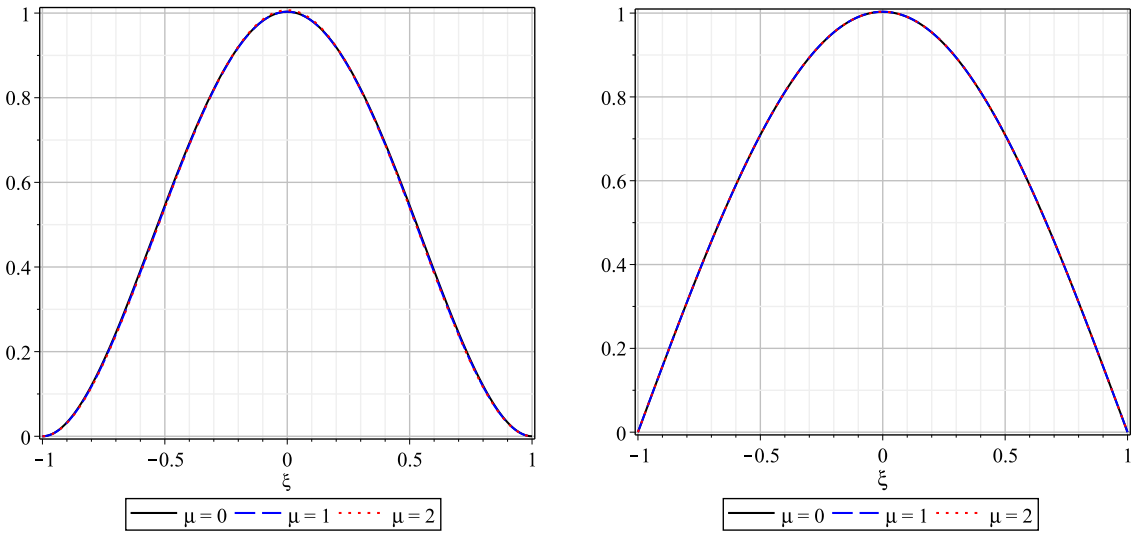

(a) 1^{st} mode - CC

(b) 1^{st} mode - SS

FIGURE 3.2: Effect of the nonlocal parameter on the first linear natural mode shape.

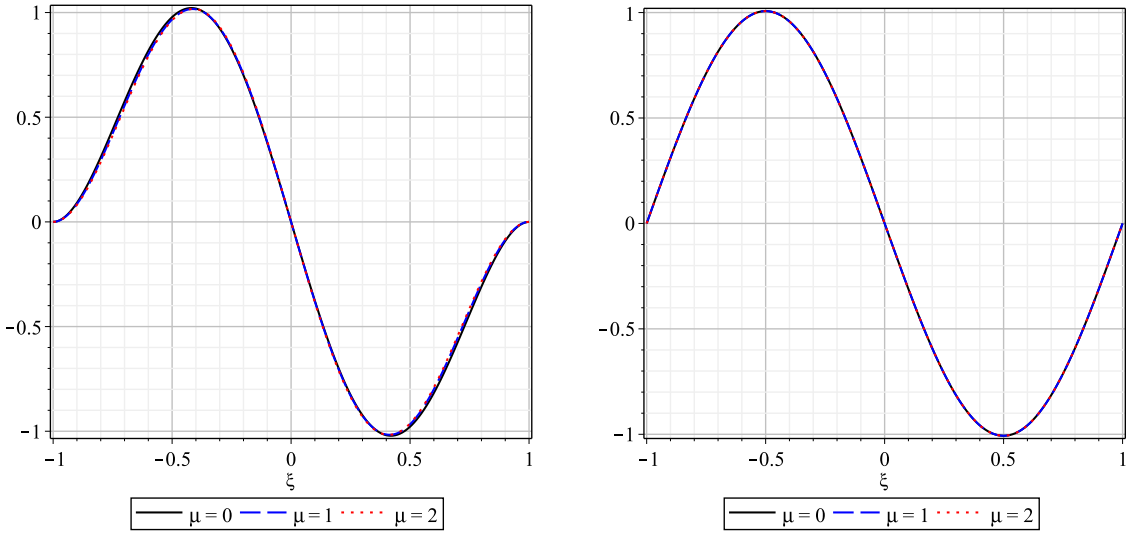

(a) 2^{nd} mode - CC (b) 2^{nd} mode - SS

FIGURE 3.3: Effect of the nonlocal parameter on the second linear natural mode shape.

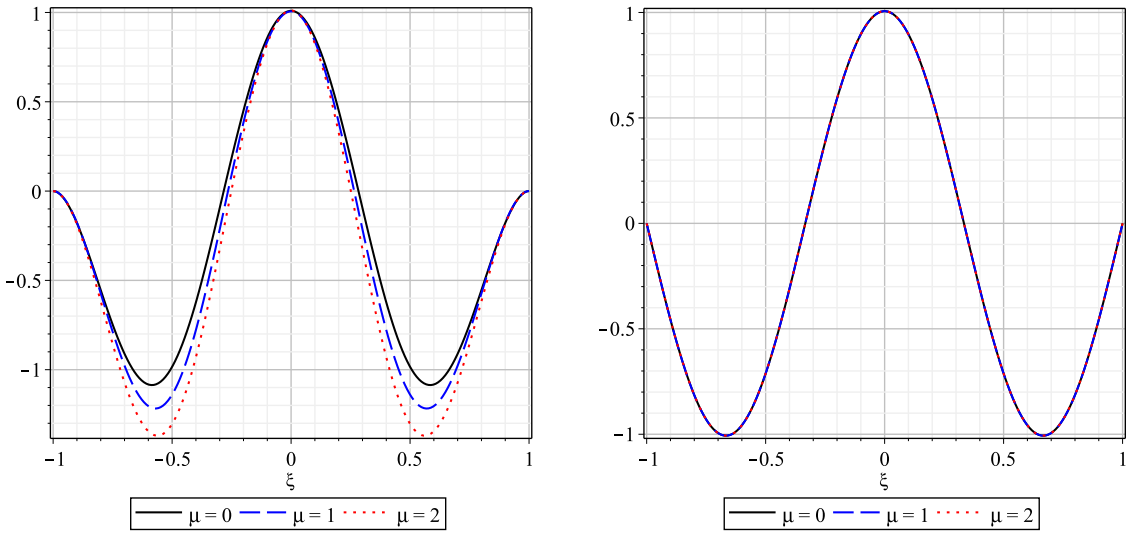

(a) 3^{rd} mode - CC (b) 3^{rd} mode - SS

FIGURE 3.4: Effect of the nonlocal parameter on the third linear natural mode shape.

3.3 NON-LINEAR VIBRATION

3.3.1 VALIDATION OF THE NON-LINEAR AND LOCAL TERMS

The *p*-version of the FEM model will be used to study the non-linear frequencies of an aluminium beam (DTDSO 70) for two boundary conditions, double clamped and simply

supported. The properties of the beam considered for this analysis are presented in Table 3.1. As the response is assumed to be periodic, the first and third harmonic were analysed for all the results presented next.

Boundary Condition: CC

The solution was calculated using $p_o = p_t = 7$ and $p_l = 10$, which were the values that assured an accurate and converged solution. In Figure 3.5, the evolution of the fundamental natural frequency presented by the model, is very close to the one obtained experimentally by White and Bennouna [26]. The amplitude w was calculated at the centre of the beam, and its value was normalized by dividing it by the beams thickness, h.

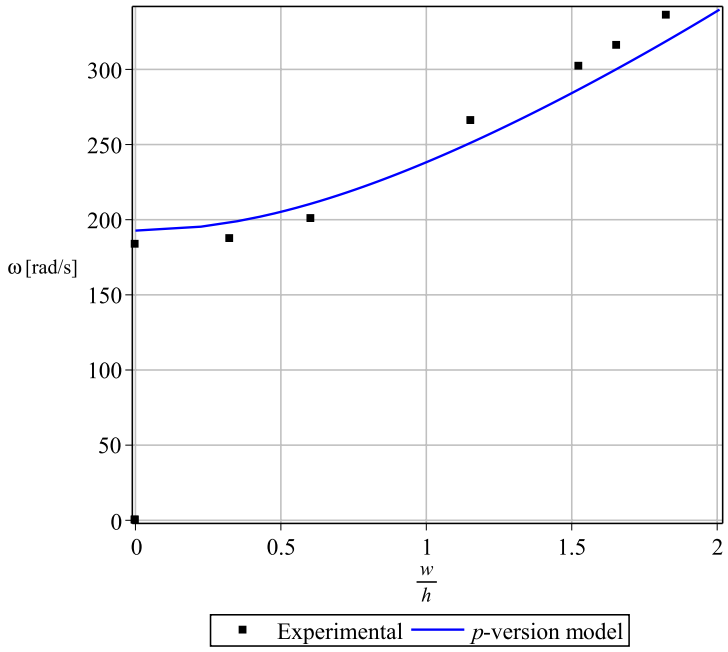

FIGURE 3.5: Comparison of the computed evolution of the first resonant frequency of a CC beam, with experimental results.

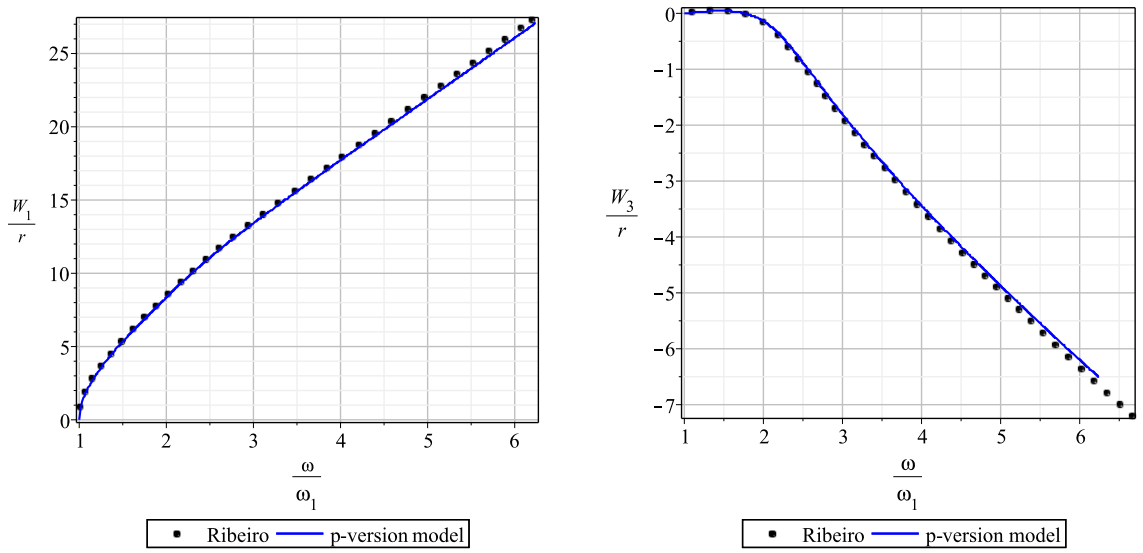

(a) 1^{st} harmonic (b) 3^{rd} harmonic

FIGURE 3.6: Backbone curves of the CC beam, amplitudes W_1 and W_2 calculated at the centre of the beam.

Figure 3.6 shows the backbone curves of the two harmonics used to calculate the solution of the periodic motion, where W_1 and W_3 represent the maximum amplitude of the first and third harmonic respectively, and are in good agreement with the results derived by Ribeiro [29]. When the beam is vibrating in its first non-linear mode shape a hardening spring effect occurs. The reason for this behaviour is that increasing the amplitude of vibration implies increasing the axial stretching due to the large deflection, which leads to a stiffer structure and in turn to a larger non-linear frequency.

TABLE 3.6: Natural frequencies (ω/ω_1) of a CC beam considering one and two harmonics.

w/r	1	4	8	12	16
One harmonic	1.0265	1.3093	1.9481	2.7004	3.6051
Two harmonics	1.0265	1.3059	1.9595	3.1481	4.6369

In Figure 3.7 and in Table 3.6, one can see the importance of the first harmonic in the general response of the system. For low values of amplitude, the system can be accurately modelled with only the first harmonic, however, as the amplitude increases that assumption would lead to significant errors, since the third harmonic has a growing importance in the total vibration of the beam.

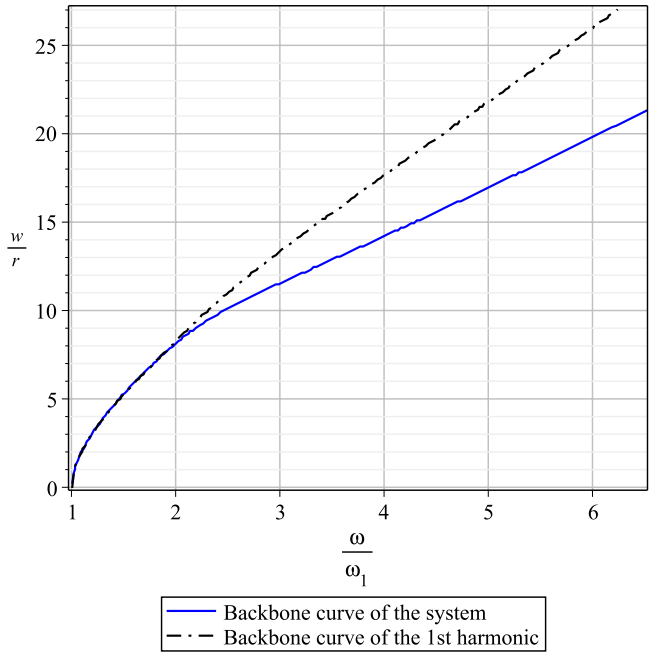

FIGURE 3.7: Backbone curves of a CC beam considering one harmonic and two harmonics.

In Figure 3.8 and 3.9 the first transverse and rotational mode shapes associated with each harmonic are plotted, for different ratios of ω/ω_1.

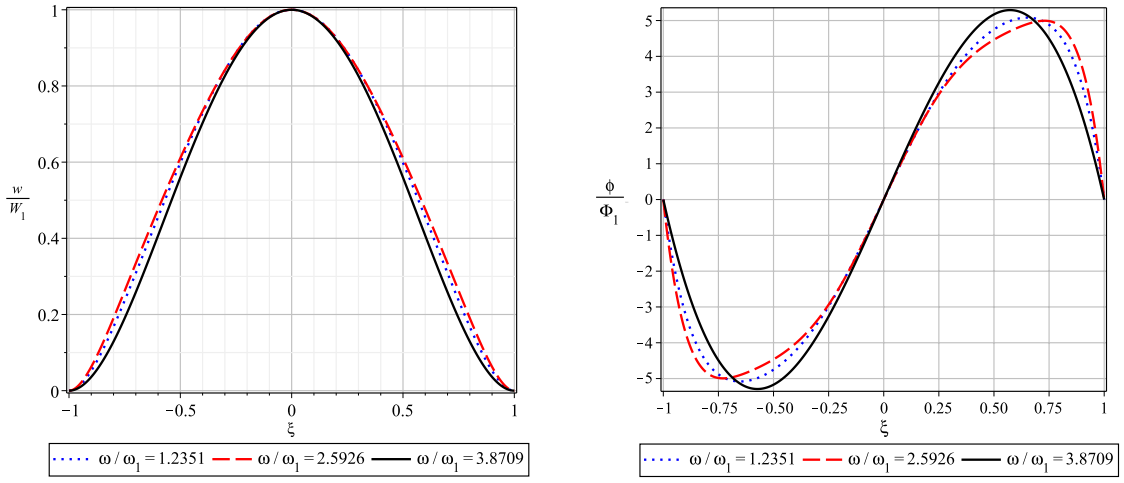

(a) transverse shape (b) rotational shape

FIGURE 3.8: Transverse and rotational shapes of the 1^{st} harmonic for different ratios of ω/ω_1.

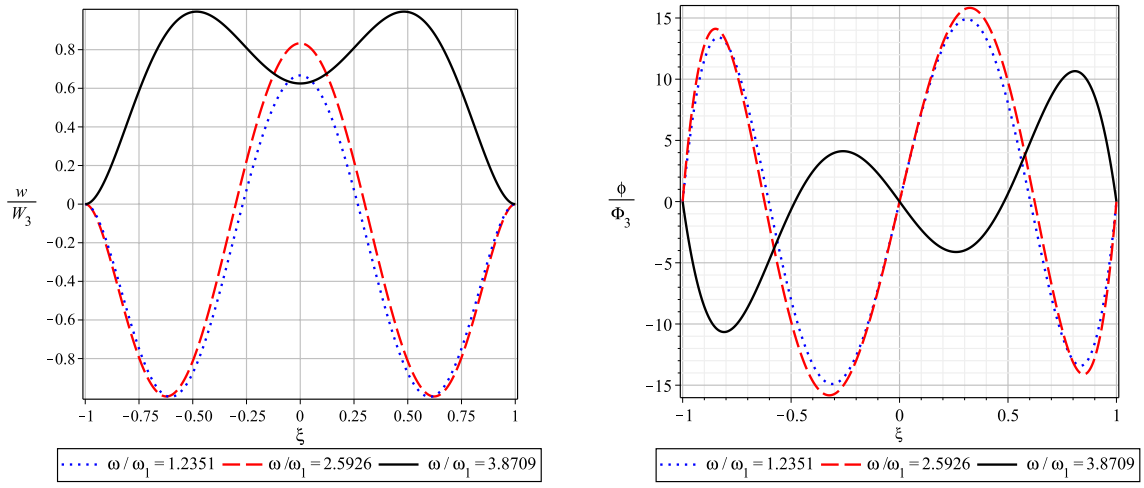

(a) transverse shape (b) rotational shape

FIGURE 3.9: Transverse and rotational shapes of the 3^{rd} harmonic for different ratios of ω/ω_1.

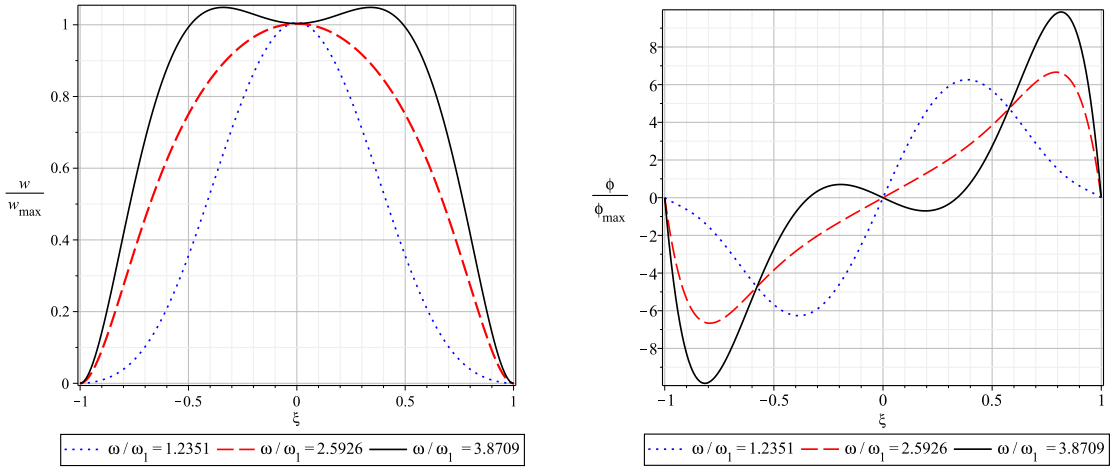

(a) 1^{st}transverse mode shape (b) 1^{st} rotational mode shape

FIGURE 3.10: 1^{st} transverse and rotational mode shape of the CC beam at $t = 2\pi kT$, for different ratios of ω/ω_1.

In Figure 3.10, it's possible to see the shape of the first traverse and rotational mode of the beam for different ratios of ω/ω_1, computed at $t = 2\pi kT$, where k is an integer and T is the period of vibration. In both mode types, for high non-linear frequencies, the shape of the beam is strongly affected by the shape of the third harmonic. When the first harmonic is vibrating at a frequency of $\omega/\omega_1 = 3.8709$, the third harmonic is vibrating at three times that frequency, which is very close to the value of the third linear natural frequency. Due to the commensurability of these two natural frequencies, a 1:3 internal

resonance occurs, where the first and the third mode couple, leading to energy exchanges between them, and consequently the shape of the beam changes significantly during the period of vibration.

Boundary Condition: SS

The same beam was used to calculate the non-linear frequencies, this time for a simply supported boundary condition. The values obtained were compared with the ones presented in the literature [27, 29, 51], in the following tables.

TABLE 3.7: Comparison of ω/ω_{l1} of a SS beam calculated with one and two harmonics.

	p-version model		Lewandowski [27]	
w/r	One harmonic	Two harmonics	One harmonic	Two harmonics
1	1.0872	1.0907	1.0865	1.0906
2	1.3366	1.3108	1.3331	1.3106
3	1.6576	1.6201	1.6422	1.6198

TABLE 3.8: Comparison of ω/ω_{l1} of a SS beam.

w/r	*p*-version model	Kriger (exact) [51]	Lewandowski [27]	Ribeiro [29]
1	1.0907	1.0892	1.0906	1.0894
2	1.3189	1.3108	1.3106	1.3180
3	1.6266	1.6201	1.6198	1.6275

Analysing Table 3.7, the non-linear frequencies ratios calculated with one harmonic are very close to the ones calculated with both harmonics, since in this situation, the third harmonic is less significant than in the double clamped case. The values obtained are very close to the ones presented in the literature.

In Table 3.8 the results were obtained considering the first and the third harmonic for the response. One can see that the results obtained with the developed model are in good agreement with the ones published in the existing literature.

3.3.2 VALIDATION OF THE NON-LINEAR AND NONLOCAL TERMS

The developed model can be applied to any symmetric cross shaped beam. Therefore, the following validation takes into account the effect of the nonlocal parameter on the

non-linear stiffness terms, and a simply supported carbon nanotube is considered. The CNT's properties are presented in Table 3.9,

TABLE 3.9: CNT properties for the validation of the non-linear/nonlocal model [52].

L [nm]	t [nm]	R_{ext}[nm]	E [TPa]	ρ [Kg/ m^3]	ν	k_s	η
6	0.64	1.50	1.10	1300	0.19	0.563	0.033

where the L is the length of CNT, t is the effective tube thickness, R_{ext} is the external radius and $\eta = \frac{e_0 a}{L}$ is the dimensionless nonlocal parameter. The values considered for the shear correction factor k_s, for the Poisson coefficient ν and the Young modulus E were presented by Yang et al. [33] and were calculated using MD simulations. The authors also used the Timoshenko beam theory to study the non-linear free vibration of carbon nanotubes.

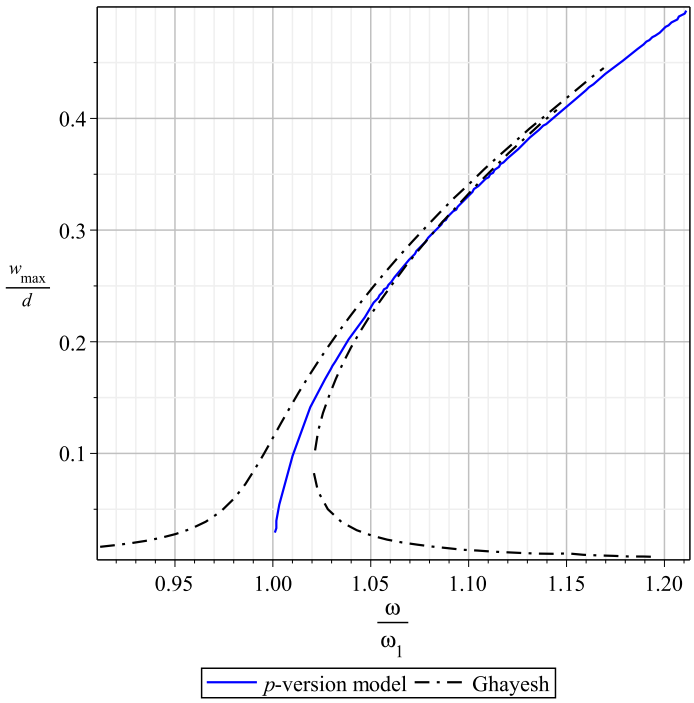

FIGURE 3.11: Frequency response curve of the system: the maximum amplitude of the CNT's midpoint ($x = 0.5L$); the solid and dotted lines represent the stable and unstable solutions, respectively.

In Figure 3.11, the frequency response curve obtained by Ghayesh [52] is presented. The author considered the same CNT presented in Table 3.9 but submitted to a harmonic excitation. The blue line represents the backbone curve obtained by the model with no forces considered, and as expected, in free vibration the response curve is in the middle

of the response curve of the forced regime situation.

Another validation took place, this time for a simply supported beam, where the evolution of the non-linear frequency ratio for different values of the nonlocal parameter is analysed. The beam's geometric properties are presented in the following table.

TABLE 3.10: SS beam properties for the validation of the non-linear/nonlocal model [53].

L [μm]	h [μm]	b [μm]
510	1.5	100

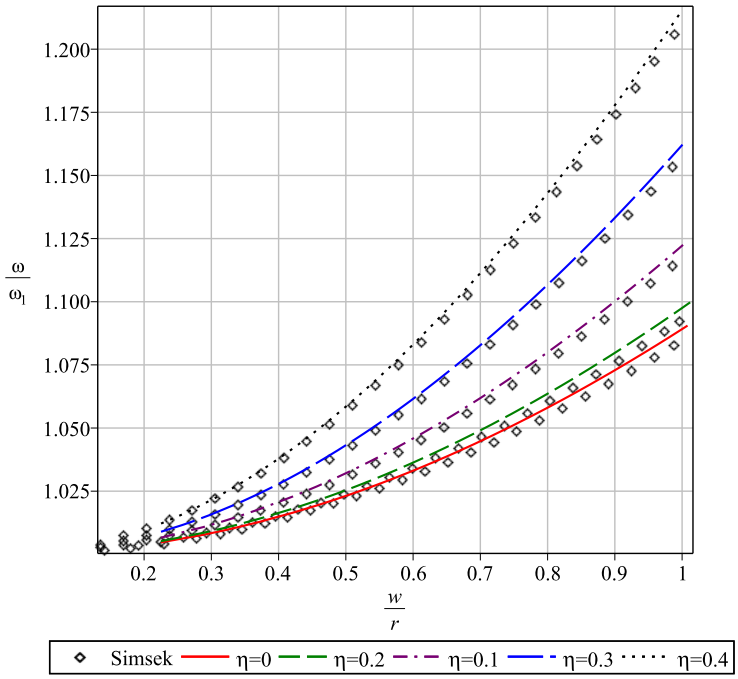

FIGURE 3.12: Variation of the non-linear frequency ratio with the dimensionless amplitude (w/r) for different nonlocal parameter values.

The values derived with the p-version model were compared to ones calculated by Simsek [53]. Figure 3.12 shows the variation of the non-linear frequency ratio with the amplitude of vibration for different values of the dimensionless nonlocal parameter. It's evident that the nonlocal effect increases the non-linear frequency, which increase non-linearly with dimensionless nonlocal parameter and with the vibration amplitude. The nonlocal effects where considered in a non-linear vibration analysis, and accurate results were obtained when compared to published ones.

3.3.3 VALIDATION OF THE ELECTROSTATIC FORCE TERMS

STATIC DEFLECTION AND PULL-IN INSTABILITY

When considering the effect of the electrostatic actuation, it's important to understand the static initial conditions of the problem. When tension is applied, the beam deforms while being attracted to the electrode. This deformation occurs until the internal elastic force of the beam balances the electrostatic one, and an equailibirum state is momently achieved. The deformation of this equilibrium state, can be called the static deformation. It's important to know the static deformation because it's from this point that the natural modes of vibration are going to be studied.

In order to validate the electrostatic force in the model developed, the static deformation of a nanobeam was calculated and compared to published results. The calculation of the static displacement was based on the Newton Method, and due to this, the model can only obtain stable solutions. The beam analysed has the properties presented in Table 3.11.

TABLE 3.11: Properties of the beam for the validation of the non-linear/non-local terms [19].

L [μm]	h [μm]	b [μm]	E [GPa]	ν
300	2	20	169	0.28

The number of shape functions considered in the p-version model was $p_o = p_t = 7$ and $p_l = 10$. In Figure 3.13 the solution was calculated using four and five terms of the Taylor series for the electrostatic force, (Eq. 2.39). The results were compared to the solution obtained by Krylov [19], and in the stable region, the solutions calculated with the model are very close to the ones obtained by the author. The stable region corresponds to the part of the curve where the internal elastic force of the beam can balance the electrostatic force. When the voltage reaches the pull-in voltage, the system becomes unstable and the beam collapses on the actuating electrode, since the internal elastic force is no longer able to balance the forces applied on the beam. In the developed model, the solution for the static deflection was obtained with the Newton method, therefore only stable solutions are obtained. In order to derive the remaining unstable solutions the continuation method could be used, however this method was only used to solve the solutions of the equations of motions in the dynamic regime.

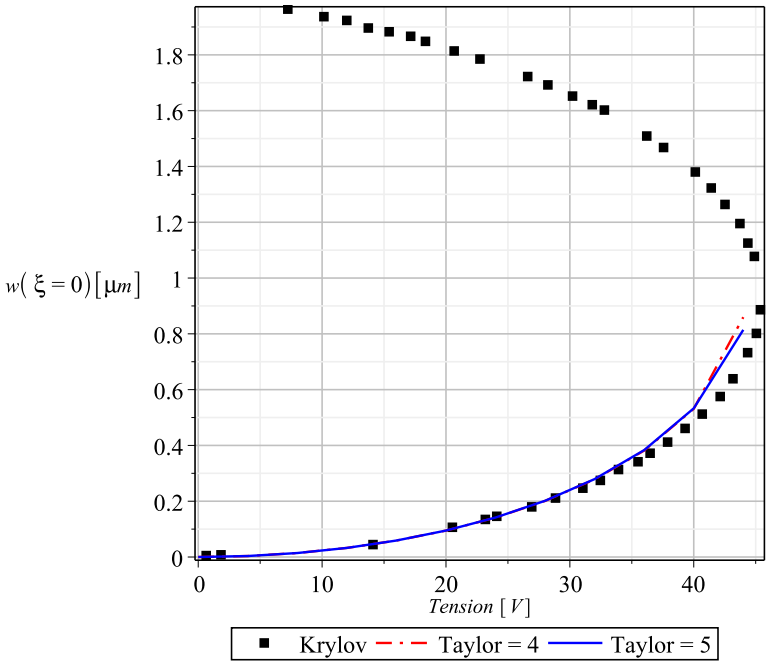

FIGURE 3.13: Deflection of the mid point of a CC beam with the applied tension.

The pull in voltage calculated by Krylov was 45.1 V, and the value calculated with the present model was 44.3 V. The instability of equilibria of electrostatically driven MEMS/NEMS devices, commonly referred to as pull-in instability is encountered as a basic static instability mechanism limiting the operational range of these kind of devices in terms of deflection and voltage. The determination of the pull-in voltage is obtained under the assumption that the increase of the voltage is slow so that no inertia or damping related forces have any type of influence on the structure's behaviour.

3.4 CONCLUSION

In all validation testes, the p-version model developed presented accurate results, which indicates that the model was correctly derived. After proving itself accurate for all the different situations tests in this chapter, the model can know be used to carry out a more detailed dynamical study of a electrostatically actuated nanobeam, which will be presented in Chapter 4.

CHAPTER 4

NUMERICAL RESULTS

4.1 INTRODUCTION

In this chapter, a detailed static and dynamic analysis of an electrostatically actuated nanobeam is presented. The material considered for the nanobeam is an isotropic single crystal silicon, which is a common material used in MEMS and NEMS devices. The influence of the electric tension and the nonlocal parameter is analysed for both static and dynamic analysis. The importance of the constant term and the harmonics considered periodic solution of the HBM in the system's response is studied. The effect of the boundary conditions (CC and SS) in the dynamical behaviour of the nanobeam is examined. The analysis of non-linear phenomena such as internal resonances and bifurcation points are also studied.

4.2 STATIC RESPONSE TO A DC ELECTROSTATIC FORCE

When the natural modes and frequencies, of a beam that is actuated by DC voltage are intend to be studied, knowing its initial deflection is essential to perform a complete dynamic study. The static deformation of the beam corresponds to its initial deflection, where the internal elastic restoring energy balances the electrostatic attraction force. This static deflection is the equilibrium state from which the natural modes of vibration will then be studied.

In order to run a simulation of a real nano dimension beam, one needs to know the properties of the materials used in NEMS devices. Cleland and Roukes [54], reported a process to fabricate double clamped beams from a single-crystal (100) Si substrates with nanometre scale dimensions. NEMS are not limited to Si based devices, graphene sheets,

carbon nanotubes, or other compounds like gallium arsenide (GaAs) can also be used in these small scaled devices [1].

In all following analysis, the material considered was single-crystal (100) silicon. Although this material is anisotropic, in order to simplify the analysis, silicon crystal can be considered isotropic, following the example used in [55]. In Table 4.1 the elastic properties of this material are presented.

TABLE 4.1: Single crystal silicon properties [55].

E [GPa]	ρ [kg/m^3]	ν
150	2330	0.17

The geometric properties of the beam considered in the following analysis is presented in Table 4.2.

TABLE 4.2: Nanobeam properties for the natural frequencies and mode shapes analysis.

L [nm]	h [nm]	b [nm]	d [nm]
40	10	10	40

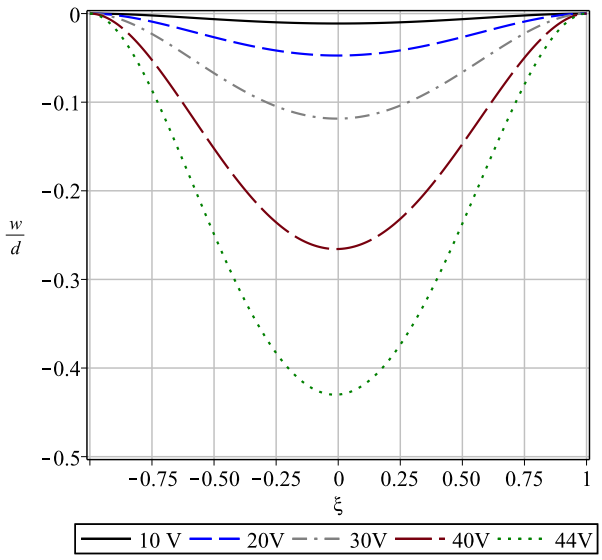

FIGURE 4.1: Static deflection evolution of the mid point of a CC beam for different values of the applied voltage.

In Figure 4.1 the deformation of the beam along the entire domain is plotted for different values of applied voltage. As the voltage reaches higher values, the deflection increases. However, the increase of the static deflection with the applied voltage is not

linear, since higher values of this parameter, lead to increasingly higher deflections, and near the pull-in voltage it is close to the maximum stable value.

4.2.1 NONLOCAL EFFECTS

In order to study the nonlocal effects on the static deformation, one needs to understand the influence of the nonlocal parameter in each term. The nonlocal parameter affects the inertia of the system, the non-linear stiffness and the electrostatic force. Since the static deformation is being analysed, the mass has no influence and only the effects on the non-linear stiffness and on the electrostatic force are going to be studied in this section. Since not much investigation of nonlocal effects on rectangular cross sectioned beams has been done, the range of values for the non-local parameters was chosen in order to clearly see their effect on the analysis made, however the values chosen might not be accurate. The nonlocal parameter enhances the non-linear stiffness terms, and in order to look at this effect independently, the nonlocal terms of the electrostatic force were neglected in this first approach. In Figure 4.2 the static deflection of the CC beam for different values of the dimensionless nonlocal parameter is presented.

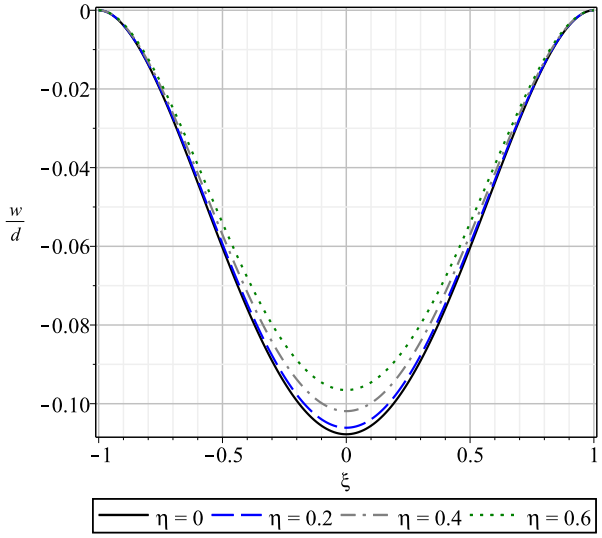

FIGURE 4.2: Static deflection evolution of a CC beam for different values of the dimensionless nonlocal parameter, under a 10 V electrostatic actuation - nonlocal effect on the non-linear stiffness terms.

As the nonlocal parameter increases the non-linear stiffness terms follow the same trend, contributing to the increase of the general stiffness of the beam, that will consequently present a lower deflection. This prediction is in good agreement with Figure 4.2.

In the previous analysis, the nonlocal effect on the electrostatic force was neglected.

This effect will now be considered in both the non-linear stiffness and electrostatic force. Figure 4.2 showed that the increase in the nonlocal parameter lead to a stiffer beam, however, in the electrostatic force, the nonlocal parameter enhances the attraction force, leading to a higher static deflection. Since the effect of the nonlocal parameter leads to opposite outcomes in the static deflection, it is important to know which effect is more significant. In the following figure, the static deflection of the same beam (as the previous analysis) is presented for the same value of voltage and for the same values of the dimensionless nonlocal parameter.

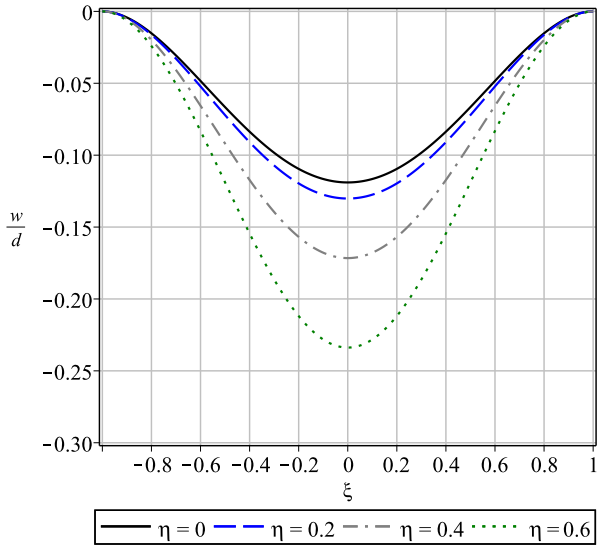

FIGURE 4.3: Static deflection evolution of a CC beam for different values of the dimensionless nonlocal parameter, under a 10 V electrostatic actuation - nonlocal effect on the non-linear stiffness and on the electrostatic force.

Analysing Figure 4.3, oppositely to what is verified in Figure 4.2, the increase of the nonlocal parameter leads to a higher static defection. This way it's possible to understand that the nonlocal effect is more influential in the electrostatic force than it is in the non-linear stiffness. The increase of the electrostatic force overcomes the increase of the non-linear stiffness, thus leading to and overall higher static deflection.

4.3 NATURAL FREQUENCIES AND MODE SHAPES OF A DOUBLE CLAMPED NANOBEAM UNDER A DC ELECTROSTATIC FORCE

The attraction exerted by the electrostatic force to the beam depends not only on the voltage applied but also on the distance between the beam and the electrode, as well as on the width of the beam. The influence of both these geometric parameters in the

resulting attraction force, and consequently on the natural frequencies, is going to the analysed. In order to do so, the mid-plane stretching (geometric non-linearity) is going to be neglected. As the magnitude of the electrostatic force rises the natural frequencies decrease and approach zero as pull-in develops. If the mid-plane stretching had not been neglected, the previous wouldn't always be verified, since the increase of the attraction force leads to an increase in the static deflection of the beam and consequently leads to higher geometric non-linearities that contribute to stiffen the beam and increase the natural frequencies.

In Figures 4.4 and 4.5 the evolution of the natural frequencies with the voltage applied is presented for different values of $\bar{d} = d/h$ and $\beta = b/h$.

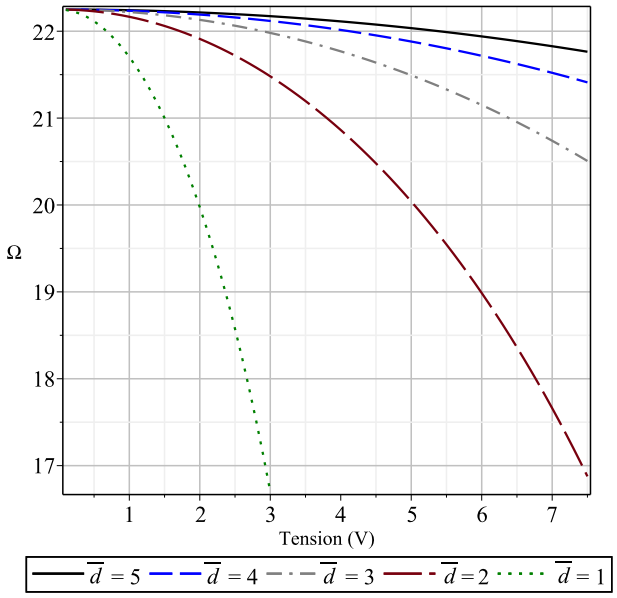

FIGURE 4.4: Variation of the fundamental natural frequency with the voltage applied, for different values of $\bar{d}$.

In both cases, the increase in the applied voltage leads to a decrease in the natural frequencies, however, this decrease is much more sensitive to changes in the gap distance d, than in the beam width b. With this conclusion and analysing the analytical expression of the electrostatic force presented in (Eq 2.38), it's clear that the attraction force is much more dependant on the distance between the beam and the electrode than on the beam's width.

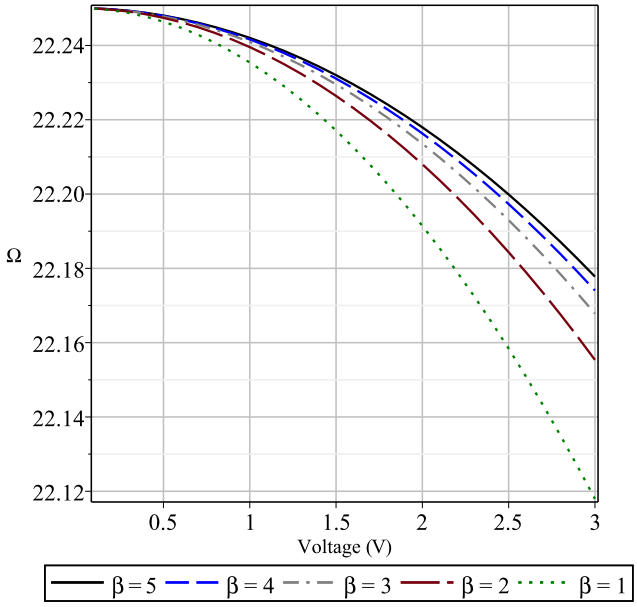

FIGURE 4.5: Variation of the fundamental natural frequency with the tension applied, for different values of β.

In the following analysis, an extensive study of the natural frequencies and mode shapes of a nanobeam under a DC electrostatic force is presented. The nano beam considered is double clamped and has the elastic properties presented in table 4.1, and the geometric properties presented in Table 4.2.

To study the non-linear frequencies, the system's backbone curves are presented for different values of applied voltage V, and dimensionless nonlocal parameter η. The non-linear natural frequencies of vibration are presented in a dimensionless form, given by Eq. (3.2), as well as the transverse displacements, given by $\bar{w} = w/h$, which are always calculated at the centre of the beam and for $t = 0$, unless stated otherwise. Since only cosine terms were considered in the solution of the periodic motions, when $t = 0$, $\bar{w}$ corresponds to the maximum displacement amplitude. For all the following analysis presented in this chapter, the number of shape functions considered to assure accurate results were: $p_o = p_t = 12$ and $p_l = 14$.

Attending to Figures 4.6 - 4.8, its possible to see the loss of symmetry of the backbone curves in relation the the horizontal axis, when the voltage applied is not zero. This loss of symmetry is due to the initial deformed configuration of the beam about which the oscillations occur. In what the natural frequencies are concerned, when the voltage applied is 0 or 5 volts, only hardening spring effect is found, i.e as the amplitude of the oscillations reach higher values, the mid plane stretching effect stiffens the beam, causing the frequencies to increase. The only clear difference in both these situations is the initial offset that exists in the 5 volts case due to the initial beam deflection. As the

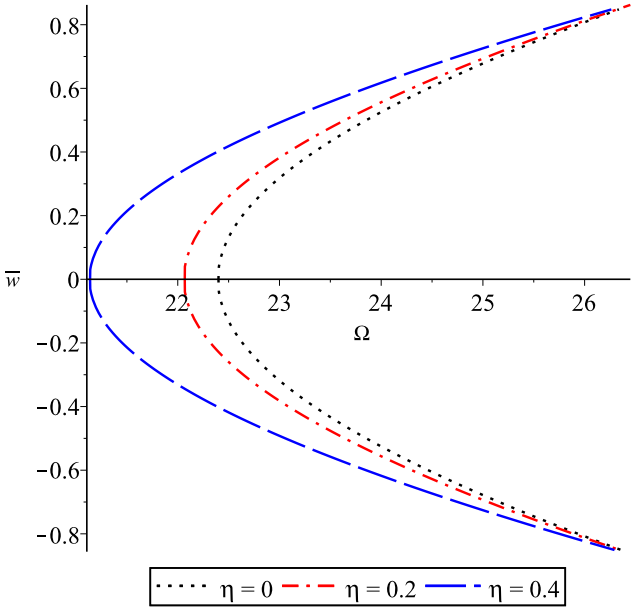

FIGURE 4.6: Total amplitude of vibration of the transverse displacement versus the non-linear natural frequency, when $V = 0$ volt.

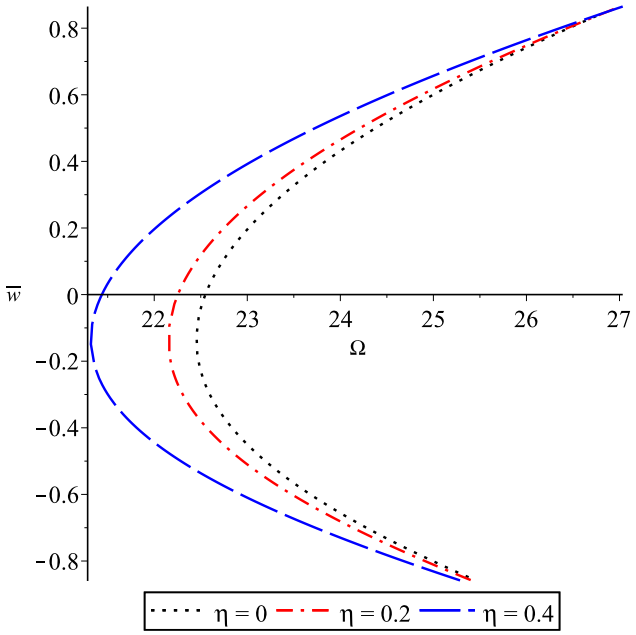

FIGURE 4.7: Total amplitude of vibration of the transverse displacement versus the non-linear natural frequency, when $V = 5$ volts.

voltage reaches 10 volts, Figure 4.8, significant changes in the dynamic behaviour of the nanobeam were registered, and highly non-linear effects are detected in the backbone

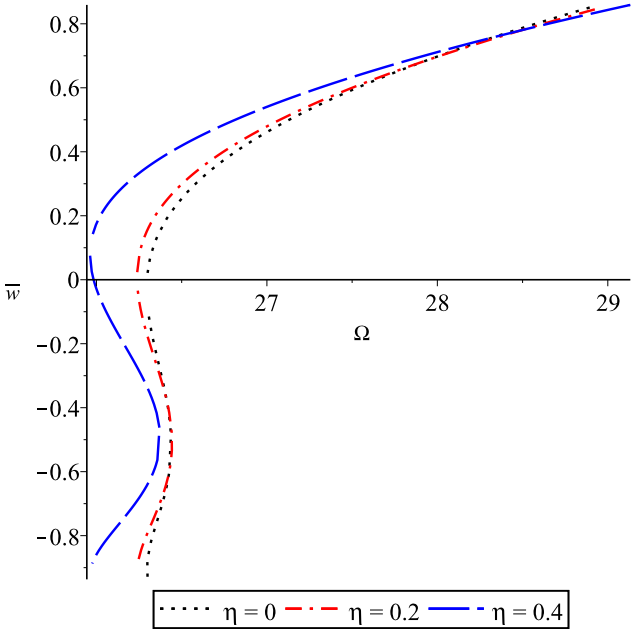

FIGURE 4.8: Total amplitude of vibration of the transverse displacement versus the non-linear natural frequency, when $V = 10$ volts.

curve. Softening effect and turning points were detected, demonstrating the complexity of this curve.

The nonlocal effects have a significant influence in the backbone curves of an electrostatically actuated nanobeam. Analysing the natural frequencies which correspond to the static deflection, one can see that the nonlocal parameter shifts the frequencies to lower values, just like it occurred in the linear analysis in the previous chapter. This frequency cannot be called a linear natural frequency since the initial condition corresponds to an already deflected beam witch introduces geometric non-linear terms, with exception of the 0 volt situation. Furthermore, the nonlocal effects lead to a more pronounced hardening and softening. To understand the influence of the nonlocal parameter in both effects, it is important to recall which terms are affected and the outcome in the natural frequencies. The nonlocal parameter increases the inertia terms, which will cause a decrease in the natural frequencies. It also affects the non-linear stiffness terms, by enhancing them (Figure 4.2), leading to an increase of the frequencies. The electrostatic force is also affected by this parameter, and as seen before, (in Figure 4.3), the higher the nonlocal parameter the higher the attraction force, which leads to a decrease of the natural frequencies. Due to all these effects of the non local parameter, in the stages of the vibration cycle where the frequencies decrease (softening), the nonlocal parameter will enhance this trend, and the opposite is also verified (hardening).

To fully understand softening and hardening effect, one needs to understand the

different stages of one vibration cycle. The static deflection of the beam causes geometric non-linear effects, which introduce an initial longitudinal tension to the beam, increasing its stiffness. When the oscillation is in its upward motion, the beam is gradually being submitted to a lower attraction force, since is farther to the static electrode, and at the same time the longitudinal tension decreases leading to a decrease in stiffness. As the cycle goes on, the beam passes through its horizontal position, and starts to deflect once again, which reintroduces the longitudinal tension, leading to a new increase in stiffness. When most part of oscillation cycle is dominated by a stiffness decrease, softening effect is detected. However, when most part of the cycle is dominated by an stiffness increase, hardening appears. Since large vibration amplitudes lead to higher geometric non-linearities (higher axial tensions), softening is usually detected for low amplitude values, where the phenomena that lead to lower natural frequencies prevail.

When no voltage is applied, only spring hardening is detected since the effects that lead to higher frequency values are always more dominant than the ones that lead to lower frequency values. This fact is also detected when the applied voltage is 5 volts, where the electrostatic force, which tends to decrease the natural frequencies, is always overridden by the geometric non-linearities, hence no softening effect is detected.

In order to justify and to deeply understand the backbone curves presented above, the evolution of the amplitude of each harmonics considered in the solution of the periodic response (Eq. 2.50), is presented. This analysis is going to be done for the cases where the applied voltage is 0, 5 or 10 volts, and the non dimension nonlocal parameter η is either 0 or 0.4.

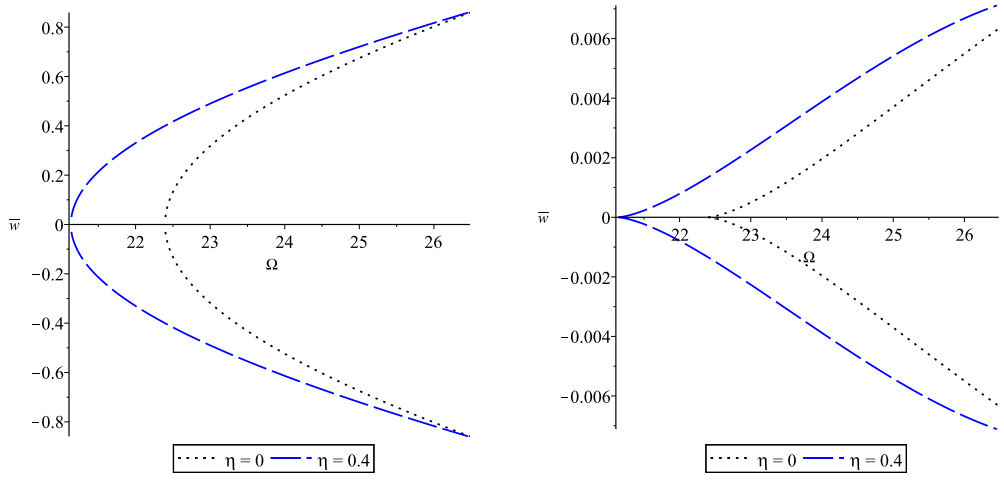

(a) 1^{st} harmonic (b) 3^{rd} harmonic

FIGURE 4.9: Amplitude of the harmonics of the transverse displacement when $V = 0$ volt, for two values of the nonlocal parameter.

When no voltage considered, the only excited harmonics are the odd ones, and the

constant term and the second harmonic have no influence in the system's response. This happens because when no electrostatic force is considered, the system is represented by a non-linear equation of the Duffing type, i.e there are only odd non-linearities. When the electrostatic force is considered, even non-linearities are originated, and the system is no-longer represented by an equation of the Duffing type, and consequently the even harmonics affect the system dynamics. In Figure 4.9 it's clear that the first harmonic is the most dominant in the total response, by comparing the difference of the amplitude range of both harmonics represented.

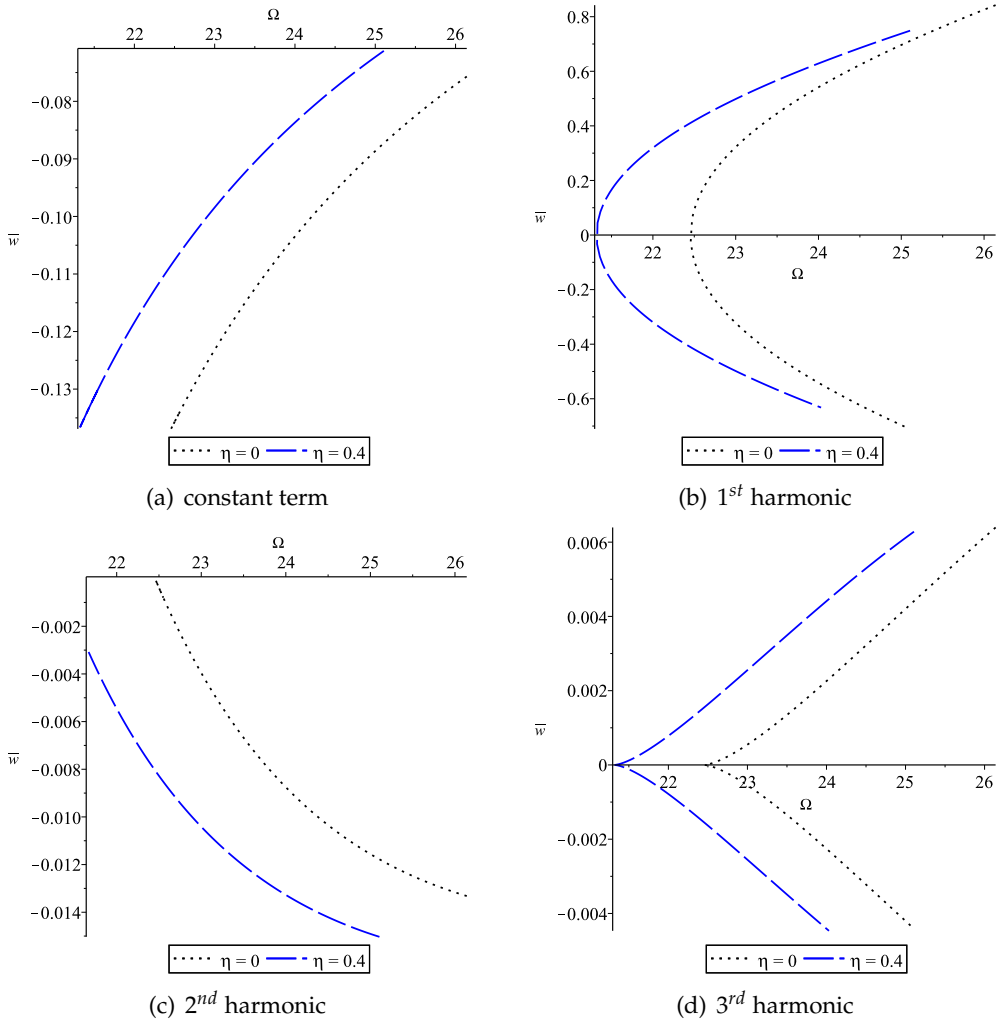

(a) constant term

(b) 1^{st} harmonic

(c) 2^{nd} harmonic

(d) 3^{rd} harmonic

FIGURE 4.10: Amplitude of the harmonics of the transverse displacement when $V = 5$ volts, for two values of the nonlocal parameter.

When the voltage applied is 5 volts, the system has an evident asymmetric behaviour. Analysing Figure 4.10, the asymmetry is explained by the presence of the even

harmonics, which have always the same sign for the frequency range considered, while the odd harmonics have a symmetric representation. On the other hand, the offset that has been detected in the backbone curves of Figure 4.7 is caused by the constant term which presents its higher magnitude values for low values of the vibration amplitude. The fact that magnitude of the constant term tends to zero as the motions evolves, can be explained by the increase stiffness of the beam. The second and the third harmonic have a small influence in the total response of the system, and as in the previous case, the first harmonic is the most dominant one. The nonlocal parameter causes the frequencies to shift to lower values, changing the frequency/amplitude relation.

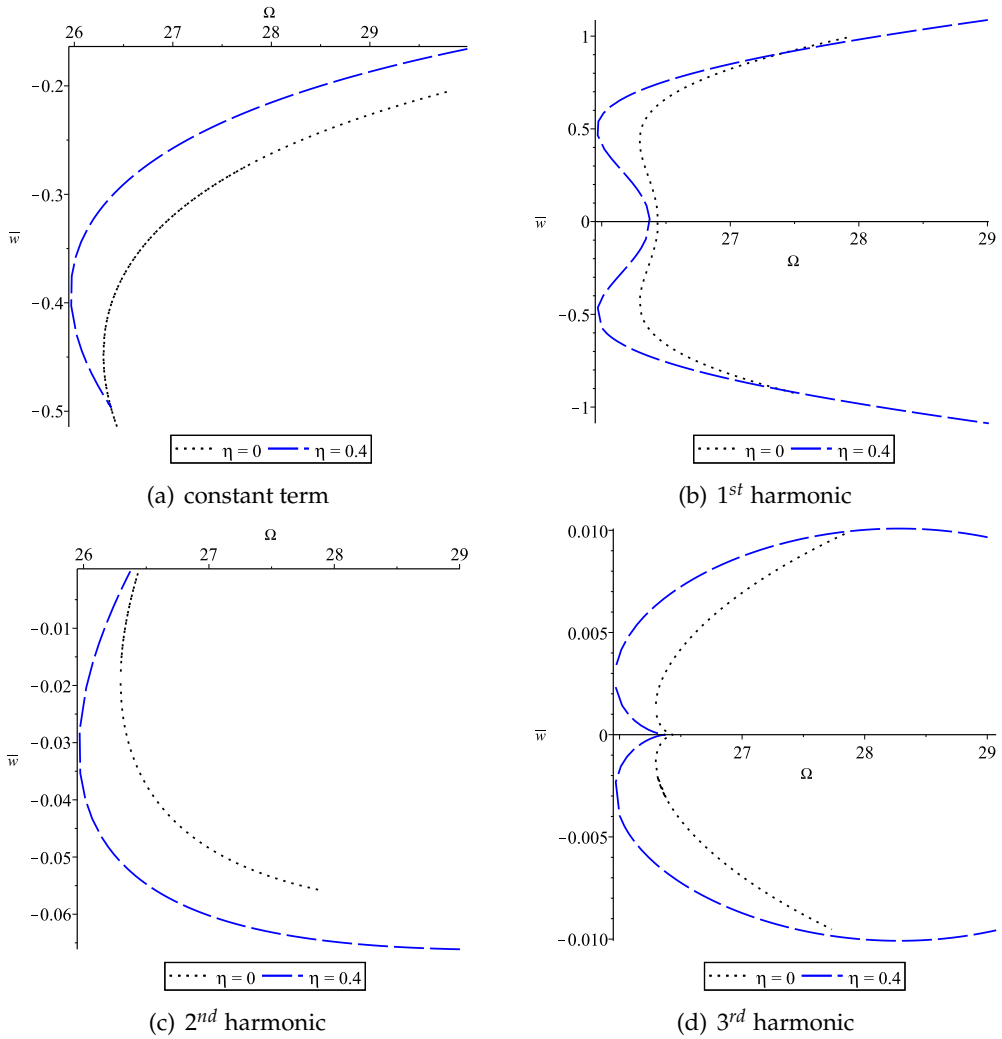

(a) constant term

(b) 1^{st} harmonic

(c) 2^{nd} harmonic

(d) 3^{rd} harmonic

FIGURE 4.11: Amplitude of the harmonics of the transverse displacement when $V = 10$ volts, for two values of the nonlocal parameter.

Increasing the voltage to 10 volt, turning points and softening behaviour were

detected in the backbone curves of Figure 4.8. In Figure 4.11, the constant term has a strong influence for frequencies close to the linear one, causing a considerable offset in what the amplitudes are concerned. Adding to this, the second harmonic, despite presenting small values of magnitude, also contributes to the asymmetric behaviour of the system. The odd harmonics present a softening behaviour for low amplitude values, which then becomes hardening as the oscillation amplitudes increase. The first harmonic is still the most dominant one, however, the constant term has a big influence for frequencies close to the linear one. The nonlocal parameter, once again shifts the frequencies to lower values, and enhances both the softening and hardening effect that occur in the odd harmonics.

In Figures 4.12 to 4.15, the shapes assumed by the constant term and the harmonics are presented, when the voltage applied is 5 volts and the nonlocal parameter η is either 0 or 0.4. The shapes are also calculated for four different amplitudes of the nanobeam's oscillation and the amplitude of each harmonic is normalized in a way, that the maximum amplitude of all harmonics at the middle of the nanobeam assumes the value 1.

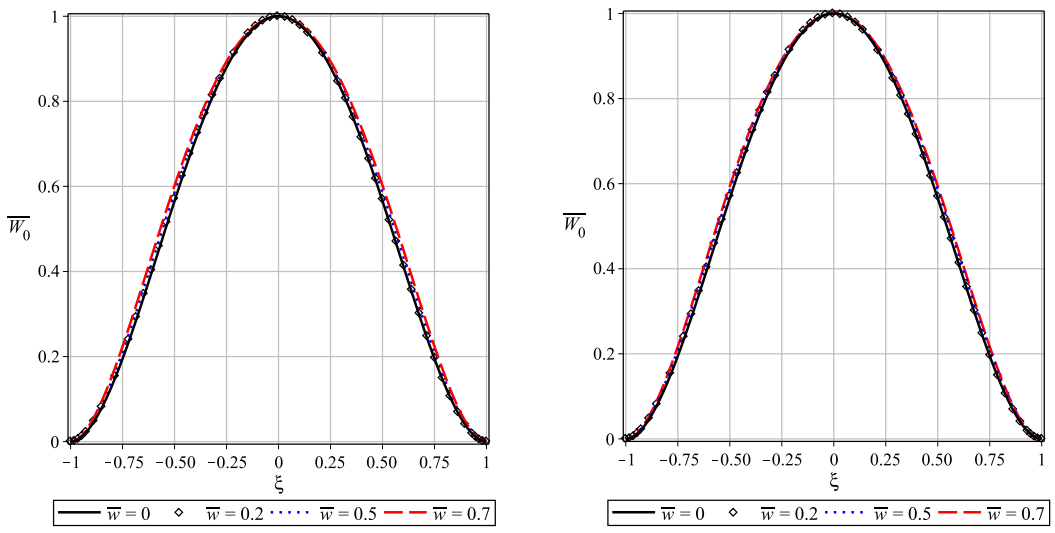

(a) constant term, $\eta = 0$

(b) constant term, $\eta = 0.4$

FIGURE 4.12: Shape of the constant term of the transverse displacement when $V = 5$ volts, for two values of the nonlocal parameter.

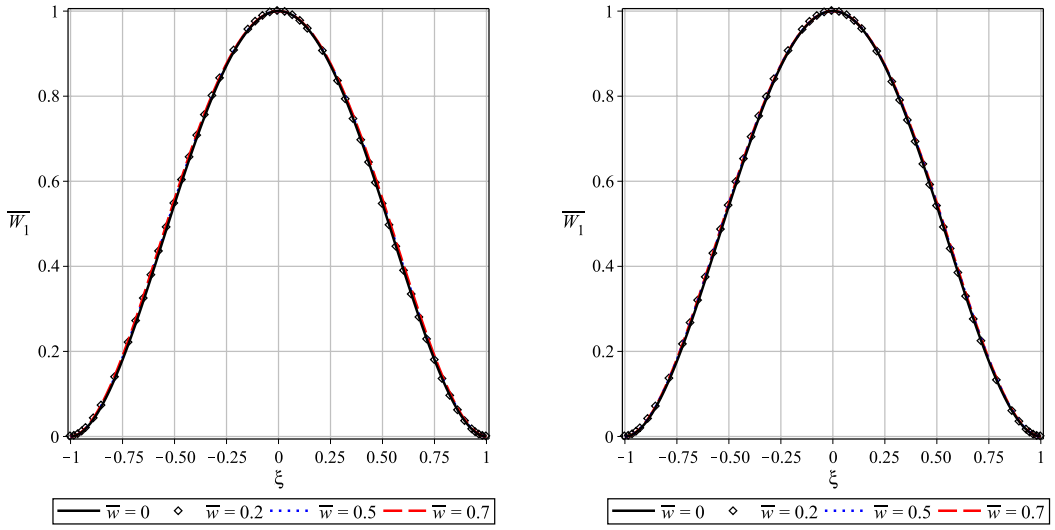

(a) 1^{st} harmonic, $\eta = 0$ (b) 1^{st} harmonic, $\eta = 0.4$

FIGURE 4.13: Shape of the 1^{st} harmonic of the transverse displacement when $V = 5$ volts, for two values of the nonlocal parameter.

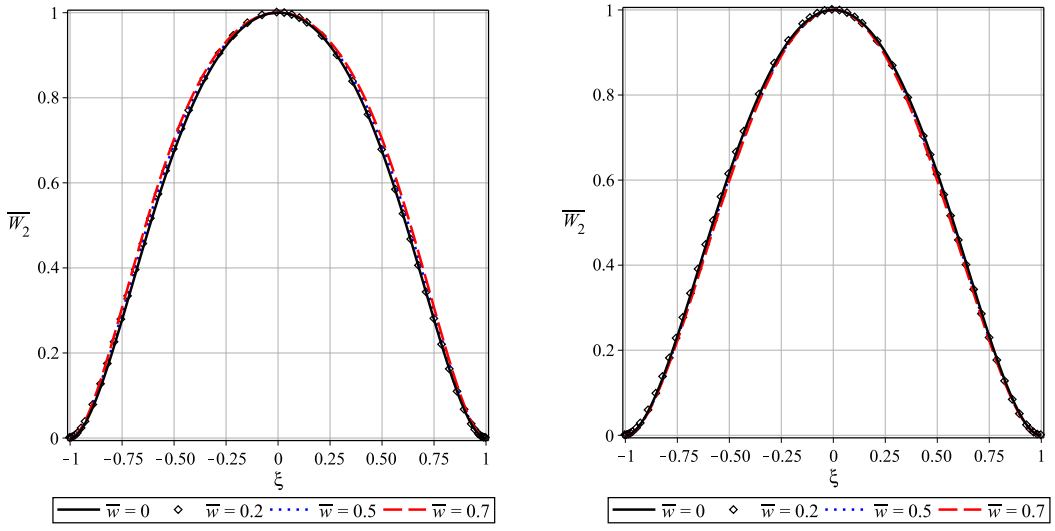

(a) 2^{nd} harmonic, $\eta = 0$ (b) 2^{nd} harmonic, $\eta = 0.4$

FIGURE 4.14: Shape of the 2^{nd} harmonic of the transverse displacement when $V = 5$ volts, for two values of the nonlocal parameter.

Comparing the shapes of the constant term and the first harmonic with the vibration amplitude, no significant changes are detected for both values of the nonlocal parameter. Analysing the second harmonic, although its shape is not sensitive to changes in the vibration amplitude, one can see that when the nonlocal parameter is zero the shape

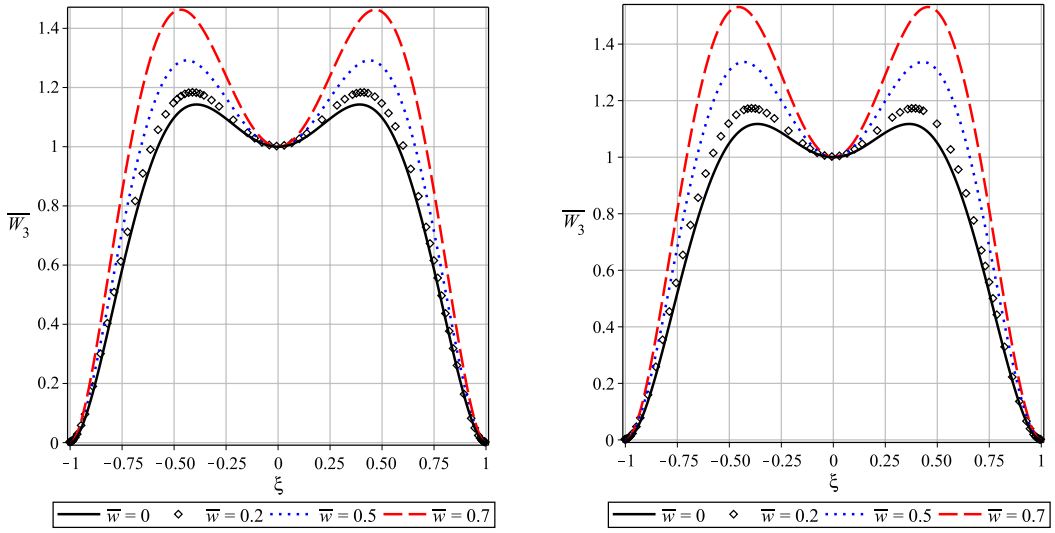

(a) 3^{rd} harmonic, $\eta = 0$

(b) 3^{rd} harmonic, $\eta = 0.4$

FIGURE 4.15: Shape of the 3^{rd} harmonic of the transverse displacement when $V = 5$ volts, for two values of the nonlocal parameter.

presents a rounder an wider form than when the nonlocal parameter is 0.4. Finally the shape of the third harmonic is highly affected by the vibration amplitude, and the nonlocal parameter has little effect on the shape of this harmonic. The shape is also defined by the first and second symmetric modes of vibration, being this last one more important for higher values of the amplitude of vibration.

In order to see the evolution of the shapes of the nanobeam with time, the transverse deflection given by Eq. (2.50 a) is considered, as well as the evolution of the rotation of each section of the beam, which is given by Eq. (2.50 b). In Figure 4.16, the transverse oscillations of the nanobeam during half a period of vibration are considered, for a local and a nonlocal case and the same representation is done for the rotations in Figure 4.17. All cases are represented for an amplitude of the first harmonic approximately equal to $\bar{w} = 0.3$. Analysing the transverse shape, both local and nonlocal representations are very similar, although in the local case, the maximum negative displacement is slightly bigger than the local case. Another difference between the local and nonlocal situation lies in their natural frequency of vibration: $3.3557 \times 10^9 rad/s$ for the local case, and $3.21459 \times 10^9 rad/s$ for the non-local one. The difference in the nonlocal and local rotations are the same of the ones presented for the transverse shape. After this analysis, it becomes clear that the shape assumed by the nanobeam during one vibration period is not the same as the first linear mode shape, due to the influence of the non-linear terms (geometric and electrostatic).

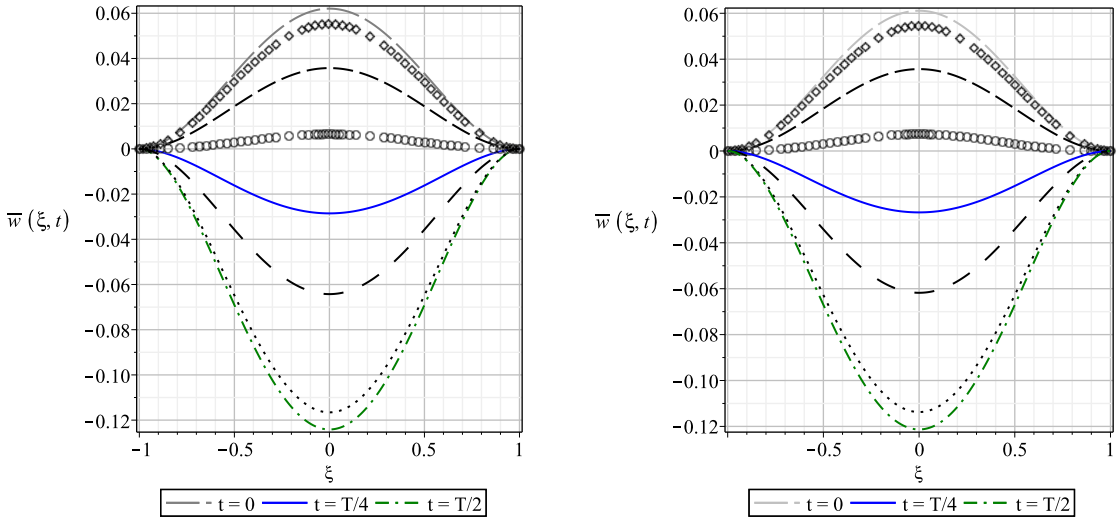

(a) $\eta = 0$ (b) $\eta = 0.4$

FIGURE 4.16: Shape of the nanobeam's first transverse mode at different instants along half a period of vibration, when $V = 5$ volts and $\bar{w} = 0.5$.

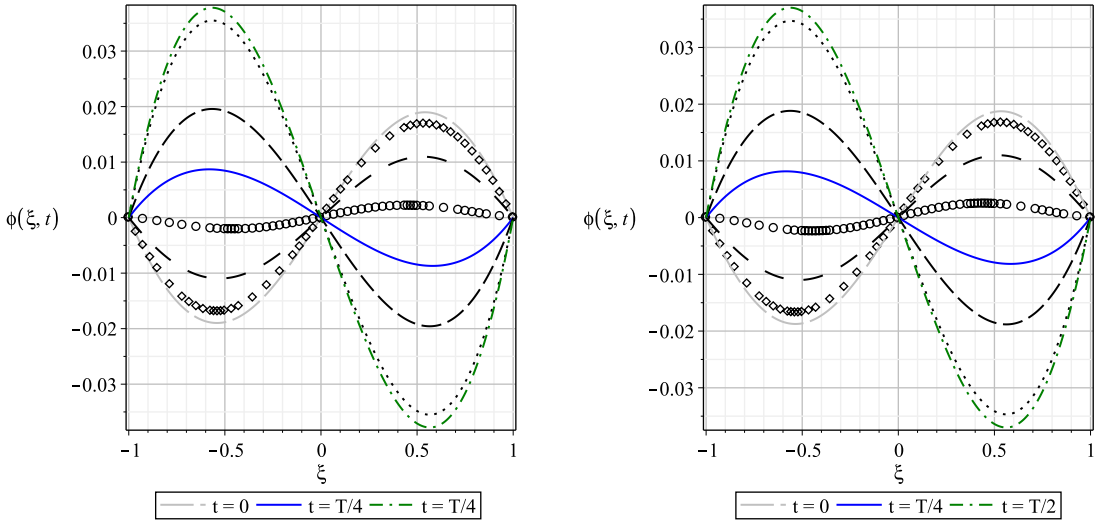

(a) $\eta = 0$ (b) $\eta = 0.4$

FIGURE 4.17: Shape of the nanobeam's first rotation mode at different instants along half a period of vibration, when $V = 5$ volts and $\bar{w} = 0.5$.

In Figures 4.18 to 4.21, the same analysis as before is done to the shapes of the constant term and the harmonics, but in this case the voltage considered is 10 volts.

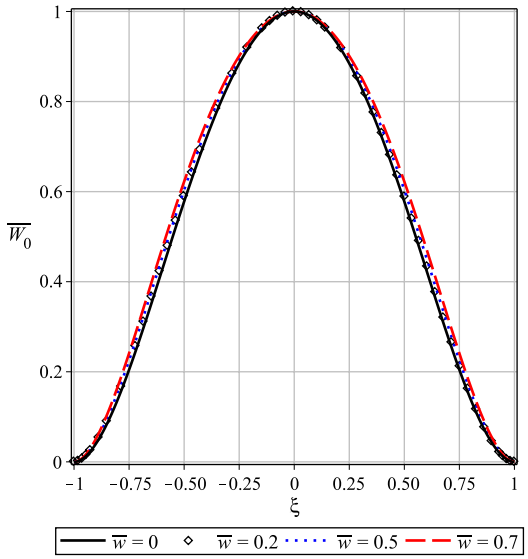

(a) constant term, $\eta = 0$

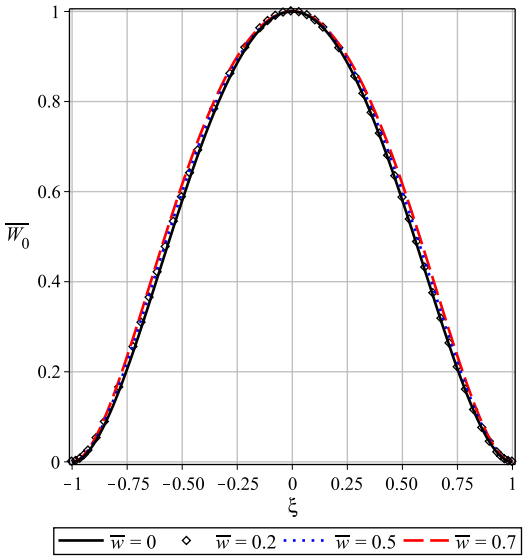

(b) constant term, $\eta = 0.4$

FIGURE 4.18: Shape of the constant term of the transverse displacement when $V = 10$ volts, for two values of the nonlocal parameter.

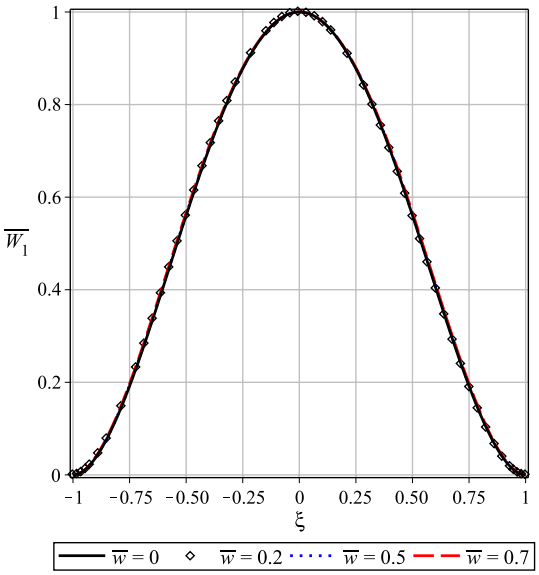

(a) 1^{st} harmonic, $\eta = 0$

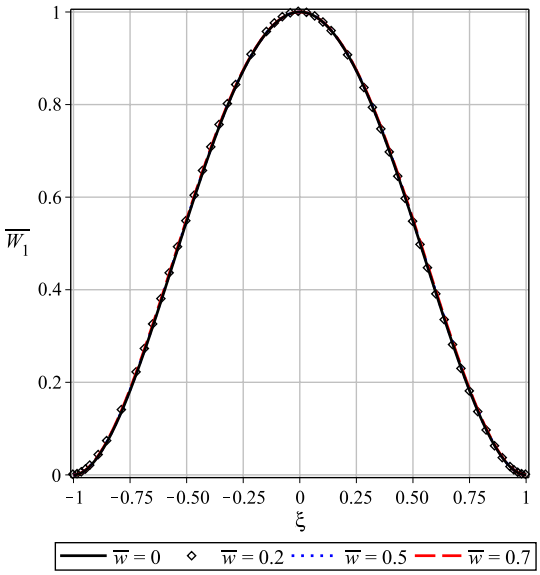

(b) 1^{st} harmonic, $\eta = 0.4$

FIGURE 4.19: Shape of the 1^{st} harmonic of the transverse displacement when $V = 10$ volts, for two values of the nonlocal parameter.

In this analysis, the shape of the constant term suffers small changes for different values of $\bar{w}$ while the shape of the first harmonic remains the same. Both the constant

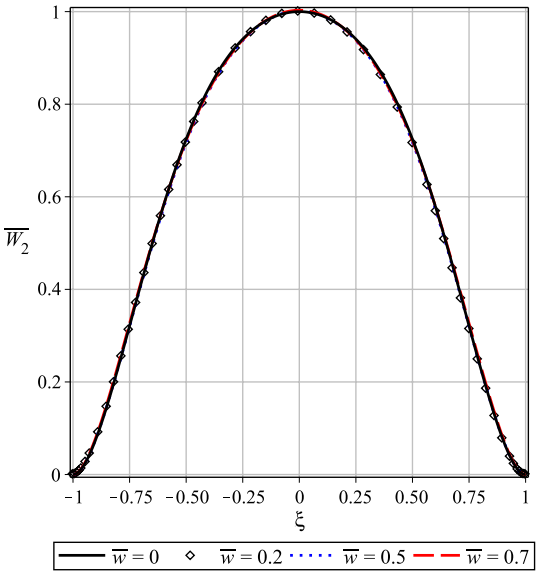

(a) 2^{nd} harmonic, $\eta = 0$

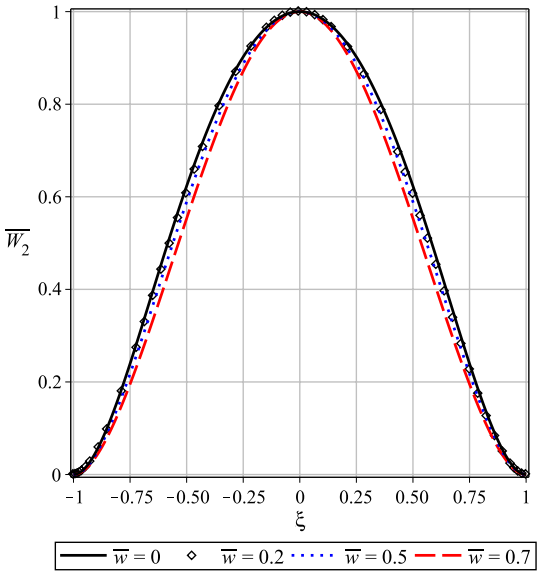

(b) 2^{nd} harmonic, $\eta = 0.4$

FIGURE 4.20: Shape of the 2^{nd} harmonic of the transverse displacement when $V = 10$ volts, for two values of the nonlocal parameter.

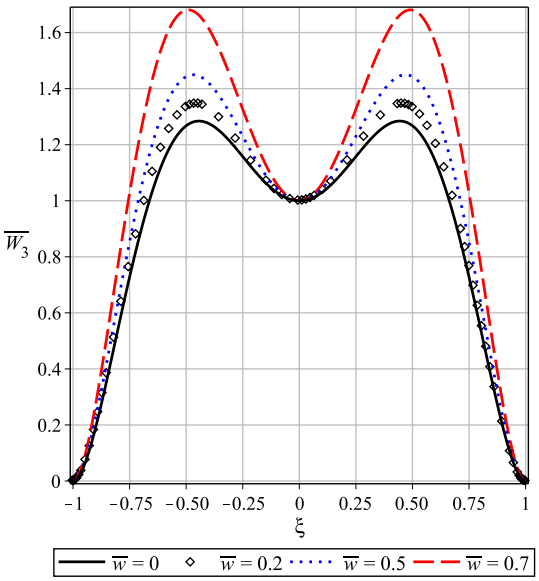

(a) 3^{rd} harmonic, $\eta = 0$

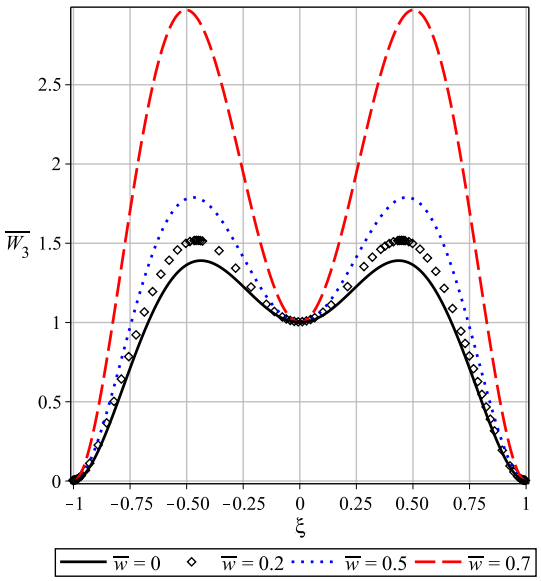

(b) 3^{rd} harmonic, $\eta = 0.4$

FIGURE 4.21: Shape of the 3^{rd} harmonic of the transverse displacement when $V = 10$ volts, for two values of the nonlocal parameter.

term and the first harmonic are insensitive to nonlocal effects. The second harmonic however, presents considerable variations when the nonlocal effects are considered. In the local case, the mode shape has an evident rounder form than the nonlocal case, similar to what happened when the voltage applied was 5 volts. The third harmonic is the one that demonstrated a higher sensitivity to changes in amplitude and nonlocal effects.

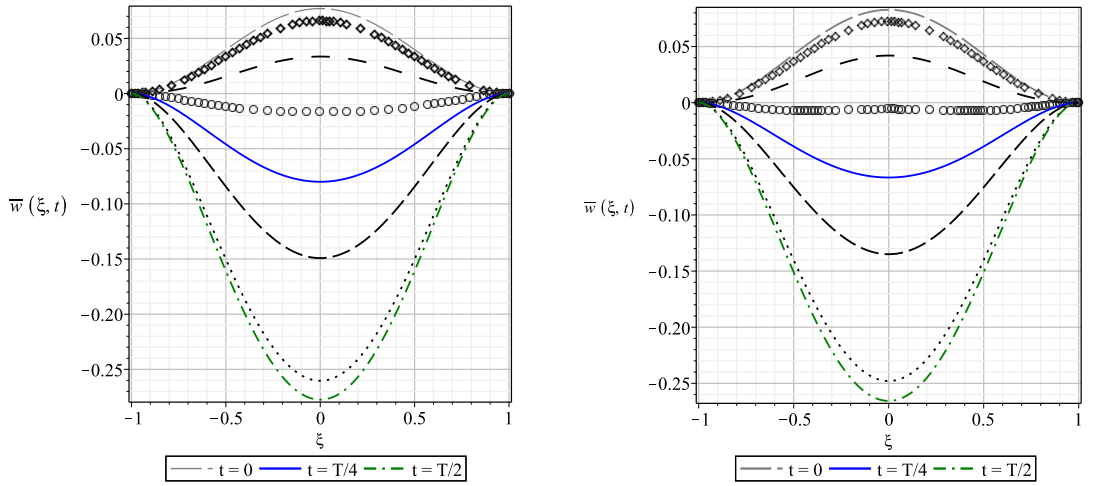

(a) $\eta = 0$ (b) $\eta = 0.4$

FIGURE 4.22: Shape of the nanobeam's first transverse mode at different instants along half a period of vibration, when $V = 10$ volts and $\bar{w} = 0.5$.

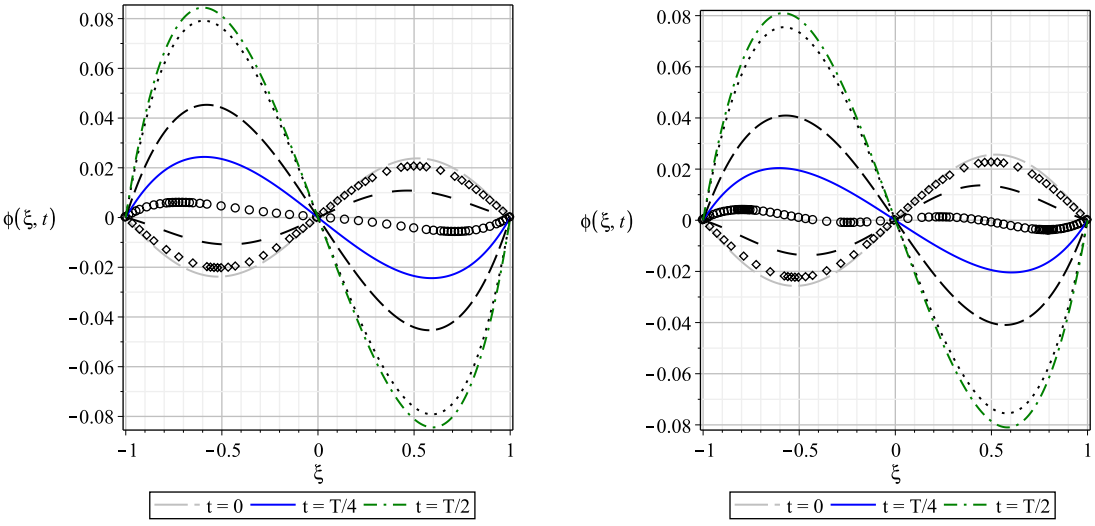

(a) $\eta = 0$ (b) $\eta = 0.4$

FIGURE 4.23: Shape of the nanobeam's first rotation mode at different instants along half a period of vibration, when $V = 10$ volts and $\bar{w} = 0.5$.

In Figure 4.22 the transverse deflection of the nanobeam is plotted for different instants of half a period of vibration, when the voltage applied is 10 volts, and in Figure 4.23 the beam's cross section rotation is shown. Comparing the representation of the transverse deflection to the one in Figure 4.16, the most evident difference is that despite both representations were made for the same positive amplitude ($\bar{w} = 0.5$), the maximum negative amplitude of vibration is much higher when the applied voltage is 10 volts, since the attraction force is higher. Looking at the nonlocal effects, one can see that they lead to higher positive deflection values and lower negative ones. It is also possible to see the influence of the third harmonic in Figures 4.22b and 4.23b, for low values of the vibration amplitude, although this influence is small due to clear dominance of the first harmonic in the system's overall dynamics.

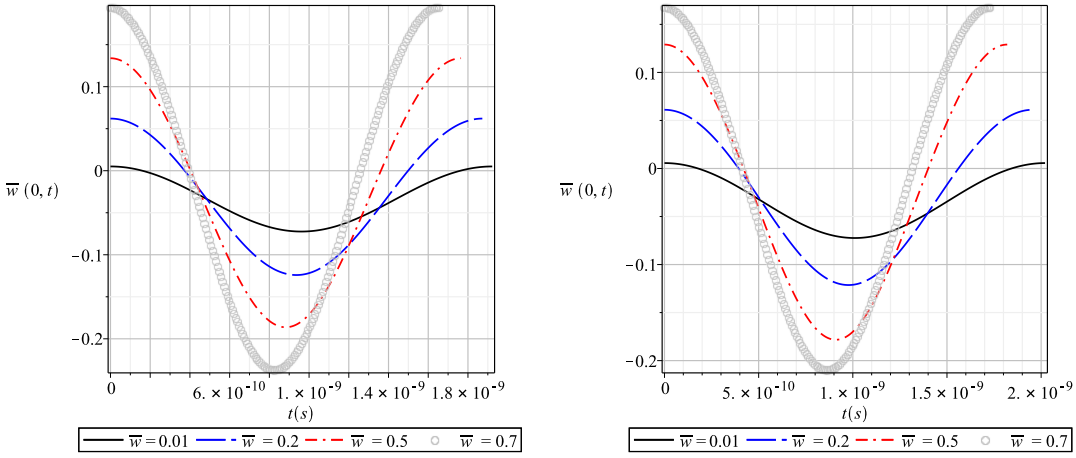

(a) $\eta = 0$, $V = 5$ (b) $\eta = 0.4$, $V = 5$

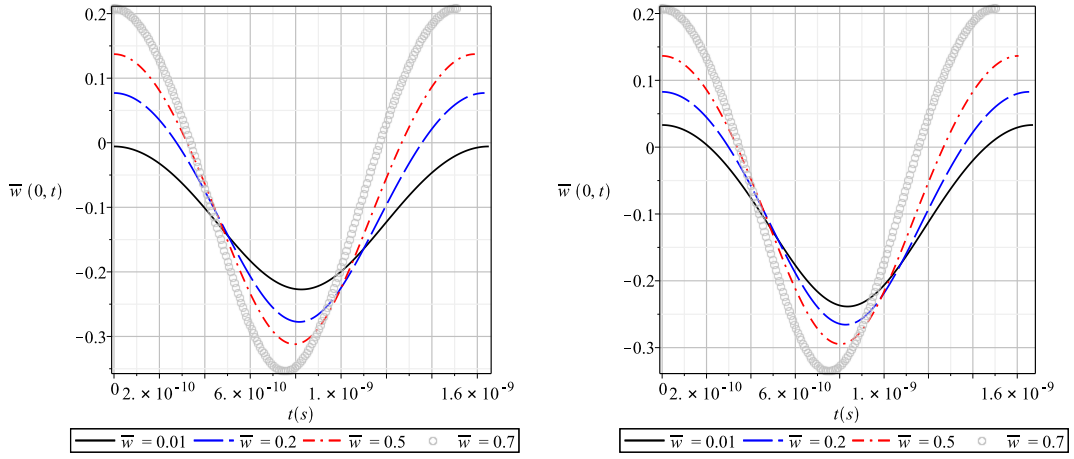

(c) $\eta = 0$, $V = 10$ (d) $\eta = 0.4$, $V = 10$

FIGURE 4.24: Time evolution of the nanobeam's middle point transverse displacement for a local and a nonlocal case, when the voltage is either 5 or 10 volts.

The time evolution of the nanobeam's middle point displacement, during one vibration cycle, represented in Figure 4.24, clearly shows the maximum and minimum values the displacement assumes for the values of voltage an nonlocal parameters considered. The information given by Figures 4.16 and 4.22, is also presented in this time displacement evolution. One can see that most part of the vibration cycle occurs for negative values of displacement, due to the initial static deflection. As the amplitude of vibration increases, the time the middle point of the beam spends in positive values of deflection also increases and almost reaches half a vibration period. Once again, the influence of nonlocal parameter in the minimum displacement value is also well represented, as well as in the natural frequencies, which in this case changes the value of the vibration period.

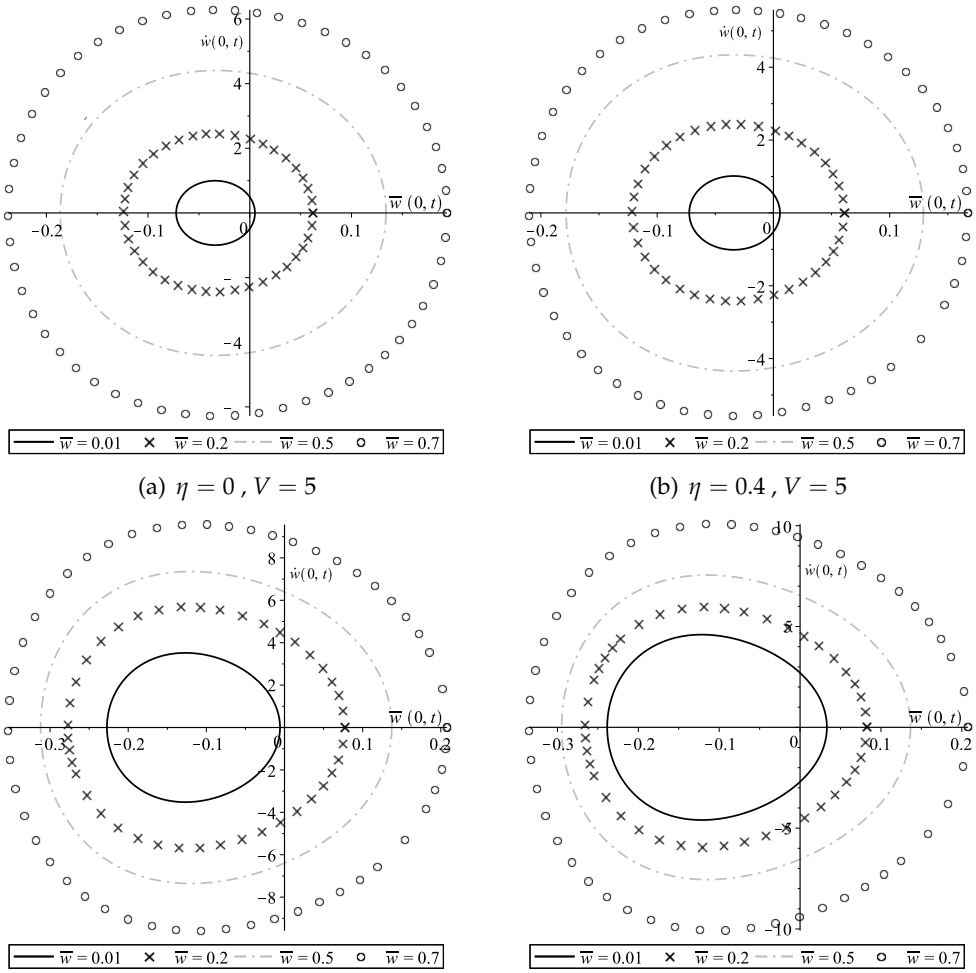

(a) $\eta = 0$, $V = 5$

(b) $\eta = 0.4$, $V = 5$

(c) $\eta = 0$, $V = 10$

(d) $\eta = 0.4$, $V = 10$

FIGURE 4.25: Phase plot - velocity versus transverse displacement of the nanobeam's middle point for two values of voltage and two different nonlocal parameters.

Another interesting way to show the evolution of the system dynamics is through a phase plot, Figure 4.25, where the middle point displacement is related to its velocity. One can see that all phase plots are not symmetric to the velocity axis, due to the initial deflection of the beam that causes the displacement offset. However, the phase plots are symmetric to the displacement axis, which means that for a fixed displacement value, the velocity of the middle point in the upward motion is equal to the velocity in the downward motion, which is expected. The effect of the applied voltage is also visible, and as it increases the phase-plot trajectories increase as well, which means that the system is submitted to higher displacements and velocities. The effect of the nonlocal parameter is also easily detected, as is changes the maximum displacements, for the same applied voltage, as well as the shape of the phase-plot trajectories leading to a more visible asymmetry of the system.

In order to see the influence of the applied voltage in the dynamic behaviour of higher modes of vibration, the second symmetric mode (i.e the third mode of vibration) is analysed when the voltage applied is 5 volts and no nonlocal effects are considered.

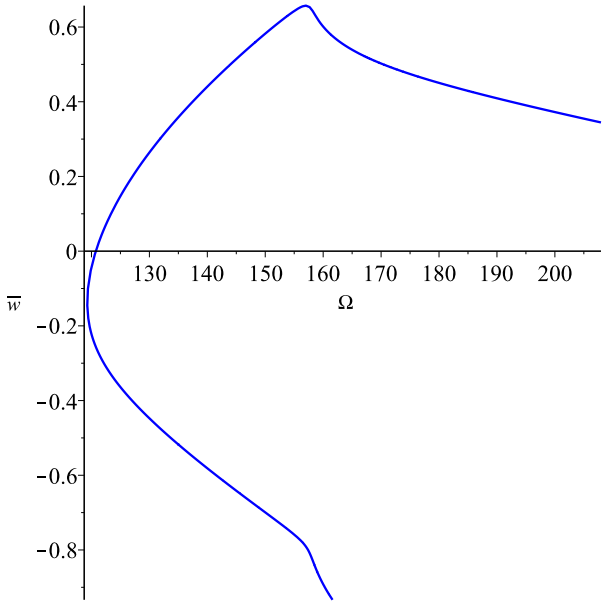

FIGURE 4.26: System backbone curve for the 3^{rd} mode when $V = 5$ volts.

The backbone curve presented in Figure 4.26 shows the existence of an amplitude offset, just like it occurred in the first mode, however the amplitude of displacement starts do decrease as the frequency assumes higher values. This fact is explained by an internal resonance that occurs, which will be explored next. The amplitude of each harmonic and of the constant term are plotted in Figures 4.27.

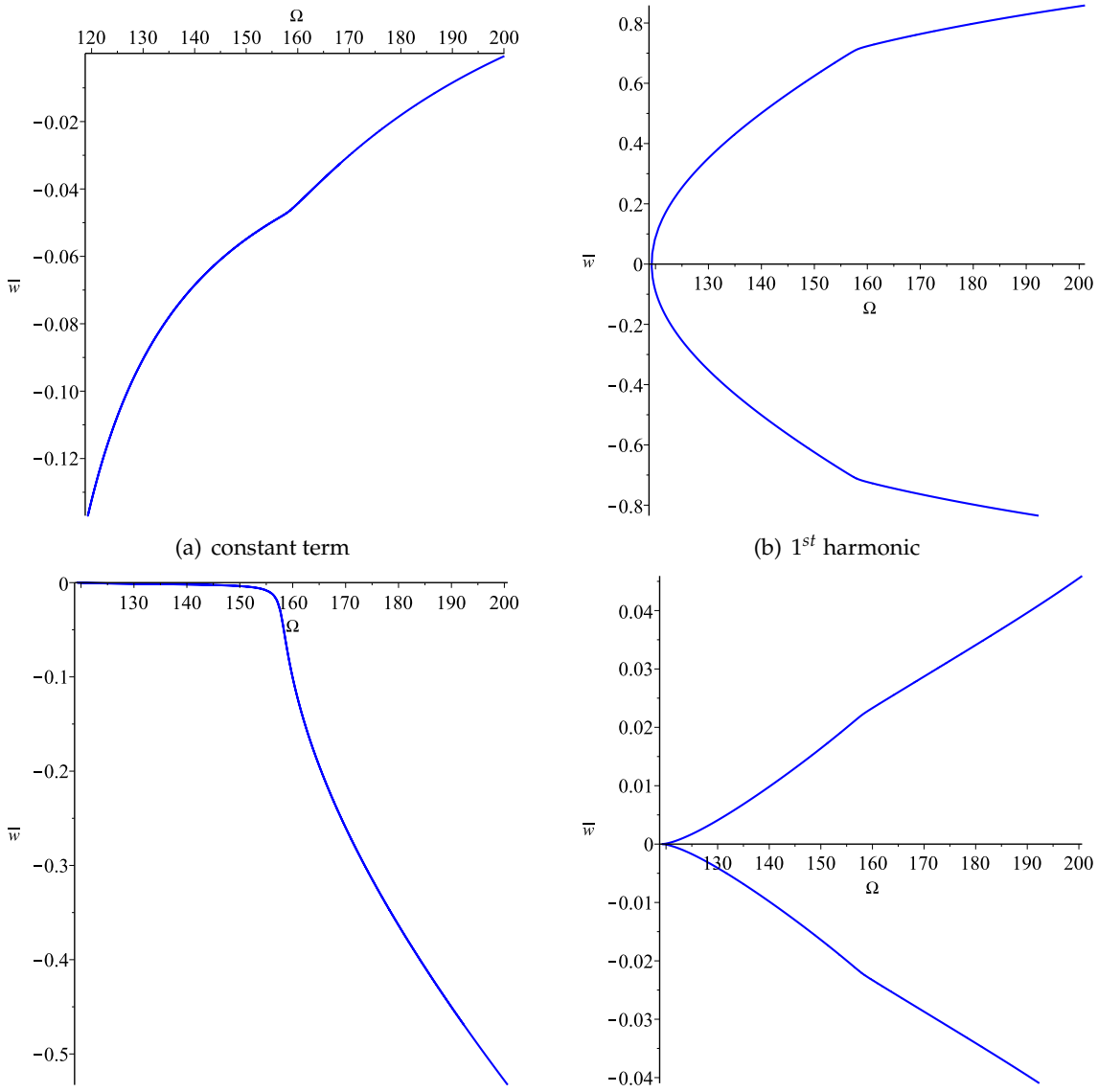

(a) constant term

(b) 1^{st} harmonic

(c) 2^{nd} harmonic

(d) 3^{rd} harmonic

FIGURE 4.27: Amplitude of the constant term and 1^{st} harmonic for the 3^{rd} mode, when $V = 5$ volts.

Analysing the amplitude of each harmonic, its clear that a 1:2 internal resonance occurs. As expected the first harmonic is the most dominant for low frequencies, however, the second harmonic has a growing importance in the vibration of the nanobeam, and when $\Omega \approx 157$, its amplitude suffers a sudden increase. The shape assumed by each harmonic and by the constant term are presented in the following figures, and will help to understand with modes of vibration are coupling in the detected

internal resonance.

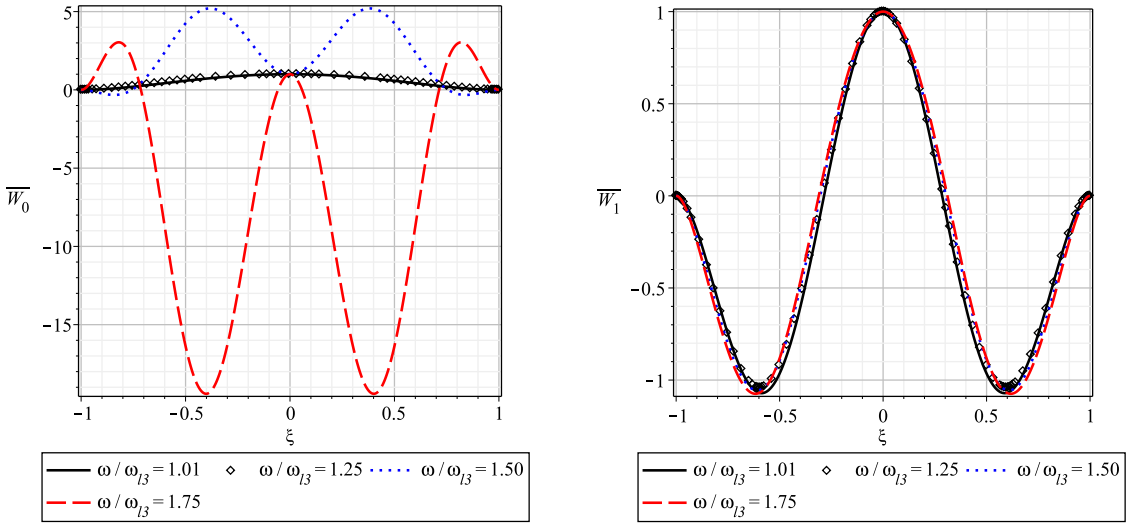

(a) constant term (b) 1^{st} harmonic

FIGURE 4.28: Shape of the constant term and the first harmonic for the second symmetric mode, when $V = 5$ volts.

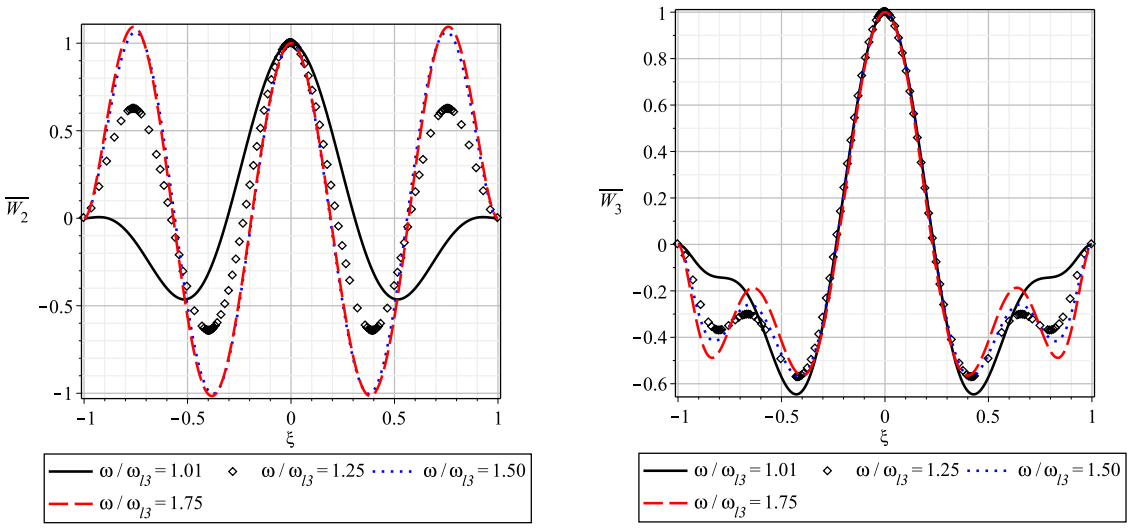

(a) 2^{nd} harmonic (b) 3^{rd} harmonic

FIGURE 4.29: Shape of the second and the third harmonic for the second symmetric mode, when $V = 5$ volts.

In Figures 4.28 one can see the shape of the constant term and the first harmonic.

It is interesting to see that the shape of the constant term changes drastically with the frequency of vibration, assuming the shape of the first symmetric mode for low frequencies and the shape of the third symmetric mode for higher frequencies. The shape of the first harmonic suffers small variations for different values of frequency and has the shape of the second symmetric mode.

In Figure 4.29, the shape of the second harmonic changes with the frequency of vibration and gradually assumes the shape of the third symmetric mode. Finally the third harmonic presents a strange shape, similar to the fourth symmetric mode, and is also sensitive to changes in the frequency of vibration.

When the first harmonic vibrates at $\omega = 0.2 \times 10^{12} rad/s$, the second harmonic will have a frequency of $0.4 \times 10^{12} rad/s$ which is close to the fifth natural frequency ($\omega_5 = 0.41 \times 10^{12} rad/s$). This way, the third mode of vibration will couple with the fifth mode, leading to energy exchanges between them, which explains the $1:2$ internal resonance detected. This will lead to significant changes in the shape of beam during the period of vibration, as the second harmonic gradually becomes more important in the total response of the beam. This change in shape of the beam can be seen in figure 4.30, as it its plotted for different instants along half its period of vibration.

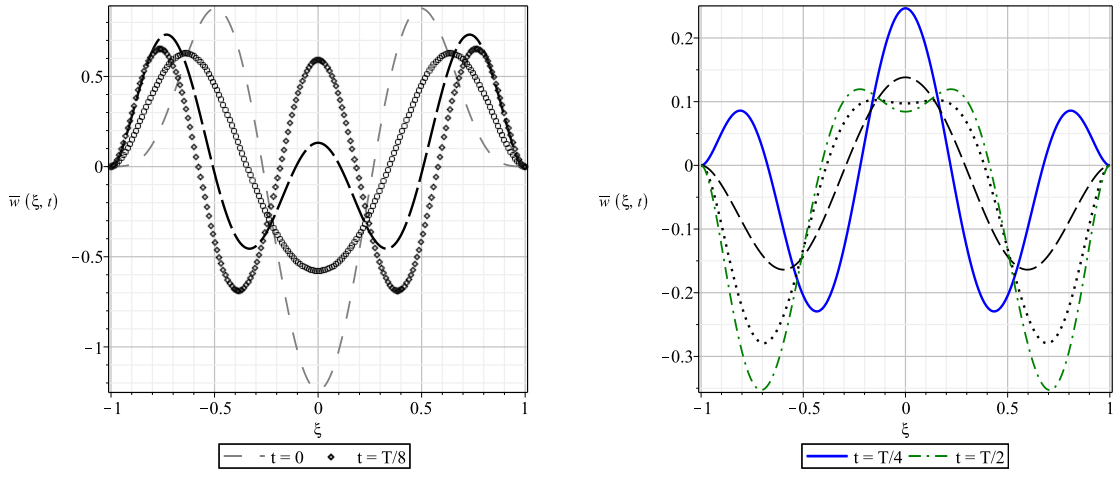

FIGURE 4.30: Shape of the beam when vibrating at its third mode, along half a period of vibration, when $V = 5$ volts.

When $t = 0$, the first harmonic is clearly the most dominant, and the beam assumes the shape of the second symmetric mode. As the motions develops, the second harmonic gradually affects the overall shape of the beam, and at half the period of vibration, $t = T/2$, one can see the clear influence of the second symmetric mode by the first harmonic added to the influence of the third symmetric mode by the second harmonic.

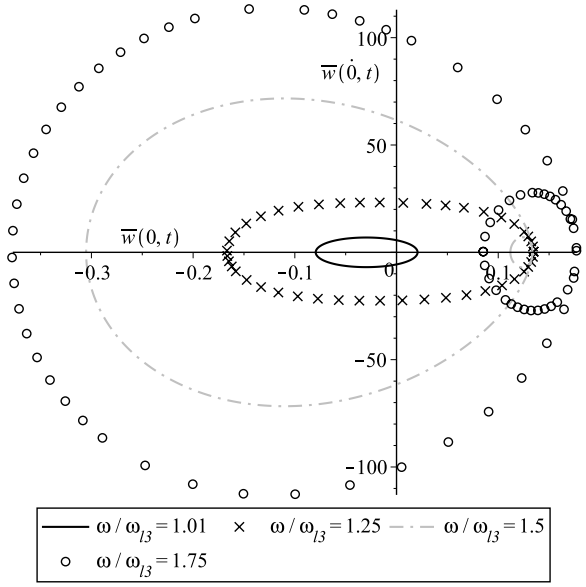

FIGURE 4.31: Phase plot - velocity versus displacement of the nanobeam's middle point when the beam is vibrating at its third mode, and $V = 5$ volts.

The phase plot of Figure 4.31 shows the influence of the internal resonance for high frequency values, as the middle point of the beam describes two circular trajectories in the displacement-velocity plane. All trajectories are symmetric in relation to the displacement axis, and the voltage applied causes a shift to negative values of displacement.

4.3.1 INFLUENCE OF THE BEAM LENGTH IN THE SYSTEM DYNAMICS

The evolution of the backbone curves is dependent on the relation between the attraction of the electrostatic force and the variations in the beam stiffness. One important geometric property that changes the deflection of the beam, and automatically causes significant changes in the system dynamics, is the length L, of the nano beam, which will be represented in a non dimension form $\bar{L} = L/h$. The following analysis considers the same properties presented in Tables 4.2 and 4.1, and considers three values for $\bar{L}$ (30, 40, 50).

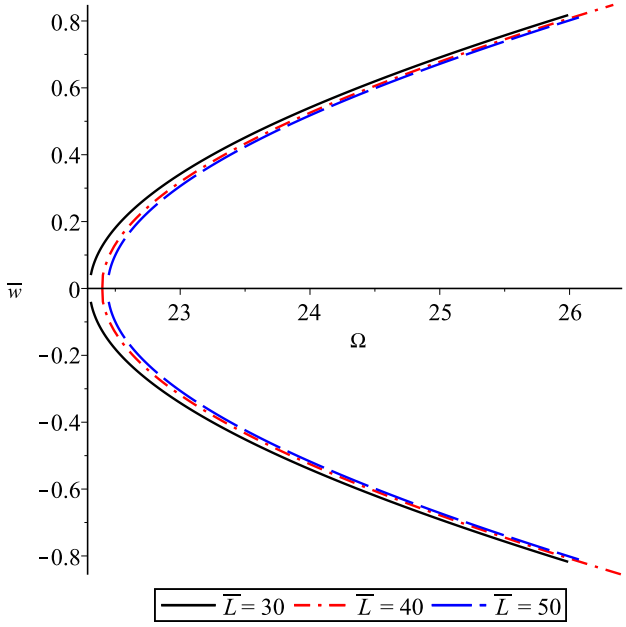

FIGURE 4.32: System backbone curve when $V = 0$ volts.

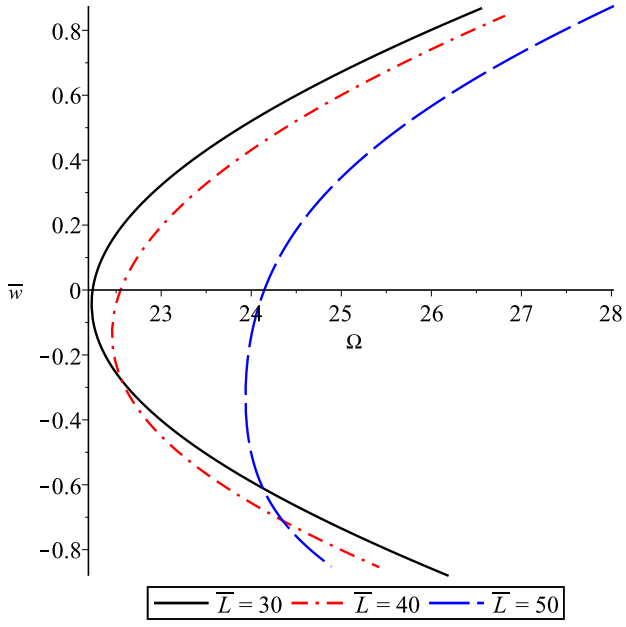

FIGURE 4.33: System backbone curve when $V = 5$ volts.

Attending to Figure 4.32, the fact that a shorter beam presents lower non dimensional frequency is misleading. This is justified by the expression used to determine the non dimensional frequency, which is proportional to the square of length of the beam (see

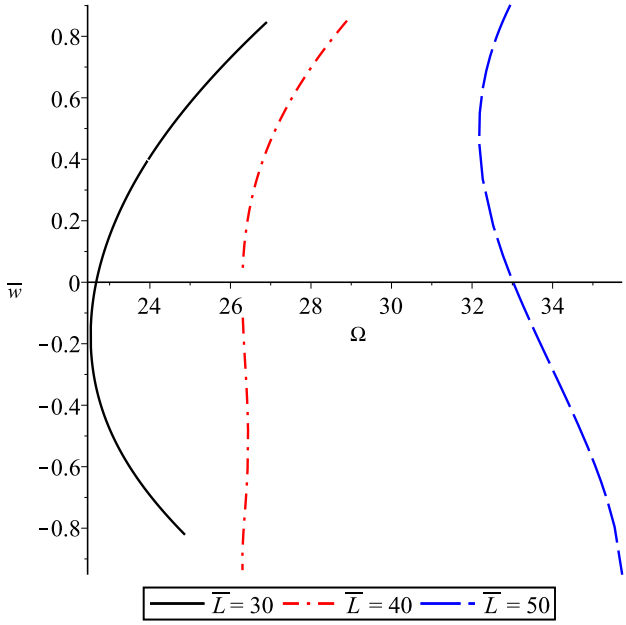

FIGURE 4.34: System backbone curve when $V = 10$ volts.

Eq. 3.2). However, the natural frequencies in rad/s are higher for shorter beams. For all values of $\bar{L}$ only spring hardening is detected, as expected, since no external force is considered. One can also see that although the spring hardening rate is similar in all situations, the shorter beam is the one that presents the higher. This is explained by the fact that for the same amplitude displacement, the shorter beam is the one who suffers more with the geometric non-linearities and consequently will present higher hardening rates than more slender beams.

In Figure 4.33 a 5 volt voltage is applied. One is able to see that the more slender beam has a more significant offset, caused by the constant term. Since the more slender beam has a lower stiffness, it will present a higher static deflection, which in turn will lead to a stronger attraction force, as it is closer to the stationary electrode. In this situation, only hardening spring effect is detected, and like when no voltage is applied, the shorter beam presents higher rates of hardening. When the voltage rises up to 10 volts, extremely different dynamic behaviours are detected. The shorter beam once again only presents a hardening effect, due to its low static deflection. In the longer beams, one can see both hardening and softening effect, however, the softening is much more pronounced when $\bar{L} = 50$, due to the higher static deflection, which initially leads to higher axial tensions. The tension gradually assumes lower values as the beam starts to vibrate, which will lead to a decrease in the frequency values, and a well marked softening effect. The natural frequencies for each beam are also extremely different, due to the high applied voltage and to the difference in length of the beams.

4.3.2 INFLUENCE OF THE GAP SIZE IN THE SYSTEM DYNAMICS

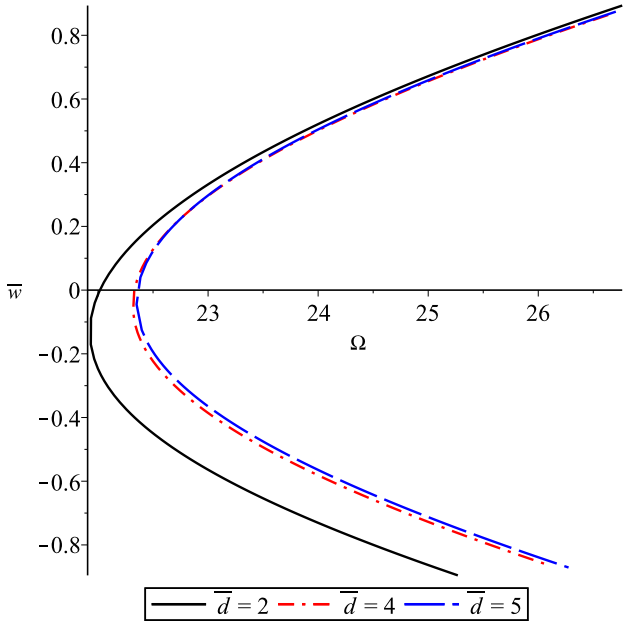

FIGURE 4.35: Total amplitude of vibration of the transverse displacement versus the non-linear natural frequency, when $V = 3$ volts.

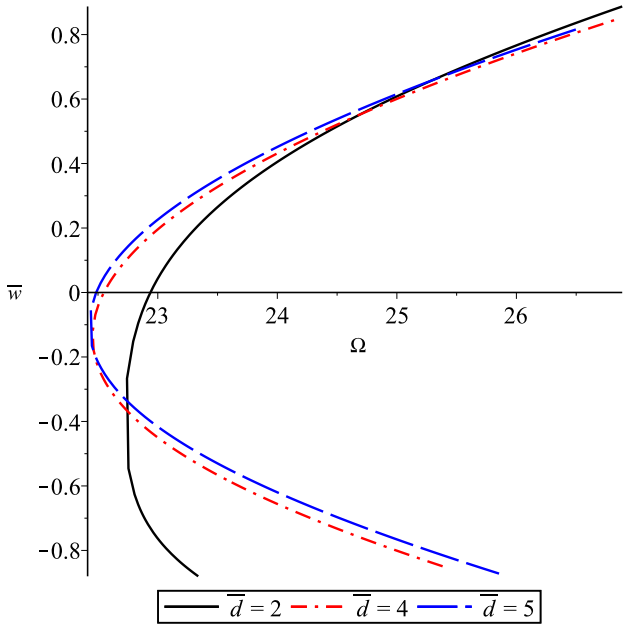

FIGURE 4.36: Total amplitude of vibration of the transverse displacement versus the non-linear natural frequency, when $V = 5$ volts.

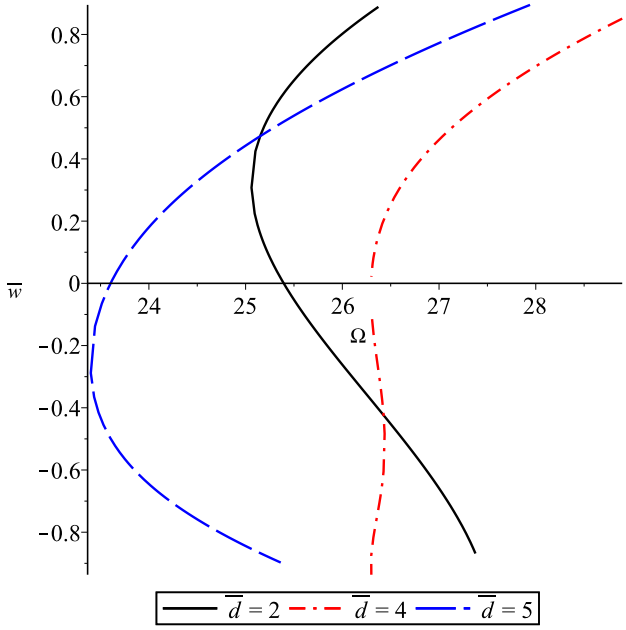

FIGURE 4.37: Total amplitude of vibration of the transverse displacement versus the non-linear natural frequency, when $V = 8$ volts.

Analysing now Figures 4.35 to 4.37, the influence of the gap size, which is here presented in a non dimension form $\bar{d} = d/h$, in system dynamics is evident.

In Figure 4.35, for an applied voltage of 3 volts, the case where the gap size is smaller is evidently going to suffer a stronger attraction force, consequently presenting a higher offset than the other 2 situations. In Figure 4.36, once again, the situation which presents a lower gap size presents a higher offset, and it also presents a region where no hardening or softening seem to prevail. In the other two situations, only hardening is verified. One can also see that a decrease in the gap size does not lead to a linear increase in the offset, as expected since the electrostatic force does not depend linearly on this parameter. Finally, in Figure 4.37, where the applied voltage is 8 volts , one can see three different behaviours of the same system, by just changing the gap size. When $\bar{d} = 5$, no softening behaviour is detected. When the gap is reduced to $\bar{d} = 4$, both softening and hardening effect are detected. In the last case, $\bar{d} = 2$, both effects are detected as well, but now the softening effect that occurs, is much more pronounced, and the hardening behaviour only takes place for higher values of $\bar{w}$. Still in this situation, one can see that no hardening effect takes place for negative values of the amplitude displacement, which may be due to the fact that the amplitude of the static deflection causes the beam to be close to the stationary electrode, and so the remaining distance is not sufficient to lead to considerable geometric non-linearities and lead to hardening. Another notable feature of figure 4.37 is the big differences in the natural frequencies, which are lower for higher values of the gap size.

4.3.3 FRINGING FIELD EFFECTS

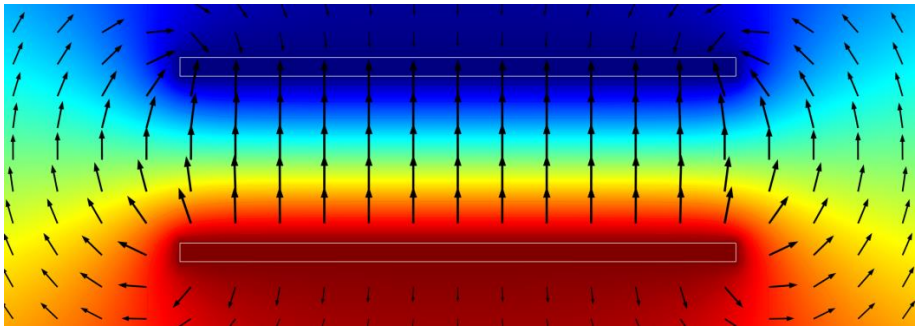

FIGURE 4.38: Representation of the electric field between two parallel plates, with the representation of fringed fields.

The electrostatic force is directly related to the existing capacitance between the beam and the static electrode. Ideally, this capacitance is proportional to the overlapped area of both plates/electrodes, where the electric field is uniform. However fringing electric fields (curved fields in Figure 4.38) exist in the edge of any two finite length parallel conducting plates, which add an additional capacitance that is not easy to quantify [56]. Since this fringe effect adds an additional capacitance, it will also enhance the electrostatic attraction force. In many electrostatic actuated MEMS and NEMS, that are fabricated by current micromachining processes, the nominal gap between the electrodes is not negligible relative to the lateral dimension of the deformable capacitor. Therefore, fringing fields are considerable and must be accounted for when modelling the electrostatic forces.

FRINGE EFFECT IN THE "PULL-IN" VOLTAGE

In this subsection, the fringing field effect in the "pull-in" voltage is going to be analysed. In the following analysis, the beam analysed by Krylov [19] is considered, which properties are presented in Table 3.11. This is a wide beam since its width is 10 times the thickness, therefore the fringing field effects are small. Analysing Figure 4.39, one can see that by considering the fringing fields, the predicted "pull-in" voltage is lower than if they were neglected. This is easily explained by the fact that for the same voltage, the fringing fields add an extra capacitance to the system, which in turn increases the electrostatic force. This way, considering the fringing field effects will always lead to lower "pull-in" voltage predictions.

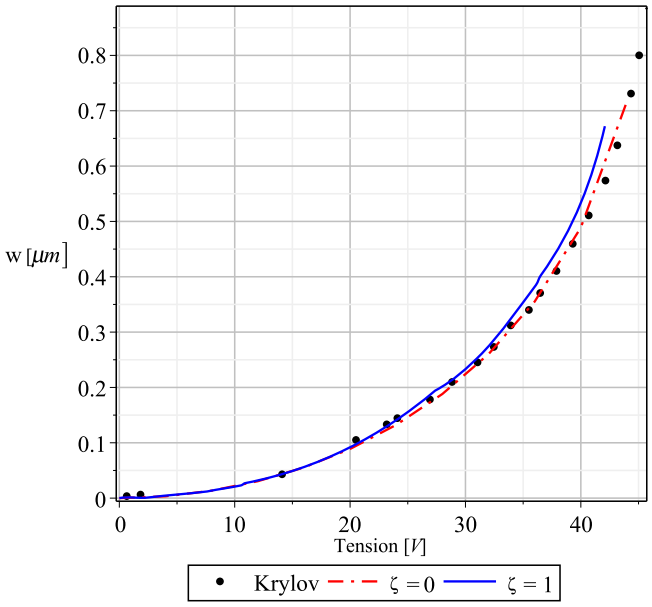

FIGURE 4.39: Fringe effect in the "pull-in" voltage of the beam considered by Krylov.

FRINGE EFFECT IN THE SYSTEM DYNAMICS

In order to see the influence of neglecting the fringe correction factor in Eq. (2.38), the backbone curves of Figures 4.7 and 4.8 are presented once again ($\zeta = 1$), this time comparing them to the case where the fringe field effect is neglected ($\zeta = 0$).

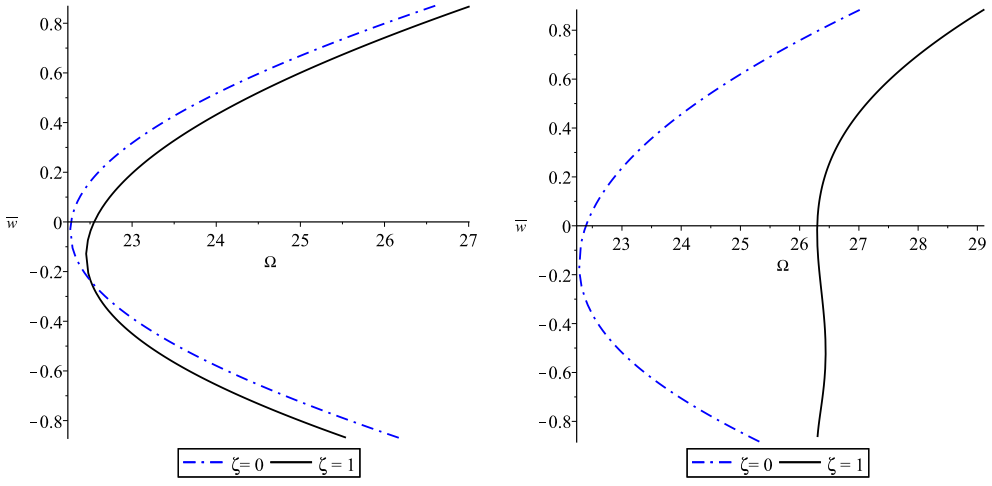

(a) $V = 5$ volts (b) $V = 10$ volts

FIGURE 4.40: Effect of neglecting the fringe effect in the backbone curve for $\bar{b} = 1$.

By analysing Figure 4.40, the error committed by neglecting the fringing effect is

evident. When $\zeta = 0$, the effective attraction force is lower, and due to this we can see in Figure 4.33 that the amplitude offset is lower. When the voltage applied increases to 10 volts, neglecting the fringe effect leads to a totally different dynamic behaviour. Instead of having softening effects, one only has hardening and the natural frequencies for the same amplitude of displacement are extremely different. The effect of neglecting the fringe effect is so evident in this beam configuration, due to the low width of the beam in relation to it's thickness and to the gap size, leading to strong fringing field effects.

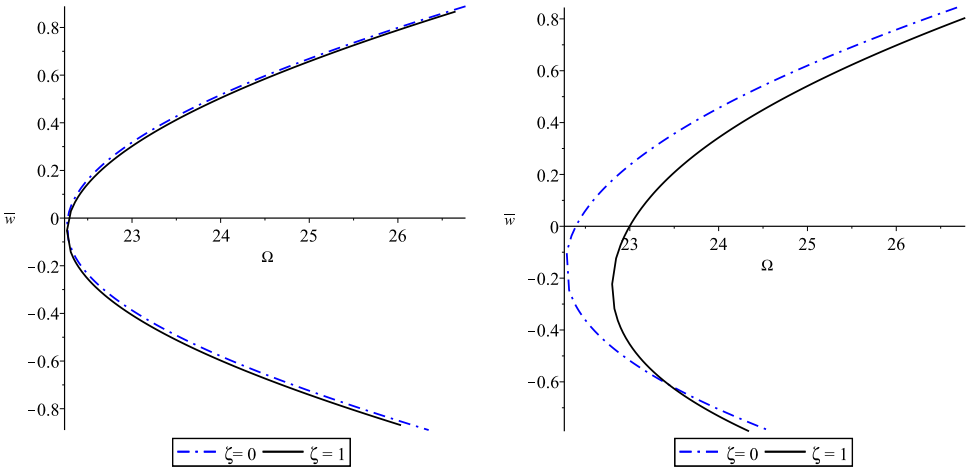

(a) $V = 5$ volts (b) $V = 10$ volts

FIGURE 4.41: Effect of neglecting the fringe effect in the backbone curve for $\bar{b} = 5$.

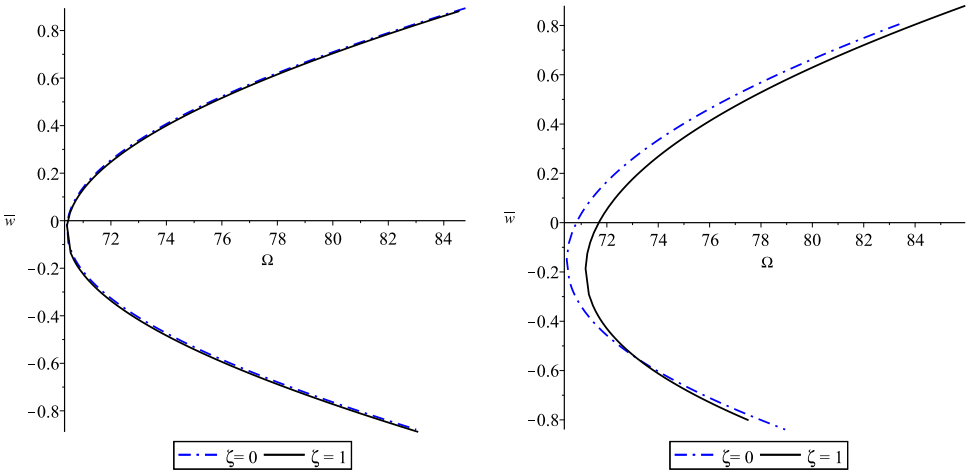

(a) $V = 5$ volts (b) $V = 10$ volts

FIGURE 4.42: Effect of neglecting the fringe effect in the backbone curve for $\bar{b} = 10$.

In Figures 4.41 and 4.42 the beams considered are increasingly wider, therefore, the

effects of the fringing fields are lower, and for 5 volts the differences are barely noticeable. However, when the voltage is raised to 10 volts, the enhancement of the electrostatic force due to the fringing fields leads to some noticeable differences in system's dynamic behaviour.

After these analysis, one can conclude that the fringing field effects can be neglected for wide beams, and when low voltages are applied in the system. For beams with small widths, these fringed fields contribute with an attraction force that cannot be neglected when compared to the attraction force generated by the uniform electric field that exists between the beam and the static electrode.

4.4 Bifurcation Analysis

In this section, bifurcation points and secondary branches are studied. The beam considered for this analysis has the elastic properties presented in Table 4.1 and the geometric properties of Table 4.2. One constant term and the first three harmonics are once again considered for this analysis, and the model uses 7 longitudinal shape functions (p_l) and 6 shape functions for the transverse and rotation displacements (p_o and p_t). The influence of the applied voltage and nonlocal effects on the bifurcation points detected will also be considered.

In this first analysis, no voltage is applied and no local effects are considered; the resulting system's backbone curve is presented in Figure 4.43. This backbone curve is not the same as the one presented in Figure 4.6, since in this case, the point considered is not at the centre of the beam but at $x = 0.25L$, and the amplitude of vibration range goes up to $\bar{w} = 2.5$ in order to detect bifurcation points and secondary branches. One bifurcation point was detected giving birth to a secondary branch, for both positive and negative vibration amplitudes. Analysing the bifurcation point detected for positive values of the vibration amplitude, it occurs for $\omega/\omega_1 = 1.73$ and $\bar{w} = 1.76$.

In the considered conditions ($V = 0$ volt and $\eta = 0$), the system is described by an equation of the Duffing type, therefore only the odd harmonics are present in the solutions of the main branch. The main branch of Figure 4.43, is related to the first and third harmonic, as seen before in Figure 4.9, and in order to see what occurs in the secondary branch, the amplitude of all harmonics are plotted in Figures 4.44 and 4.45.

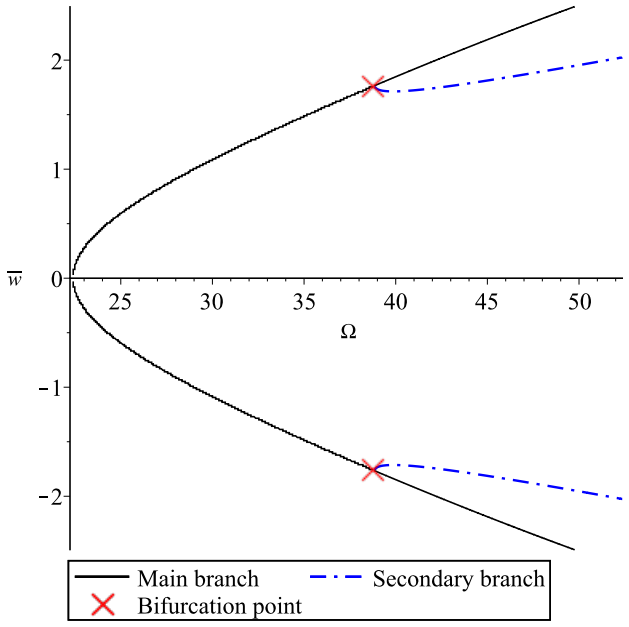

FIGURE 4.43: Main and Secondary branches of the backbone curve of a CC beam with no applied voltage and no nonlocal effects considered, for $x = 0.25L$.

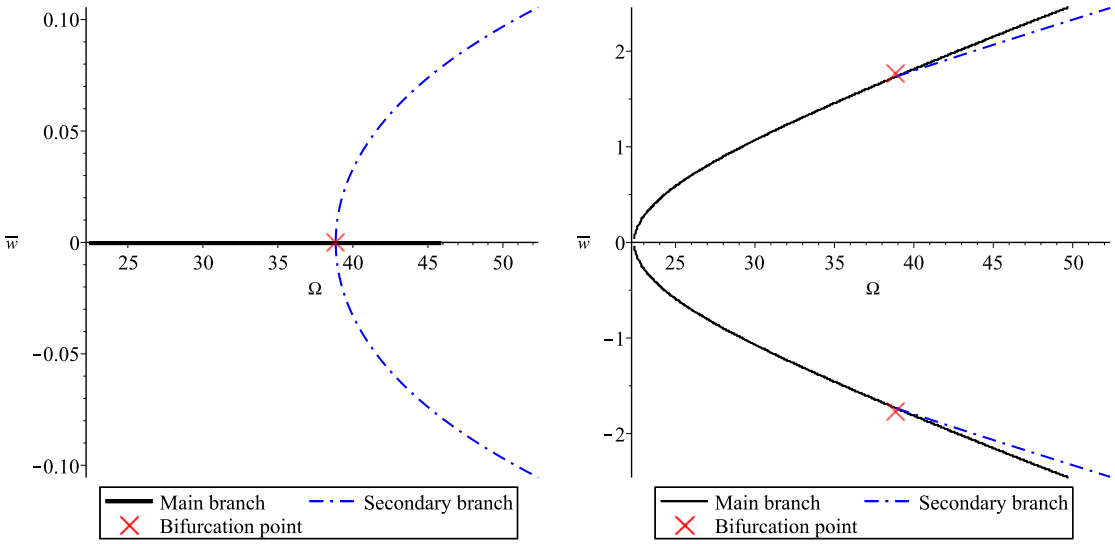

(a) constant term (b) 1^{st} harmonic

FIGURE 4.44: Main and secondary branches of the backbone curve of the constant term and the 1^{st} harmonic, for $x = 0.25L$.

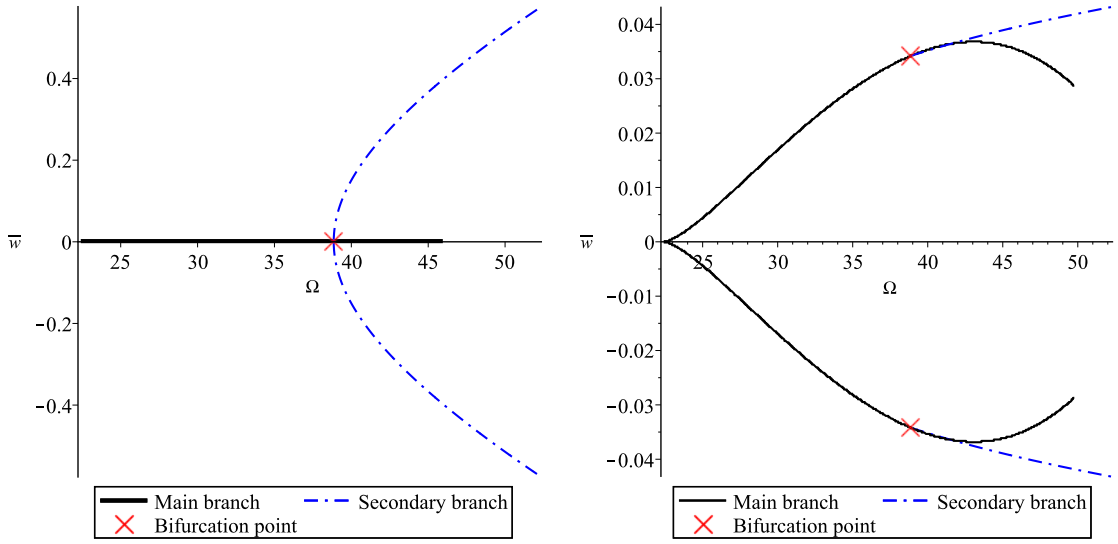

(a) 2^{nd} harmonic (b) 3^{rd} harmonic

FIGURE 4.45: Main and secondary branches of the backbone curve of the 2^{nd} harmonic. and the 3^{rd} harmonic, for $x = 0.25L$.

Analysing the evolution of the harmonics of the main branches, only the odd harmonics contribute to the total response of the beam. However, when analysing the secondary branches, one can see that the amplitude of the constant term and the second harmonic start to grow, and are not zero.

These results confirm that although the system is governed by an equation with only odd non-linearities, even harmonics can appear in the solution due to symmetry breaking bifurcations, like the one detected in this analysis. The secondary branches found by Lewandowski [27] and Ribeiro [29] connect two main branches, however, in this case the secondary branch, which is related to both odd and even harmonics, did not lead to another main branch. This fact was also reported by Stoykov and Ribeiro [30].

To understand which modes are interacting in the secondary branch, the shape of each harmonic is plotted for four different points along the secondary branch presented in Figure 4.43, where ω_{bif} corresponds to the frequency at which the bifurcation point occurs. Analysing the shapes of each harmonic, one can see that the constant term and the second harmonic assume the second mode shape of vibration, the first harmonic is related to the first mode shape and finally the third harmonic presents the third mode shape. The shape of the harmonics are not shown in a non-dimensional form, allowing one to see that when the shapes are plotted for a frequency very close to the bifurcation one ($\omega/\omega_{bif} = 1.01$), the constant term and the second harmonic are almost non-existent. As the frequency is increased, the amplitude of the constant term and the second harmonic increase as well.

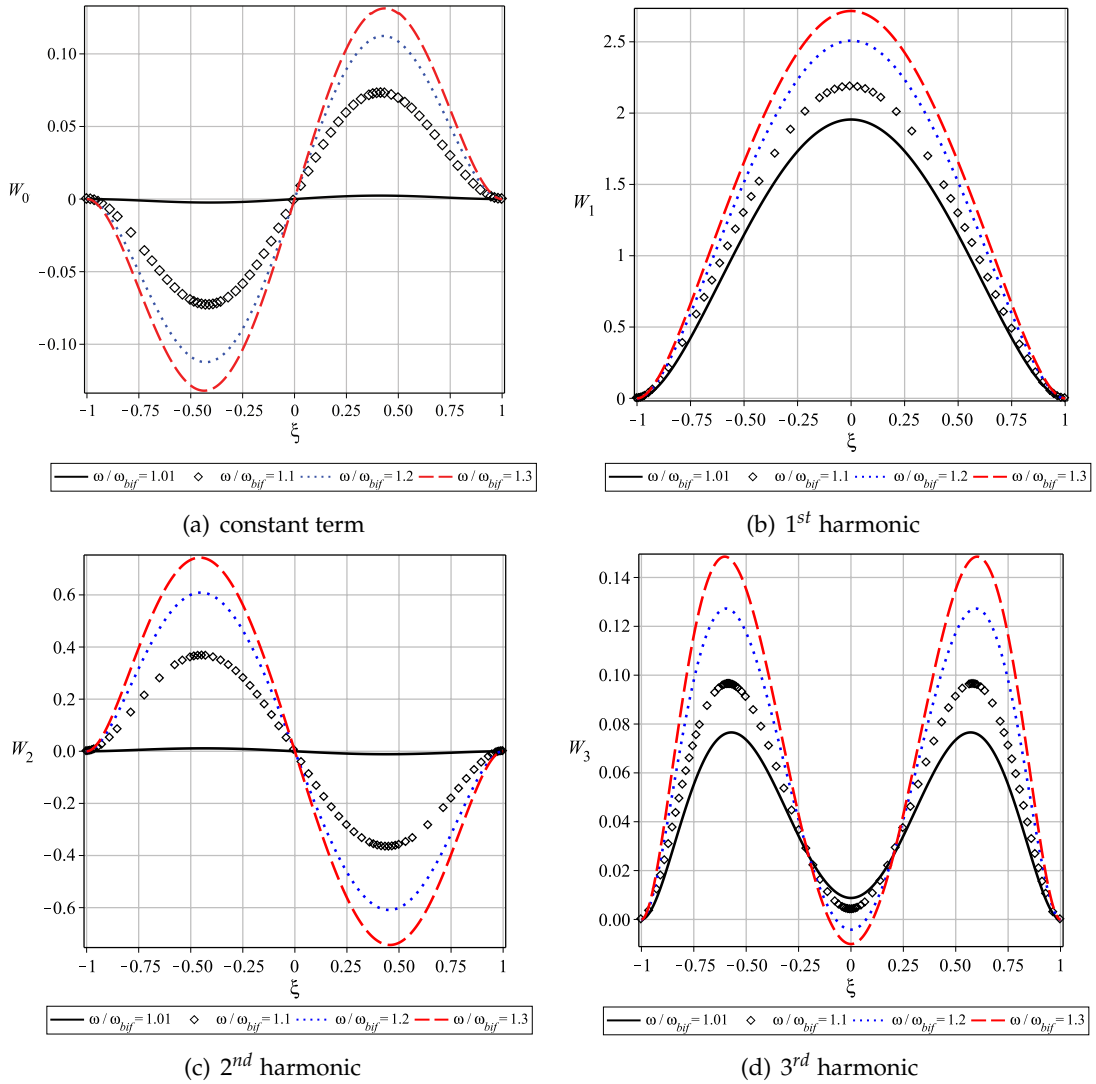

(a) constant term

(b) 1^{st} harmonic

(c) 2^{nd} harmonic

(d) 3^{rd} harmonic

FIGURE 4.46: Shape of the constant term and the three harmonics for different points along the secondary branch, considering V=0 volt and $\eta = 0$.

In Figure 4.47, the shape of the beam along half a period of vibration is presented, when $\omega/\omega_{bif} = 1.2$. A 1:2 internal resonance is detected, where the first and second harmonics interact with each other, leading to energy exchanges between the first and second mode. The third harmonic also has some influence in the general response of the beam, as one can see by analysing the amplitudes of this harmonic (Figures 4.45b and 4.46d), although the third mode shape associated to this harmonic is not clearly visible in the overall beam shape presented in Figure 4.47. During one vibration cycle, the shape of the beam clearly changes from the first mode to the second mode, as the energy exchanges from one mode to the other.

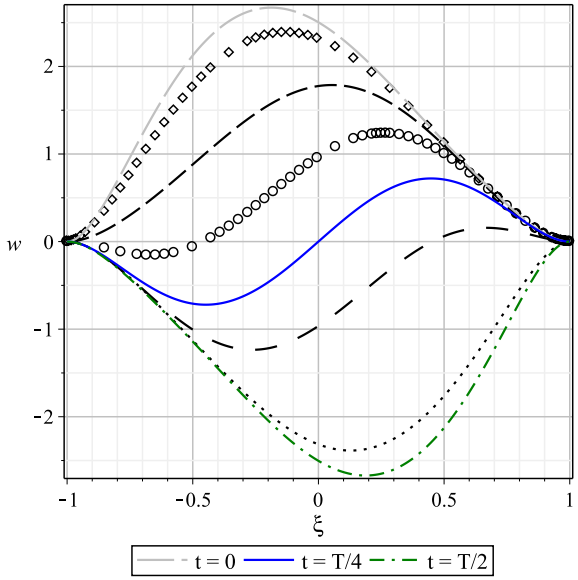

FIGURE 4.47: Shape of the beam along half a period of vibration, when ω/ω_{bif} = 1.2, $V = 0$ volt, and $\eta = 0$.

In Table 4.3 some relevant frequency ratios are presented, to understand the influence of the applied voltage and the nonlocal effects on the bifurcation point detected. Analysing the influence of the nonlocal effects on the frequency ratio at which the bifurcation point occurs (ω_{bif}/ω), one can see that for both values of η, this frequency ratio remains unchanged. When voltage is considered, this frequency ratio decreases, which means that the bifurcation point occurs for frequencies closer to the fundamental natural frequency. For all cases presented in Table 4.3, the bifurcation point detected is related to a 1:2 internal resonance, however, analysing the ratio ω_2/ω_{bif} for the cases where $V = 0$ volt, this value would be expected to be closer to 2, in order to justify the detected internal resonance. This could probably be explained by the fact that ω_2 (used to obtain the ratio in Table 4.3) was calculated for the static deflection of the beam, and not for the amplitude of vibration at which the bifurcation occurred. This way, it would be expected that if the second natural frequency was calculated at the amplitude of vibration at which the bifurcation occurs, due to geometric non-linearities, the frequency ratio ω_2/ω_{bif} would be much closer to 2, which would explain the 1:2 internal resonance.

In Figure 4.48, the backbone curves of the cases analysed in Table 4.3, which were calculated for a point at the centre of the beam ($x = 0$), are presented.

TABLE 4.3: Frequency relation for the bifurcation analysis, for different values of the applied voltage and the nonlocal parameter.

	$V = 0$ volt, $\eta = 0$	$V = 10$ volts, $\eta = 0$	$V = 0$ volt, $\eta = 0.2$	$V = 10$ volts , $\eta = 0.2$
ω_{bif}/ω_1	1.73	1.49	1.73	1.49
ω_2/ω_{bif}	1.58	1.96	1.60	1.82
ω_3/ω_{bif}	3.08	3.84	3.24	3.75

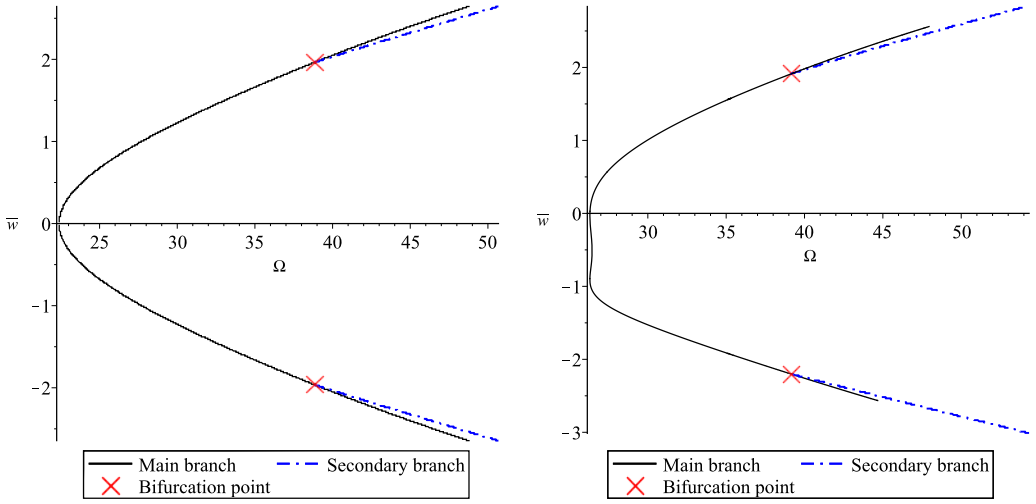

(a) $V = 0, \eta = 0$ (b) $V = 10, \eta = 0$

(c) $V = 0, \eta = 0.2$ (d) $V = 10, \eta = 0.2$

FIGURE 4.48: Main and secondary branches of the backbone curve of a CC beam for a point at the centre of the beam ($x = 0$), considering different values of V and η.

Combining the information of Table 4.3 with Figure 4.48, on can see that the nonlocal parameter does not affect neither the frequency ratio nor the amplitude of vibration at which the bifurcation occurs. The applied voltage introduces an asymmetric behaviour of the system, however, although the bifurcation points occur for different values of amplitude, the correspondent frequency ratio is the same.

Is important to refer that for all the presented cases, the bifurcation points detected are symmetry breaking bifurcations. This is clear for the cases where the applied voltage is $V = 0$ volt, since the even harmonics have no influence in the main branch's solutions, but appear in the secondary branches. However, when $V = 10$ volts the equation of motion which describes the system, contains even non-linearities, meaning that even harmonics affect the solutions of the main branches, and still this bifurcation is considered a symmetry breaking one. To understand why this point is still a symmetry breaking bifurcation, and considering the case where $V = 10$ and $\eta = 0$, the shape of the second harmonic is plotted for a solution in the main branch just before the frequency at which the bifurcation occurs ($\omega/\omega_{bif} = 0.9$), and for a solution in the secondary branch where $\omega/\omega_{bif} = 1.1$.

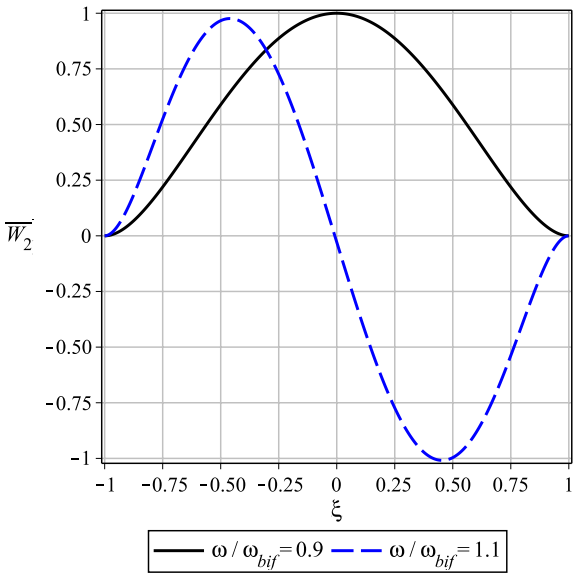

FIGURE 4.49: Shape of the second harmonic for $\omega/\omega_{bif} = 0.9$ and $\omega/\omega_{bif} = 1.1$.

In Figure 4.49, one can see that for the solution in the main branch, the second harmonic assumes the first mode shape which is symmetric, however, for the solution in the secondary branch the second harmonic presents the shape of the second mode which is antisymmetric. In the main branch, only symmetric modes prevail, and in the secondary branch, the odd harmonics assume symmetric mode shapes (just like in the main branch), while the odd harmonics present antisymmetric mode shapes. Due to this evidence, the bifurcation is considered a symmetry breaking bifurcation.

4.5 Natural Frequencies and Mode Shapes of a Simply Supported Nanobeam Under a DC Electrostatic Force

In the previous section, the dynamic behaviour of a double clamped beam under a DC electrostatic force was studied. In this section, the boundary condition considered will be simply supported. In a first approach, the influence of the type of boundary condition in the spring hardening effect will be analysed. This way, both boundary conditions analysed in this dissertation will be compared, (CC and SS).

The beam considered has the geometric properties presented in Table 4.2 and the elastic properties presented in Table 4.1. No electrostatic force will be considered, in order to see the influence of the geometric non-linearity only.

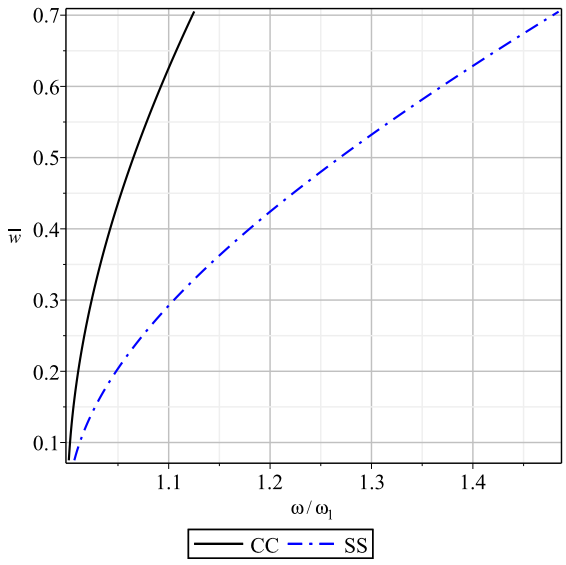

FIGURE 4.50: Comparison of the hardening spring effect for both type of boundary conditions, simply supported (SS) and double clamped (CC).

Analysing Figure 4.50, one can see the evolution of the backbone curve for a SS and CC beam. The frequencies are presented in a non-dimension form, and not in their absolute values, which means that although the natural frequencies of both beams are different, they start at the same point in the representation above. This way one can analyse the hardening rate of both boundary conditions, and conclude that the SS beam is submitted to an higher hardening than the CC beam.

This evidence is somehow counter intuitive, since the double clamped beam has a higher stiffness and one would expect it to have also a higher hardening effect. However, the higher stiffness only leads to a higher linear natural frequency. The simply supported

beam seems to present higher non-linear stiffness terms than the double clamped beam, which in turn lead to a more pronounced hardening. The probable physical explanation to this difference may lie in the moments that appear in the fixed ends of a double clamped beam. As the beam deflection increases these moments also increase, and at the same time, the geometric non-linearity leads to an axial tension. The moments generated in the fixed ends will contribute to reduce the axial tension, and consequently reduce the hardening rate. Since a simply supported boundary condition allows the rotation of the transverse section of the beam, no moments are generated, which could then explain the higher hardening rate that is verified in this situation.

For the simply supported beam, a simpler analysis was carried out, where only the backbone curves and the first and second symmetric modes are analysed. In all situations the voltage considered was 5 volts, and no nonlocal effects were took into account.

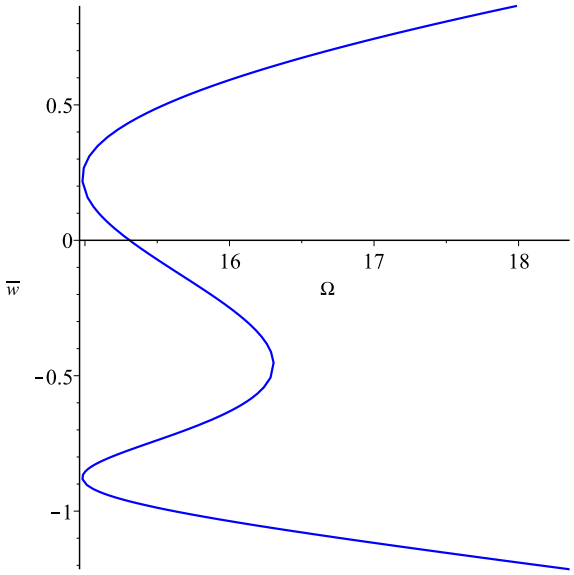

FIGURE 4.51: Backbone curve for the 1^{st} natural frequency of the SS beam when $V = 5$ volts.

In Figure 4.51 the evolution of the first natural frequency of the SS beam is presented in a backbone curve. In opposition to what occurred in the CC boundary condition for the same applied voltage (Figure 4.7), in the simply supported case one can find both spring hardening and softening effect. Since the SS beam has higher static deflection, it will present a strong initial axial tension. When vibrates at low amplitude values, the reduction of the axial in the overall oscillation motion leads to a softening behaviour. However, when the amplitudes of vibration are increased, geometric non-linearities start to become more evident and softening gives place to hardening.

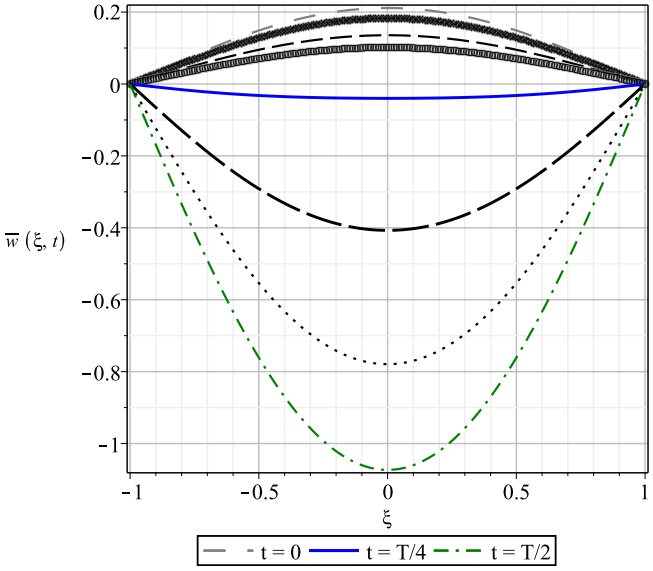

FIGURE 4.52: 1^{st}mode shape of the SS beam when $V = 5$ volts.

The shape of the beam vibrating at its first mode is presented in Figure 4.52 for different instants along half a period of vibration, when $\bar{w} = 0.2$.

The analysis carried out for the first natural frequency is now performed for the third one, and the second symmetric mode shape (third mode shape) is presented.

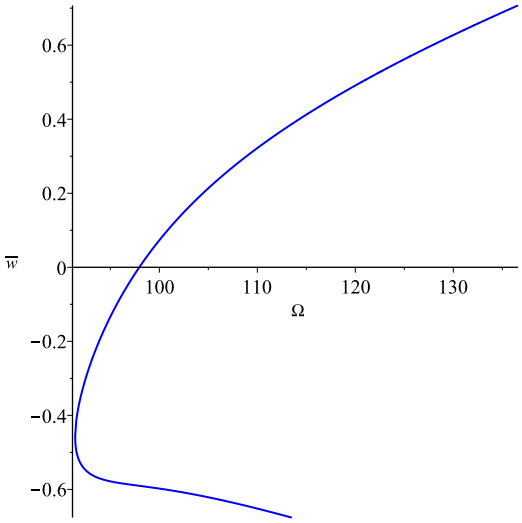

FIGURE 4.53: Backbone curve for the 3^{rd} natural frequency of the SS beam when $V = 5$ volts.

The backbone curve of Figure 4.53 shows that for the third natural frequency only spring hardening is detected, however, the rate of hardening is much more pronounced for amplitudes lower than the static deflection of the beam, than for higher values. No

internal resonance was found in this situation, and for $\bar{\omega} = 0.2$, the shape of the beam vibrating in its second symmetric mode is presented in the following figure, for half is period of vibration.

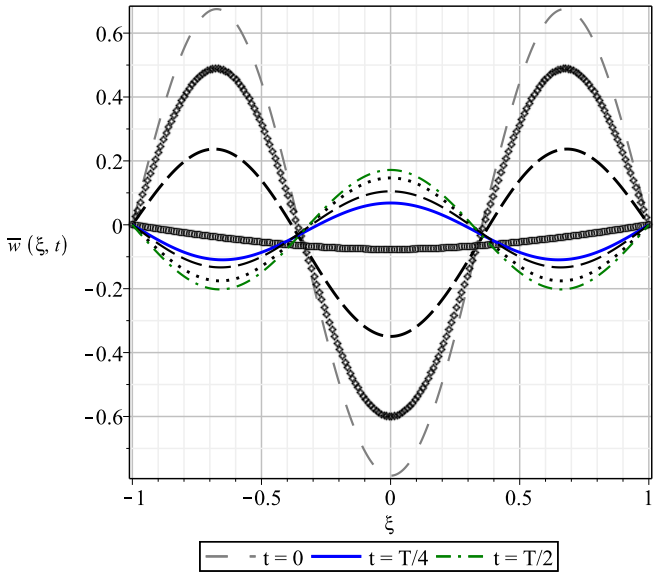

FIGURE 4.54: 2^{nd} symmetric mode shape of the SS beam when $V = 5$ volts.

4.6 CONCLUSION

In this chapter, an extensive analysis of the static and dynamic behaviour of an electrostatically actuated nanobeam took place. The static deflection is highly dependent on the voltage applied and on the nonlocal parameter, and higher deflections occur for higher values of both parameters. A dynamical analysis was made for both type of boundary conditions considered in this dissertation, where both hardening and softening effect were found, depending on the applied voltage. The influence of the beam's width and the gap distance in the dynamical behaviour of the beam was analysed, as well as the effect of fringing fields. Furthermore, symmetry breaking bifurcations were detected, which led to secondary branches, where 1:2 internal resonances were detected. The bifurcations detected were not affected by nonlocal effects, however, when the applied voltage was considered, the bifurcation point took place for lower frequency ratios.

CHAPTER 5

MOLECULAR DYNAMICS

5.1 INTRODUCTION

Molecular Dynamics (MD) is a computational method that calculates the time dependent behaviour of an atomic/molecular system. It describes the motion of all atoms as well as the interactions that occur among them, which governs the microscopic behaviour of physical systems. There are two main families of MD methods, which differ according to the model chosen to represent the system. The classical mechanics approach to MD simulations, considers the atoms as point masses connected by springs, which represent the role of the chemical bonds. This approach gives a perspective of the dynamical evolution of a system, describing the trajectories of each atom and molecules that are determined by numerically solving Newton's equation of motion. The second approach is the quantum or *ab initio* (first principles) MD simulations, which take into account the quantum nature of the chemical bonds. The electron density function for the valence electrons, which determines the bonding of the atoms existing in the system, is computed by solving quantum equations, while the dynamics of the nuclei and inner atoms are modelled by classical approaches [57]. In this chapter the classical mechanics approach to MD simulations will be considered, and will simply be referred to as MD.

MD simulations are intensively used in the area of Biology and Chemistry, where the structure, dynamics and thermodynamics of biological molecules are investigated [57,58] Since MD simulations are able to describe the trajectory of each atom, it has been used to study the elastic properties and dynamical behaviour of carbon nanotubes [6,7,59,60].

Despite the great potential that MD simulations present to study the dynamical behaviour of molecular and atomic systems, they require very high computational resources, which limits the common application of these simulations to fairly simple systems. Another factor that leads to high computational time is the size of the

integration time steps required. Typical MD simulations have time steps in the order of 1 femtosecond (10^{-15} s), and due to this, the simulations can only run up to nanoseconds (10^{-9} s) or a few microseconds (10^{-6} s). These limitations show the importance of developing continuum models, like the one presented in this dissertation, that are able to accurately describe the dynamical behaviour of nano-scaled systems with considerable lower computational resources.

5.2 Atomic Force Field Model of Molecular Systems

Since the problems that MD simulations solve involve many atoms, using a quantum mechanics approach leads to huge computational costs. In order to overcome this problem, empirical potential energy functions or atomic force field models have been developed, and are much less computationally demanding. In this section a small overview of one typical atomic force field model used to describe atomic/molecular systems is presented [57,58].

The interaction law that describes the chemical bond between atoms is specified by the potential energy V which is a function of the positions $\boldsymbol{r}_i$ of the interacting atoms. The force $\boldsymbol{F}_i$ applied on the *i-th* atom can be expressed as the gradient of the potential V, as shown in the following equation.

$$\boldsymbol{F}_i = -\nabla_i V = -\Big(\frac{\partial V}{\partial x_i}, \frac{\partial V}{\partial y_i}, \frac{\partial V}{\partial z_i}\Big) \tag{5.1}$$

A typical potential energy considered in the simulation of atomic/molecular systems, is calculated as a sum of the bonded terms (E_{bonded}) which describes the bonds, angles and bond rotations in a molecular structure, and a sum of the non-bonded terms ($E_{non-bonded}$), which account for the interactions between non bonded atoms.

$$V = E_{bonded} + E_{non-bonded} \tag{5.2}$$

$$E_{bonded} = E_{bond-stretch} + E_{angle-bend} + E_{rotate-bond} \tag{5.3}$$

Physically, the terms $E_{bond-stretch}$ and $E_{angle-bend}$ of Eq. (5.3) describe energies of deformations of bond lengths and bond angles from a specific equilibrium values. The term $E_{rotate-bond}$ is a periodic energy term which describes the rotations around the chemical bond.

$$E_{non-bonded} = E_{vdW} + E_{electrostatic} \tag{5.4}$$

In Eq. (5.4) the term E_{vdW} represents the van de Waals repulsive and attractive interatomic forces and the term $E_{eletrostatic}$ represents the Coulomb electrostatic potential.

5.3 General Overview of the MD Algorithm

The MD algorithm, which is well described in [58], is based on solving Newton's equation of motion of each individual atom,

$$\boldsymbol{F}_i = m_i \frac{\boldsymbol{r}_i}{dt^2} \tag{5.5}$$

where m_i represents the mass of the *i-th* atom and $\boldsymbol{r}_i$ represents its position. Knowing the initial positions and velocities of the atoms, one can integrate Eq. (5.5) and derive the trajectory of each particle, describing the position, velocity and acceleration as they change with time. This method is deterministic since the position and velocity of each atom can be calculated and the state of the system can be predicted at any time instant. Combining Eq. (5.5) and (5.1), one can relate the derivative of the potential V, to the changes in position r_i as a function of time.

$$-\frac{dV}{d\boldsymbol{r}_i} = m_i \frac{d^2\boldsymbol{r}_i}{dt^2} \tag{5.6}$$

The equations of motion for each atom can be derived from Eq. (5.5), and the position and the velocity can be expressed as follows,

$$\boldsymbol{v}_i = \boldsymbol{a}_i t + \boldsymbol{v}_{i0} \tag{5.7a}$$

$$\boldsymbol{x}_i = \frac{\boldsymbol{a}_i t^2}{2} + \boldsymbol{v}_{i0} t + \boldsymbol{x}_{i0} \tag{5.7b}$$

Since MD simulations require very small integration time steps, considering a constant acceleration during one time step is a reasonable assumption. The initial position of each atom can be determined by experimental observation with different x-ray or electron microscopy techniques [58].

After defining the initial position of all atoms, their initial acceleration can be determined as follows,

$$\boldsymbol{a}_i = -\frac{1}{m_i}\frac{dV}{d\boldsymbol{r}_i} \tag{5.8}$$

Knowing the initial velocity distribution is not so straightforward. However, if the system is in thermal equilibrium at temperature T, the initial velocity distribution is taken to be the Maxwell-Boltzmann distribution, which represents the probability of a certain atom having the velocity v. As an example, the velocity distribution of Hydrogen atoms for two different temperatures are presented in Figure 5.1.

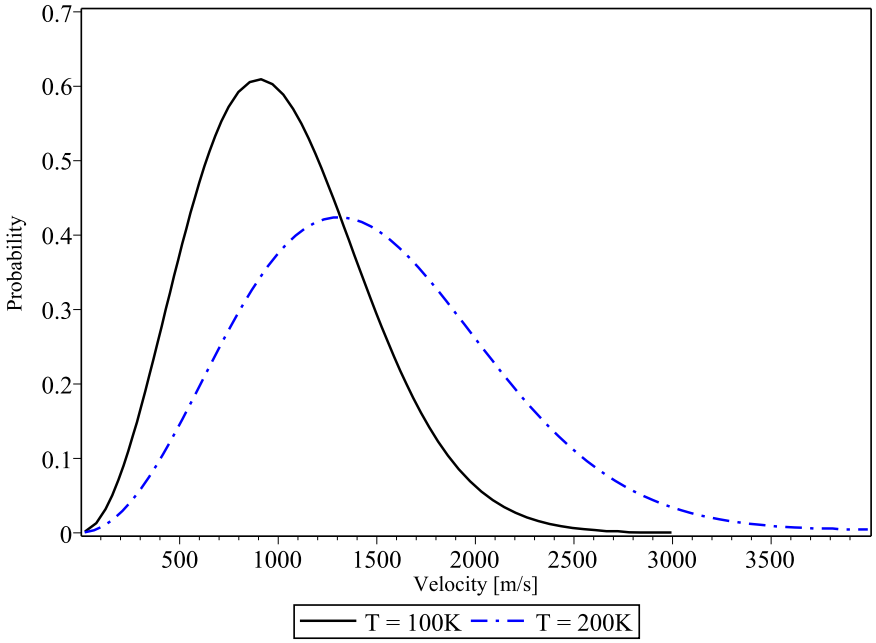

FIGURE 5.1: Maxwell-Boltzmann velocity distribution of Oxygen atoms at 300 K.

The initial velocity of each individual atom in the simulation domain is randomly chosen according to its Maxwell-Boltzmann distribution function.

The models that define the potential energy of a atomic/molecular system, are a function of the position of all existing atoms, and consequently, the potential energy has a complicated nature which leads to equations of motion with no analytical solution. Due to this complexity, the equations must be solved numerically and many algorithms have been developed for that purpose, such as the Verlet or the leap-frog algorithms [57, 58].

A simplified description of the MD simulation algorithm is presented in Figure 5.2, where one can see the sequence of the main steps.

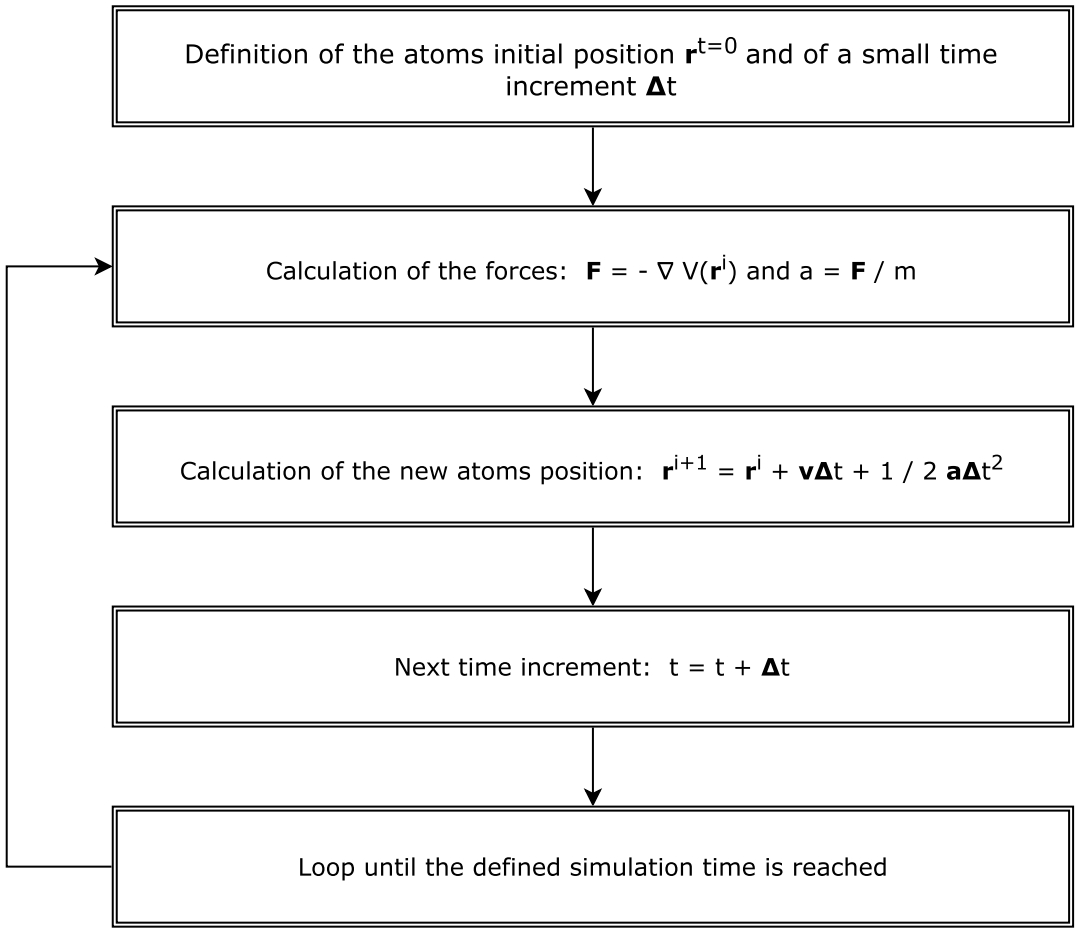

FIGURE 5.2: Block diagram of the MD algorithm.

5.4 CARBON NANOTUBES

Carbon nanotubes (CNT) are cylindrical hollow tubes formed by carbon atoms that present highly attractive properties for a variety of fields due to their excellent mechanical and electronic properties. Their good electrical and thermal conductivity, high stiffness and strength combined with low density, make CNTs a highly attractive building element for NEMS devices. One promising application of these structures in NEMS, is the CNT based ultrasensitive sensor. CNTs are stable in harsh chemical environments, and respond to external actuations rapidly and with high sensitivity [59]. With this stated, it is of great significance to fully understand their vibration properties.

CNTs can be separated in single walled nanotubes (SWCNT) and in multi walled nanotubes (MWCNT), depending on the number of atoms they have along its thickness. A SWCNT if formed by rolling a one-atom thick graphene sheet, and the way this rolling

process is done, will determine the chirality of the nanotube. The chirality is represented by a pair of indices (n,m) which separate the nanotubes in zigzag (n,0), armchair (n,n) and chiral (n,m).

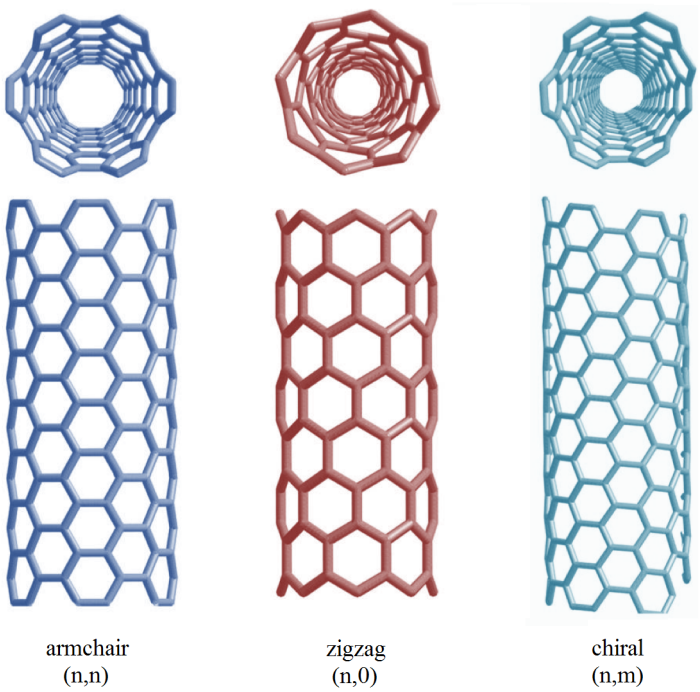

FIGURE 5.3: Different types of chirality in a CNT.

5.5 MD SIMULATIONS

In this section some MD simulations are presented in order to calculate the Young's modulus of a certain carbon nanotube, and to calculate the natural frequencies which will then be compared to the ones obtained with the continuum nonlocal model presented in this dissertation. All simulations were carried out with the Atomistix ToolKit (ATK) software developed by Quantum Wise [61].

The Young's modulus of CNTs has been a subject of considerable interest. The determination of this elastic property has been done experimentally and with MD simulations. Treacy et al. [62], carried out some experimental work to determine the Young's modulus of clamped-free CNTs, using electric or thermal excitation, and measuring the vibrations in a transmission electron microscope. Using the frequency equation derived from the Euler-Bernoulli beam theory, the authors derived the Young's modulus in a reverse manner.

The computation of the Young's Modulus can also be done using MD simulations, and values in the order of 1 TPa have been reported [33, 60]. This value range is in good agreement with the experimental results reported by [62].

In the following analysis, an armchair (5,5) CNT was considered. In order to calculate the Young's modulus of this structure, the CNT was strained in an incrementation process. During each increment, the applied force is registered and converted to a strain value by knowing the geometry of the CNT. Furthermore, after each strain increment the configuration of the atoms were brought to the equilibrium via an appropriate energy minimisation, to assure stability in the process. This way, the resulting Young's modulus calculated was 1.1325 TPa, and the derived stress-strain curve is presented in Figure 5.4.

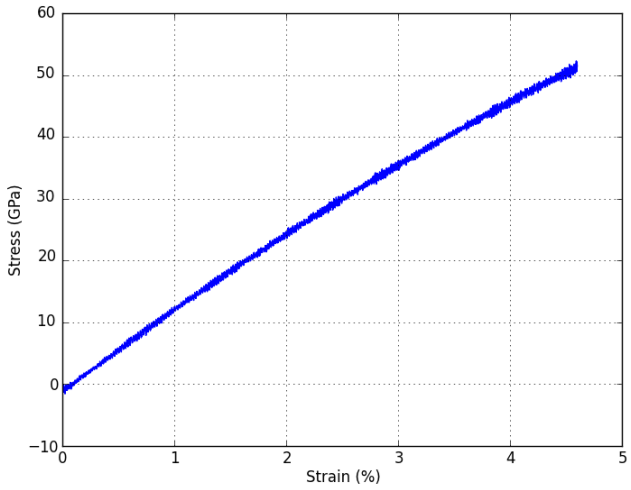

FIGURE 5.4: Stress-Strain curve of a CNT.

The value calculated with this MD simulation is in good agreement with the values calculated by other authors [5, 33, 60].

In the next MD simulation presented, the natural frequencies, of the same CNT considered before, were calculated and compared to the ones derived by the *p*-version model presented in previous chapters.

The natural frequencies were computed by solving the well known equation of motion,

$$\mathbf{M}\ddot{\mathbf{q}} + \mathbf{K}\mathbf{q} = \mathbf{0} \tag{5.9}$$

where $\mathbf{M}$ is the mass matrix, $\mathbf{K}$ the stiffness or Hessian matrix and $\mathbf{q}$ the vector of generalized displacements. The mass matrix is easy to calculate, on the other hand, the

stiffness matrix is more cumbersome to derive. The ATK software calculates each term of the stiffness matrix $D_{\mu\alpha,i\beta}$, by the following equation [61],

$$D_{\mu\alpha,i\beta} = \frac{dF_{i\beta}}{dr_{\mu\alpha}} \tag{5.10}$$

where $F_{i\beta}$ is the force on atom i in the direction β due to a displacement $r_{\mu\alpha}$ of atom μ in the direction α. The derivative is calculated by finite differences.

All terms of the stiffness matrix are calculated for each time step of the simulation, and at the end, the values are averaged out resulting in what can be called a "time averaged stiffness matrix". This way, in order to compute the natural frequencies and modes, one just needs to solve the eigenvalue problem,

$$\mathbf{K}\boldsymbol{\varphi}_i = \lambda_i \mathbf{M}\boldsymbol{\varphi}_i \tag{5.11}$$

were λ_i is te *i-th* eigenvalue, which represents the square of the natural frequency, and $\boldsymbol{\varphi}_i$ is the corresponding eigenvector (natural mode).

In order to validate this MD simulation, and to assure that the correct set-up and energy potentials were considered, the first natural frequency of the double clamped armchair (5,5) CNT was calculated and compared with the one presented by Hu [63], in Table 5.1.

TABLE 5.1: First natural frequency of an armchair (5,5) CNT.

L [nm]	MD [THz]	Hu [63] [THz]
4.12	0.65286	0.6600

Its important to refer that since MD simulations give a complete description of the trajectory of all atoms that define a molecular structure, one can derive the natural frequencies corresponding to all types of modes, such as flexural modes, torsional modes, shell modes and even breathing modes [6].

Analysing Table 5.2, the first two natural frequencies computed appear repeated, and are related to the flexural modes about the two different axis that are perpendicular to the axis of the CNT. The fifth mode is a torsional mode, and this way it does not appear repeated. The sixth and the seventh mode are flexural modes, and their value should appear repeated, however, due to asymmetries introduced by numeric issues, the values are slightly different. The shell and breathing modes are highly energetic modes, and do not appear in the above table.

As stated before, continuum models are good alternatives to describe the dynamics of nano structures, like CNTs, and it would be interesting to compare the results derived with the MD simulation with the ones calculated with the *p*-version continuum model

TABLE 5.2: First seven natural frequencies of a double clamped armchair (5,5) CNT computed with a MD simulation.

Mode	[THz]
ω_1 - flexural mode	0.6529
ω_2 - flexural mode	0.6529
ω_3 - flexural mode	1.5233
ω_4 - flexural mode	1.5233
ω_5 - torsional mode	1.6370
ω_6 - flexural mode	1.8594
ω_7 - flexural mode	1.8643

presented in previous chapters. To obtain accurate results with the continuum model, one first needs to know the correct value of the nonlocal parameter. Wang [12] deduced that the this parameter should be inferior to 2 nm, and Yang [33] also reported values between 0 and 2 nm.

Considering the aforementioned estimates of the nonlocal parameter , and comparing the results calculated with the continuum model with the ones derived with MD simulations, the nonlocal parameter that presented smaller relative errors was $\mu = 1.75$ nm . In Table 5.3 and in Figure 5.5, the first linear natural frequency for a armchair (5,5) CNT with different lengths, computed with both MD simulations and with the continuum model, is presented. For the p-version model, the number of shape functions used were $p_o = p_t = 15$. The relative errors between both methods are also presented.

TABLE 5.3: First linear natural frequency of an armchair (5,5) CNT computed with MD simulations and with a p-version continuum model.

L [nm]	MD [THz]	p-version model [THz]	Relative Error (%)
4.12	0.65286	0.66509	1.87
5.0	0.55856	0.54932	1.65
6.0	0.44733	0.44515	0.48
7.0	0.36754	0.36440	0.85
8.0	0.30467	0.30181	0.94
10.0	0.21037	0.21405	1.75

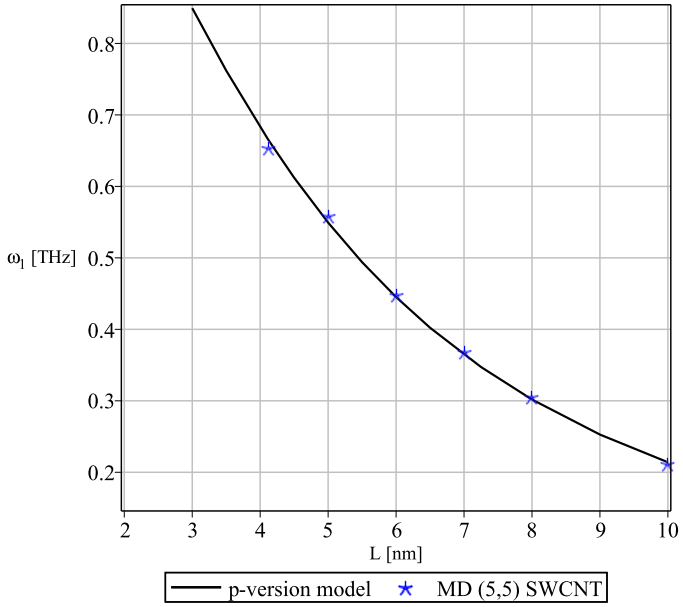

FIGURE 5.5: Evolution of the first linear natural frequency of an armchair (5,5) CNT with its length, computed with MD simulations and with the p-version continuum model

The p-version model produces extremely accurate results when compared to the ones derived with MD simulations. The nonlocal parameter that assured this accuracy is also in the range of values recommended in the literature. Hence, the advantage of using continuum models becomes extremely clear, since one can obtain correct results with much less computational effort.

Although the developed p-version model obtained accurate results, the success of these continuum approaches in modelling the vibrations of CNTs is highly dependent on the values of the non-local parameter, on the Young's modulus and even in the considered geometric properties of these structures. Regarding the nonlocal parameter, Duan et al. [7] have attempted to calibrate the nonlocal parameter for different CNTs, and found that this parameter is dependent on the boundary conditions and on the relation between the length and the diameter (L/d). The authors state that the nonlocal parameter decreases as the ratio L/d increases, and that this evolution is different depending on the type of boundary condition. Zhang et al. [59] analysed the influence of the chirality on the vibration of CNTs, and found that the first natural frequency is insensitive to changes in the chirality, and the higher natural frequencies are gradually more affected by this parameter.

Another subject that is a matter of discussion is the CNT effective thickness. Conventionally, the spacing between graphite layers is taken as the CNT thickness, which value is $0.34nm$, however some atomistic simulations presented in the literature [64, 65] have reported thickness values ranging from 0.066 to $0.34nm$. Huang et al [65] developed

an analytical approach to explain the ambiguity of the thickness value. The authors found that the thickness and the Young's modulus depend on the loading type, on the nanotube chirality and radius, and in the interatomic potential, which explains why the thickness values obtained by different authors are scattered, since most of them do not account for such effects.

Further investigations have to be carried out in order to accurately define the correct parameters of CNTs used in continuum models in order for them to fully take advantage of their potentialities and present themselves as true alternatives to atomistic models.

5.6 Conclusion

In this chapter, a general overview of the MD methodology and algorithm was presented. As a first principle approach, MD simulations are capable of modelling an atomic/molecular system with very high accuracy. When these type of simulations are used to study vibrations of nanotubes, one can obtain the entire dynamical behaviour of these structures, which is not possible with most continuum models. Despite this advantage, MD models demand high computation resources, which limits their application to very short timed simulations and to simple atomic/molecular structures.

The continuum model presented in this dissertation is an alternative to these expensive type of simulations. However, the success of the continuum models in accurately modelling vibrations of CNTs, is dependent on the correct Young's modulus of the structure, in the nonlocal parameter considered and on the correct effective tube thickness. The correct value of the nonlocal parameter is still a matter of intensive study, and an attempt was made to adjust this parameter of a armchair (5,5) CNT by comparing the results derived with the continuum model with the ones calculated with MD.

CHAPTER 6

CONCLUSIONS

6.1 SUMMARY

In this Thesis, a *p*-version of the finite element method based in the Timoshenko beam theory and in Erigen's nonlocal elasticity theory was developed to study the non-linear static and dynamic behaviour of electrostatically actuated nanobeams. The non-linearities considered in the model are due to the large vibration displacements which lead to geometric non-linearities, and due to the inherent non-linearity of the external electrostatic force. The non-linear equations of motion were solved by the harmonic balance method combined with an arc-length based continuation method, and several harmonics were considered in the Fourier expansion of the periodic solution of the equations of motion.

All the different terms of the developed *p*-version model were validated by comparing the derived results with those found in the literature, and turned out to by very accurate. In the analysis of the linear vibration, one found that the nonlocal parameter only affects the inertia of the system leading to lower natural frequencies as the nonlocal parameter increases, whereas the linear stiffness terms remain unchanged. In what the linear mode shapes are concerned, the nonlocal parameter has no influence in the lower modes, and its effect only becomes visible for higher modes. Furthermore the influence of this parameter in the boundary conditions was analysed, and one found that the double clamped boundary condition is more sensitive to nonlocal effects than the simply supported case in both natural frequencies and natural mode shapes.

Regarding the local non-linear stiffness terms, one found that when no external force is applied in the beam, only hardening spring effect is found, and the backbone curves of the system are symmetric, since the constant term and the second harmonic of the response are not excited, as the system is described by an equation of the Duffing

type. When nonlocal effects are taken into account, the non-linear stiffness terms are increased. This was verified when the static deflection of the beam was analysed, and it was found that increasing the nonlocal effects would lead to lower initial deflections. However, when the nonlocal effects are considered in the electrostatic force, the effect of the enhanced stiffness is overridden by the enhancement of the attraction force, thus leading to higher static deflections.

In the dynamical analysis, one found that the electrostatic attraction force, leads to lower fundamental natural frequencies, and this effect becomes more significant as the attraction force increases and gets closer to the "pull-in" voltage. The influence of the applied voltage and nonlocal effects in the dynamical behaviour of the system was carefully analysed. One found that for low voltages, the backbone curves of the system were shifted to lower frequency values, and presented an amplitude offset was due to the constant term, which introduces an asymmetric behaviour, where only spring hardening effect was detected. As the voltage was increased to higher values, the system dynamics becomes more complex, and both softening and hardening were found. When nonlocal effects were also considered, the asymmetric behaviour of the systems were more noticeable, and both softening and hardening effects were more pronounced. This analysis was made for both a simply supported and a double clamped nanobeam, and it was found that for the simply supported beam, softening behaviour was detected for lower voltage values. A 1:2 internal resonance was detected when higher modes of the double clamped beam were analysed, and energy exchanges between the third and fifth mode led to significant changes in the second symmetric mode shape of the nanobeam.

As the Timoshenko beam theory was used, the influence of the beam length in its dynamic behaviour was studied, and it was found that for the same applied voltage, longer beams have a more complex dynamical response, as they present higher deflections and therefore are submitted to higher variations of the attraction force during the oscillation cycle. The influence of the distance between the nanobeam and the static electrode was also analysed, since this parameter, along with the voltage, affects significantly the electrostatic force. Softening behaviour was detected for lower values of the gap size and voltage, and as the gap size increased only hardening effect prevailed, even when high voltages were considered.

The influence of fringed fields in the static and dynamical behaviour of a nanobeam was also explored. Its was found that the electrostatic force is related to the existing capacitance between the beam and the static electrode, and when the fringing field effect is considered, the actual existing capacitance is higher, thus leading to higher attraction forces when all the other parameters remain unchanged. This way, when this effect is considered, the "pull-in" voltage predicted is lower than when these fields are neglected. The influence of fringing fields is more noticeable for narrow beams, and it becomes negligible as the beam width is increased.

Furthermore, symmetry breaking bifurcation points were detected, which gave birth

to secondary branches. In systems that presented only odd harmonics in the main branch solutions, which are related to symmetric shapes, the bifurcation point led to the appearance of even harmonics in the secondary branch solutions, which present antisymmetric shapes. The appearance of the second harmonic in the secondary branch caused a 1:2 internal resonance, where energy exchanges between the first and second modes took place. It was found that nonlocal effects do not have any influence in the bifurcation points detected, and the applied voltage caused the bifurcations to appear for lower frequency ratio values.

A general overview of the molecular dynamic algorithm was also presented. This atomistic simulation can accurately describe the complete dynamical behaviour of a molecular/atomic structure like carbon nanotubes. Some MD simulations were carried out to compute the Young's modulus of a armchair (5,5) CNT and its natural frequencies, which were then compared with the results obtained with the continuum model developed. This comparison was useful to calibrate an accurate value of the nonlocal parameter for the CNT considered. A small insight of the CNT properties that affect the nonlocal parameter was made, and it was found that there is some disagreement between different results presented in the literature, which means that more atomistic simulations and experimental work must be carried out in order to accurately calibrate the CNT properties needed to successfully use the continuum models in their full potential.

6.2 Future Work

The focus in the development of models capable to accurately describe the highly non-linear behaviour of nanoscaled devices has only been intensified in the past few years, due to the interest in the application of these devices in various areas of technology. However, further research can be done in this field of knowledge, and some interesting topics to explore are presented below:

— The model presented in this work, accurately models the undamped linear and non-linear vibration nanobeams, where no energy dissipation terms are considered. However, as future work it would be interesting to consider damping terms to the model, which could be linear or even non-linear, and see the effect on the dynamic response of these systems;

— The analysis made is based on studying the vibration of a nanobeam actuated by a DC electrostatic force, which can be treated as a free vibration problem. As future work, the study of the forced vibration problem by considering an AC term of the electrostatic force could be carried out;

— The developed model only takes in to account the electrostatic force as external actuating forces. Therefore, Casimir effects and van der Walls forces could be included

in the model in order to study their effect in the dynamic of single walled and multi walled carbon nanotubes;

— The success of the nonlocal continuum models, is highly dependent on the nonlocal parameter used for each situation. Therefore, a detailed analysis of the dependency of the nonlocal parameter with geometric properties or boundary conditions should be made. This involves comparing the continuum model results with the ones derived with MD simulation and if possible with experimental results.

APPENDIX A

The integration by parts used to derive the mass and stiffness matrices presented in Chapter 2 are presented next. From the first equation of motion, Eq. (3.25a), one has the following terms:

$$\mathbf{t}(x)\Big(EA\frac{\partial^2 u}{\partial x^2}\Big) \Rightarrow \mathbf{K}_p = EA\frac{2}{L}\int_{-1}^{1}\mathbf{t}(\xi)\frac{\partial^2\mathbf{t}(\xi)}{\partial\xi^2}^T\mathbf{s}(t)d\xi$$
$$= EA\frac{2}{L}\Bigg(\underbrace{\mathbf{t}(\xi)\frac{\partial\mathbf{t}(\xi)}{\partial\xi}^T\mathbf{s}(t)\Big|_{-1}^{1}}_{=0} - \int_{-1}^{1}\frac{\partial\mathbf{t}(\xi)}{\partial\xi}\frac{\partial\mathbf{t}(\xi)}{\partial\xi}^T\Bigg) = -EA\frac{2}{L}\int_{-1}^{1}\frac{\partial\mathbf{t}(\xi)}{\partial\xi}\frac{\partial\mathbf{t}(\xi)}{\partial\xi}^T d\xi\mathbf{s}(t) \tag{A.1}$$

$$\mathbf{t}(x)\Big(EA\frac{\partial w}{\partial x}\frac{\partial^2 w}{\partial x^2}\Big) \Rightarrow \mathbf{K}_2^1 = EA\frac{2}{L^2}\int_{-1}^{1}\Big(\frac{\mathbf{f}(\xi)}{\partial\xi}^T\mathbf{q}_w(t)\Big)\mathbf{t}(\xi)\frac{\partial^2\mathbf{f}(\xi)}{\partial\xi^2}^T d\xi\mathbf{s}(t) \tag{A.2}$$

From the second equation of motion, Eq. (3.25b), one has the following terms:

$$\mathbf{f}(x)\Big(\rho A\frac{\partial^2 w}{\partial t^2}\Big) \Rightarrow \mathbf{M}^w = \frac{L}{2}\rho A\int_{-1}^{1}\mathbf{f}(\xi)\mathbf{f}(\xi)^T d\xi\ddot{\mathbf{q}}(t) \tag{A.3}$$

$$\mathbf{f}(x)\Big(-k_s GA\frac{\partial^2 w}{\partial x^2}\Big) \Rightarrow \mathbf{K}_\gamma^{22} = -\frac{2}{L}k_s GA\int_{-1}^{1}\mathbf{f}\frac{\partial^2\mathbf{f}}{\partial x^2}\mathbf{q}(t)d\xi$$
$$= -\frac{2}{L}k_s GA\Big(\underbrace{\mathbf{f}(\xi)\frac{\partial\mathbf{f}(\xi)}{\partial\xi}^T\mathbf{q}(t)\Big|_{-1}^{1}}_{=0} - \int_{-1}^{1}\frac{\partial\mathbf{f}(\xi)}{\partial\xi}\frac{\partial\mathbf{f}(\xi)}{\partial\xi}^T\mathbf{q}(t)d\xi\Big) = \frac{2}{L}k_s GA\int_{-1}^{1}\frac{\partial\mathbf{f}}{\partial\xi}\frac{\partial\mathbf{f}}{\partial\xi}^T d\xi\mathbf{q}(t) \tag{A.4}$$

$$\mathbf{f}(x)\Big(k_s GA\frac{\partial\phi}{\partial x}\Big) \Rightarrow \mathbf{K}_{\gamma}^{32} = k_s GA\int_{-1}^{1}\frac{\partial\mathbf{g}(\xi)}{\partial\xi}\mathbf{f}(\xi)^T d\xi\mathbf{r}(t) \tag{A.5}$$

$$\begin{aligned}\mathbf{f}(x)\Big(-\mu\rho A\frac{\partial^4 w}{\partial x^2 t^2}\Big) \Rightarrow \mathbf{M}^{\mu w} &= -\frac{2}{L}\mu\rho A\int_{-1}^{1}\mathbf{f}(\xi)\frac{\partial^2\mathbf{f}(\xi)}{\partial\xi^2}\ddot{\mathbf{q}}(\mathbf{t})d\xi \\ -\frac{2}{L}\mu\rho A\Big(\underbrace{\mathbf{f}(\xi)\frac{\partial\mathbf{f}(\xi)}{\partial\xi}^T\mathbf{q}(t)\Big|_{-1}^{1}}_{=0} &- \int_{-1}^{1}\frac{\partial\mathbf{f}(\xi)}{\partial\xi}\frac{\partial\mathbf{f}(\xi)}{\partial\xi}^T\mathbf{q}(t)d\xi\Big) = \frac{2}{L}\mu\rho A\int_{-1}^{1}\frac{\partial\mathbf{f}(\xi)}{\partial\xi}\frac{\partial\mathbf{f}(\xi)}{\partial\xi}^T d\xi\mathbf{q}(t)\end{aligned} \tag{A.6}$$

To derive the non-linear matrices $\mathbf{K}_5^1$ and $\mathbf{K}_6^2$ a simplification of Eq. (3.25b) has do be done first.

$$\begin{aligned}\frac{\partial^3}{\partial x^3}\Big(N\frac{\partial w}{\partial x}\Big) \Rightarrow \int_L \mathbf{f}(x)\frac{\partial^3}{\partial x^3}\Big(N\frac{\partial w}{\partial x}\Big)dx &= \underbrace{\mathbf{f}(x)\frac{\partial^2}{\partial x^2}\Big(N\frac{\partial w}{\partial x}\Big)\Big|_{-l/2}^{l/2}}_{=0} - \int_L\frac{\partial\mathbf{f}(x)}{\partial x}\frac{\partial^2}{\partial x^2}\Big(N\frac{\partial w}{\partial x}\Big) \\ = \underbrace{\frac{\partial\mathbf{f}(x)}{\partial x}\frac{\partial}{\partial x}\Big(N\frac{\partial w}{\partial x}\Big)\Big|_{-l/2}^{l/2}}_{=0} &- \int_L\frac{\partial^2\mathbf{f}(x)}{\partial x^2}\frac{\partial}{\partial x}\Big(N\frac{\partial w}{\partial x}\Big)\end{aligned} \tag{A.7}$$

Simplifying the derivative one has,

$$-\int_L\frac{\partial^2\mathbf{f}(x)}{\partial x^2}\frac{\partial}{\partial x}\Big(N\frac{\partial w}{\partial x}\Big) = -\int_L\frac{\partial^2\mathbf{f}(x)}{\partial x^2}\Big(\underbrace{\frac{\partial N}{\partial x}\frac{\partial w}{\partial x}}_{=0 \text{ Eq. (2.17a)}} + N\frac{\partial^2 w}{\partial x^2}\Big) \tag{A.8}$$

Substituting N by the relation presented in Eq (2.24a) one arrives at,

$$-\int_L\frac{\partial^2\mathbf{f}(x)}{\partial x^2}\Big(EA\mu\Big[\frac{\partial u}{\partial x}+\frac{1}{2}\Big(\frac{\partial w}{\partial x}\Big)^2\Big]\Big)\frac{\partial^2 w}{\partial x^2} \tag{A.9}$$

Finally, applying the Galerkin's method to Eq (A.9), the matrices $\mathbf{K}_5^1$ and $\mathbf{K}_6^2$ can be derived.

$$\begin{aligned}\mathbf{K}_5^1 &= -\frac{16}{L^4}EA\mu\int_{-1}^{1}\frac{\partial^2\mathbf{f}(\xi)}{\partial\xi}\frac{\partial\mathbf{t}(\xi)}{\partial x}^T\mathbf{s}(t)\frac{\partial^2\mathbf{f}(\xi)}{\partial\xi^2}^T\mathbf{q}(t)\\ &= -\frac{16}{L^4}EA\mu\int_{-1}^{1}\Big(\frac{\partial^2\mathbf{f}(\xi)}{\partial\xi^2}^T\mathbf{q}(t)\Big)\frac{\partial^2\mathbf{f}(\xi)}{\partial\xi^2}\frac{\partial\mathbf{t}(\xi)}{\partial\xi}^T d\xi\mathbf{s}(t)\end{aligned} \tag{A.10}$$

$$\begin{aligned}\mathbf{K}_6^2 &= -\frac{16}{L^5}EA\mu\int_{-1}^{1}\frac{\partial^2\mathbf{f}(\xi)}{\partial\xi}\frac{\partial^2\mathbf{f}(\xi^2)}{\partial x}^T\mathbf{q}(t)\frac{\partial^2\mathbf{f}(\xi)}{\partial\xi^2}^T\mathbf{q}(t)\\ &= -\frac{16}{L^5}EA\mu\int_{-1}^{1}\Big(\frac{\partial^2\mathbf{f}(\xi)}{\partial\xi^2}^T\mathbf{q}_w(t)\Big)^2\frac{\partial^2\mathbf{f}(\xi)}{\partial\xi^2}\frac{\partial^2\mathbf{f}(\xi)}{\partial\xi^2}^T d\xi\mathbf{q}(t)\end{aligned} \tag{A.11}$$

From the third equation of motion, Eq (2.25c), one has the following terms:

$$\begin{aligned}&\mathbf{g}(x)\Big(EI\frac{\partial^2\phi}{\partial x^2}\Big)\Rightarrow\mathbf{K}_b=\frac{2}{L}EI\int_{-1}^{1}\mathbf{g}(\xi)\frac{\partial^2\mathbf{g}(\xi)}{\partial\xi^2}\mathbf{r}(t)d\xi\\ &=EI\Big(\underbrace{\mathbf{g}(\xi)\frac{\partial\mathbf{g}(\xi)}{\partial\xi}^T\mathbf{r}(t)\Big|_{-1}^{1}}_{=0}-\int_{-1}^{1}\frac{\partial\mathbf{g}(\xi)}{\partial\xi}\frac{\partial\mathbf{g}(\xi)}{\partial\xi}^T\mathbf{r}(t)\Big)d\xi=-EI\int_{-1}^{1}\frac{\partial\mathbf{g}(\xi)}{\partial\xi}\frac{\partial\mathbf{g}(\xi)}{\partial\xi}^T\mathbf{r}(t)\end{aligned} \tag{A.12}$$

$$\mathbf{g}(x)\Big(k_sGA\frac{\partial w}{\partial x}\Big)\Rightarrow\mathbf{K}_\gamma^{32}=k_sGA\int_{-1}^{1}\mathbf{g}(\xi)\frac{\partial\mathbf{f}(\xi)}{\partial\xi}^T d\xi\mathbf{q}(t) \tag{A.13}$$

$$\mathbf{g}(x)\Big(\frac{2}{L}k_sGA\frac{\partial\phi}{\partial x}\Big)\Rightarrow\mathbf{K}_\gamma^{33}=k_sGA\int_{-1}^{1}\mathbf{g}(\xi)\mathbf{g}(\xi)^T d\xi\mathbf{r}(t) \tag{A.14}$$

$$\mathbf{g}(x)\Big(\rho A\frac{\partial^2\phi}{\partial t^2}\Big)\Rightarrow\mathbf{M}^\phi=\frac{L}{2}\rho A\int_{-1}^{1}\mathbf{g}(\xi)\mathbf{g}(\xi)^T d\xi\ddot{\mathbf{r}}(t) \tag{A.15}$$

$$\begin{aligned}&\mathbf{g}(x)\Big(-\mu\rho I\frac{\partial^4\phi}{\partial x^2t^2}\Big)\Rightarrow\mathbf{M}^{\mu\phi}=-\frac{2}{L}\mu\rho I\int_{-1}^{1}\mathbf{g}(\xi)\frac{\partial^2\mathbf{g}(\xi)}{\partial\xi^2}\ddot{\mathbf{r}}(t)d\xi\\ &=-\frac{2}{L}\mu\rho I\Big(\underbrace{\mathbf{g}(\xi)\frac{\partial\mathbf{g}(\xi)}{\partial\xi}^T\ddot{\mathbf{r}}(t)\Big|_{-1}^{1}}_{=0}-\int_{-1}^{1}\frac{\partial\mathbf{g}(\xi)}{\partial\xi}\frac{\partial\mathbf{g}(\xi)}{\partial\xi}^T\ddot{\mathbf{r}}(t)\Big)d\xi=\frac{2}{L}\mu\rho I\int_{-1}^{1}\frac{\partial\mathbf{g}(\xi)}{\partial\xi}\frac{\partial\mathbf{g}(\xi)}{\partial\xi}^T d\xi\ddot{\mathbf{r}}(t)\end{aligned} \tag{A.16}$$

BIBLIOGRAPHY

[1] Mehran Mehregany Darrin J. Young, Christian A. Zorman. Handbook of Nanotechnology. In Bhushan, editor, *Handbook of Nanotechnoloy*, chapter 12, pages 359–384. Springer, 3rd edition.

[2] Mohammad I. Younis. MEMS Linear and Nonlinear Statics and Dynamics. In Springer, editor, *MEMS Linear and Nonlinear Statics and Dynamics*, chapter 1, pages 1–11. 1st edition.

[3] Mohammad I. Younis. *Investigation of the Mechanical Behaviour of Microbeam-Based MEMS Devices*. PhD thesis, Faculty of the Virginia Polytechnic Institute and State University, 2001.

[4] Mir Masoud Seyyed Fakhrabadi, Abbas Rastgoo, and Mohammad Taghi Ahmadian. Size-dependent instability of carbon nanotubes under electrostatic actuation using nonlocal elasticity. *International Journal of Mechanical Sciences*, 80:144–152, 2014.

[5] D Sanchez-Portal, Emilio Artacho, J M José M Soler, Angel Rubio, and P Ordejon. Ab initio structural, elastic, and vibrational properties of carbon nanotubes. *Physical Review B*, 59(19):12678, 1999.

[6] I. R. Fernandez, H. Fangohr, and A. Bhaskar. Normal modes of carbon nanotubes: Similarities and differences with their continuum counterpart. *Journal of Physics: Conference Series*, 26(1):131–134, 2006.

[7] W. H. Duan, C. M. Wang, and Y. Y. Zhang. Calibration of nonlocal scaling effect parameter for free vibration of carbon nanotubes by molecular dynamics. *Journal of Applied Physics*, 101(2):1–7, 2007.

[8] A. Cemal Eringen. On differential equations of nonlocal elasticity and solutions of screw dislocation and surface waves. *Journal of Applied Physics*, 54(9):4703–4710, 1983.

[9] J. N. Reddy. Nonlocal theories for bending, buckling and vibration of beams. *International Journal of Engineering Science*, 45(2-8):288–307, 2007.

[10] C. M C Roque, A. J M Ferreira, and J. N. Reddy. Analysis of Timoshenko nanobeams with a nonlocal formulation and meshless method. *International Journal of Engineering Science*, 49(9):976–984, 2011.

[11] C M Wang, Y Y Zhang, and X Q He. Vibration of nonlocal Timoshenko beams. *Nanotechnology*, 18(10):105401, 2007.

[12] Q. Wang. Wave propagation in carbon nanotubes via nonlocal continuum mechanics. *Journal of Applied Physics*, 98(12), 2005.

[13] J N Reddy and S D Pang. Nonlocal continuum theories of beams for the analysis of carbon nanotubes. *Journal of Applied Physics*, 103(2), 2008.

[14] R. Ansari and S. Sahmani. Small scale effect on vibrational response of single-walled carbon nanotubes with different boundary conditions based on nonlocal beam models. *Communications in Nonlinear Science and Numerical Simulation*, 17(4):1965–1979, 2012.

[15] K. L. Ekinci. Electromechanical transducers at the nanoscale: Actuation and sensing of motion in nanoelectromechanical systems (NEMS). *Small*, 1(8-9):786–797, 2005.

[16] Marc Dequesnes, S V Rotkin, and N R Aluru. Calculation of pull-in voltages for carbon-nanotube-based nanoelectromechanical switches. *Nanotechnology*, 13(1):120–131, 2002.

[17] Changhong Ke, Horacio D. Espinosa, and Nicola Pugno. Numerical Analysis of Nanotube Based NEMS Devices Part II: Role of Finite Kinematics, Stretching and Charge Concentrations. *Journal of Applied Mechanics*, 72(5):726, 2005.

[18] M. Mojahedi, M. Moghimi Zand, and M. T. Ahmadian. Static pull-in analysis of electrostatically actuated microbeams using homotopy perturbation method. *Applied Mathematical Modelling*, 34(4):1032–1041, 2010.

[19] Slava Krylov. Lyapunov exponents as a criterion for the dynamic pull-in instability of electrostatically actuated microstructures. *International Journal of Non-Linear Mechanics*, 42(4):626–642, 2007.

[20] Bumkyoo Choi and E G Lovell. Improved analysis of microbeams under mechanical and electrostatic loads. *Journal of Micromechanics and Microengineering*, 7(1):24, 1997.

[21] Yongchul Ahn, Henry Guckel, and J David Zook. Capacitive microbeam resonator design. *Journal of Micromechanics and Microengineering*, 11(1):70, 2001.

[22] N. Kacem, S. Baguet, S. Hentz, and R. Dufour. Computational and quasi-analytical models for non-linear vibrations of resonant MEMS and NEMS sensors. *International Journal of Non-Linear Mechanics*, 46(3):532–542, 2011.

[23] Hassen M. Ouakad and Mohammad I. Younis. The dynamic behavior of MEMS arch resonators actuated electrically. *International Journal of Non-Linear Mechanics*, 45(7):704–713, 2010.

[24] A Nayfeh and P. Pai. *Linear and Nonlinear Structural Mechanics*. 2004.

[25] Wanda Szemplińska-Stupnicka. *The Behaviour of Nonlinear Vibration Systems - Volume II: Advanced Concepts and Applications to Multi-Degree-of-Freedom Systems*. Kluwer Academic Publishers.

[26] R.G. White M.M.Bennouna. The Effects of Large Vibration Amplitudes on the Fundamental Mode Shape of a Clamped-Clamped Uniform Beam. *Journal of Sound and Vibration*, 96(3):309–331, 1984.

[27] R. Lewandowski. Nonlinear free-vibrations of beams by the finite-element and continuation methods. *Journal of Sound and Vibration*, 170:577–593, 1994.

[28] R. Benamar AND M. M. K. Bennouna. The Effects of Large Vibration Amplitudes on the Mode Shapes and Natural Frequencies of Thin Elastic Structures , Part I : Simply Supported And Clamped-Clamped Beams. 232:179–195, 2000.

[29] P. Ribeiro and M Petyt. Non-Linear Vibration of Beams With Internal Resonance By the Hierarchical Finite-Element Method. *Journal of Sound and Vibration*, 224(4):591–624, 1999.

[30] S. Stoykov and P. Ribeiro. Nonlinear free vibrations of beams in space due to internal resonance. *Journal of Sound and Vibration*, 330(18-19):4574–4595, 2011.

[31] Bo Fang, Ya-Xin Zhen, Chi-Ping Zhang, and Ye Tang. Nonlinear vibration analysis of double-walled carbon nanotubes based on nonlocal elasticity theory. *Applied Mathematical Modelling*, 37(3):1096–1107, 2013.

[32] Y. M. Fu, J. W. Hong, and X. Q. Wang. Analysis of nonlinear vibration for embedded carbon nanotubes. *Journal of Sound and Vibration*, 296(4-5):746–756, 2006.

[33] J. Yang, L. L. Ke, and S. Kitipornchai. Nonlinear free vibration of single-walled carbon nanotubes using nonlocal Timoshenko beam theory. *Physica E: Low-Dimensional Systems and Nanostructures*, 42(5):1727–1735, 2010.

[34] R. Ansari and H. Ramezannezhad. Nonlocal Timoshenko beam model for the large-amplitude vibrations of embedded multiwalled carbon nanotubes including thermal effects. *Physica E: Low-Dimensional Systems and Nanostructures*, 43(6):1171–1178, 2011.

[35] W.Han. *The analysis of isotropic and laminated rectangular plates including geometrical non/linearity using the p-version finite element method*. Ph.d. thesis, University of Southampton, 1993.

[36] N S Bardell. Free vibration analysis of a flat plate using the hierarchical finite element method. *Journal of Sound and Vibration*, 151(2):263–289, 1991.

[37] I.N. Katz I. Babuska, B.A. Szabo. The p-Version of the Finite Element Method. *Journal on Numerical Analysis*, 18(3):515–545, 2015.

[38] Metin Aydogdu. A general nonlocal beam theory: Its application to nanobeam bending, buckling and vibration. *Physica E: Low-Dimensional Systems and Nanostructures*, 41(9):1651–1655, 2009.

[39] Huu Tai Thai. A nonlocal beam theory for bending, buckling, and vibration of nanobeams. *International Journal of Engineering Science*, 52:56–64, 2012.

[40] T Kaneko. On Timoshenko's correction for shear in vibrating beams. *Journal of Physics D: Applied Physics*, 8(16):1927, 1975.

[41] J. R. Hutchinson. Shear Coefficients for Timoshenko Beam Theory. *Journal of Applied Mechanics*, 68(1):87, 2001.

[42] R. M C Mestrom, R. H B Fey, J. T M van Beek, K. L. Phan, and H. Nijmeijer. Modelling the dynamics of a MEMS resonator: Simulations and experiments. *Sensors and Actuators, A: Physical*, 142(1):306–315, 2008.

[43] R. M C Mestrom, R. H B Fey, K. L. Phan, and H. Nijmeijer. Simulations and experiments of hardening and softening resonances in a clamped-clamped beam MEMS resonator. *Sensors and Actuators, A: Physical*, 162(2):225–234, 2010.

[44] Dean T. Nayfeh, Ali Hasan and Mook. *Nonlinear Oscillations*. Wiley-VCH Verlag GmbH, 2007.

[45] Klaus-Jürgen Bathe. *Finite Element Procedures*. Klaus-Jurgen Bathe.

[46] E Riks. An incremental approach to the solution of snapping and buckling problems. *International Journal of Solids and Structures*, 15(7):529–551, 1979.

[47] M. A. Crisfield. A fast incremental/iterative solution procedure that handles "snap-through". *Computers and Structures*, 13(1-3):55–62, 1981.

[48] P. Ribeiro. *Geometrical Nonlinear Vibration of Beams and Plates by the Hierarchical Finite Element Method*. PhD thesis, University Of Southampton, 1998.

[49] M A Eltaher, Amal E Alshorbagy, and F F Mahmoud. Vibration analysis of Euler Bernoulli nanobeams by using finite element method. *Applied Mathematical Modelling*, 37(7):4787–4797, 2013.

[50] Mário Oliveira. *Vibrações de Nanoplacas*. PhD thesis, Faculdade de Engenharia da Universidade do Porto, 2014.

[51] S. Woinowski-Kriger. The efect of an axial force on the vibration of hinged bars. *Journal of Applied Mechanics*, pages 239–249, 1950.

[52] Mergen H. Ghayesh. Nonlinear size-dependent behaviour of single-walled carbon nanotubes. *Applied Physics A: Materials Science and Processing*, 117(3):1393–1399, 2014.

[53] M. Simsek. Large amplitude free vibration of nanobeams with various boundary conditions based on the nonlocal elasticity theory. *Composites Part B: Engineering*, 56:621–628, 2014.

[54] A. N. Cleland and M. L. Roukes. Fabrication of high frequency nanometer scale mechanical resonators from bulk Si crystals. *Applied Physics Letters*, 69(18):2653–2655, 1996.

[55] R Spiering, V.L., Bouwstra, S., Spiering. On chip decoupling zone for package-stress reduction. *Sensors and Actuators, A: Physical*, 39:149–156, 1993.

[56] M.C. Hegg and A.V. Mamishev. Influence of Variable Plate Separation on Fringing Electric Fields in Parallel-Plate Capacitors, 2004.

[57] Jarosaw Meller. Molecular Dynamics. *Encyclopedia of Life Sciences*, pages 1–8, 2001.

[58] L. Falquet R. Stote, A. Dejaegere, D. Kuznetsov. Molecular Dynamics Simulations - HARMM - http://www.ch.embnet.org/MD_tutorial/, 1999.

[59] Y Y Zhang, C M Wang, and V B C Tan. Assessment of Timoshenko beam models for vibrational behavior of single-walled carbon nanotubes using molecular dynamics. *Adv. Appl. Math. Mech*, 1(1):89–106, 2009.

[60] Paras M. Agrawal, Bala S. Sudalayandi, Lionel M. Raff, and Ranga Komanduri. A comparison of different methods of Young's modulus determination for single-wall carbon nanotubes (SWCNT) using molecular dynamics (MD) simulations. *Computational Materials Science*, 38(2):271–281, 2006.

[61] QuantumWise. Atomistix ToolKit Manual, 2008.

[62] M M J Treacy, T W Ebbesen, and J M Gibson. Exceptionally high Young's modulus observed for individual carbon nanotubes. *Nature*, 381(6584):678–680, 1996.

[63] Y. G. Hu, K. M. Liew, and Q. Wang. Modeling of vibrations of carbon nanotubes. *Procedia Engineering*, 31:343–347, 2012.

[64] B. I. Yakobson, C. J. Brabec, and J. Bernholc. Nanomechanics of carbon tubes: Instabilities beyond linear response. *Physical Review Letters*, 76(14):2511–2514, 1996.

[65] Y. Huang, J. Wu, and K. C. Hwang. Thickness of graphene and single-wall carbon nanotubes. *Physical Review B - Condensed Matter and Materials Physics*, 74(24):1–9, 2006.